2017-05-03

Spectroscopy Based Approaches for Detection of Ions, Alpha-L-Fucosidase, and Singlet Oxygen

Eric Waidely
University of Miami, ericwaidely@gmail.com

UNIVERSITY OF MIAMI

SPECTROSCOPY BASED APPROACHES FOR DETECTION OF IONS, ALPHA-L-FUCOSIDASE AND SINGLET OXYGEN

By

Eric Waidely

A DISSERTATION

Submitted to the Faculty
of the University of Miami
in partial fulfillment of the requirements for
the degree of Doctor of Philosophy

Coral Gables, Florida

May 2017

UNIVERSITY OF MIAMI

A dissertation submitted in partial fulfillment of
the requirements for the degree of
Doctor of Philosophy

SPECTROSCOPY BASED APPROACHES FOR DETECTION OF IONS, ALPHA-L-FUCOSIDASE AND SINGLET OXYGEN

Eric Waidely

Approved:

_____
Roger M. Leblanc, Ph.D.
Professor of Chemistry

_____
James Wilson, Ph.D.
Professor of Chemistry

_____
Orlando Acevedo, Ph.D.
Associate Professor of Chemistry

_____
Guillermo J. Prado, Ph.D.
Dean of the Graduate School

_____
Jean-Marie Parel, Ph.D.
Research Associate Professor
Bascom Palmer Eye Institute

WAIDELY, ERIC (Ph.D., Chemistry)

Spectroscopy Based Approaches for Detection of Ions, Alpha-L-Fucosidase and Singlet Oxygen (May 2017)

Abstract of a dissertation at the University of Miami.

Dissertation supervised by Professor Roger M. Leblanc.
No. of pages in text. (113)

The detection of unknown analytes is a staple of analytical chemistry. Whether it be contaminants, biomarkers, or potential medicine, quantifying the presence of analytes can lead to great benefits. Toxic contaminants in food and water cause many health complications and can often be fatal. Due to industrialization, water contamination has become a more common problem of modern society. Poor environmental awareness in mining practices can yield toxic metal contamination into water supplies. Water containing heavy metals can lead to a regional health crisis, as the local water can no longer be used for drinking or farming practices.

One way in which water contamination can be combatted is to develop new ways to detect and remove these toxic materials. Host-guest interactions have been implemented to bind metal cations in solution. There are many different types of molecules capable of host-guest interactions, however, cavitands are among the most well-established. Cavitands are macromolecules named for the cavity in the center of the molecule in which guest molecules can become included. The most common cavitands are based upon the calix[4]arene and possess a negatively charged cavity, which is ideal for host-guest interactions with positively charged metal cations. Most cavitands are poorly soluble, especially in polar solvents such as water. Although solubility limits the use of cavitands in solution, they can be modified to become more amphiphilic by altering the “head” and

“tail” groups. By producing amphiphilic cavitands, it is possible to generate one-molecule thick layers of cavitands and observe the host-guest interaction with metal cations through surface chemistry at the air-water interface. By monitoring the host-guest interaction at the air-water interface with spectroscopy, it can be possible to distinguish the type of metal that is interacting with the cavitand.

Alternatively, some analytes can be detected to diagnose certain diseases. These analytes are referred to as biomarker, and are any type of molecule whose presence can be indicative of a disease. One example of such an analyte is alpha-L-fucosidase. Alpha-L-fucosidase is an oncofetal enzyme that catalyzes the cleavage of fucose-bound molecules. Standard adult diets do not regularly include fucose, and as such, the production of alpha-L-fucosidase is limited after gestation. Although alpha-L-fucosidase is almost undetectable in healthy blood serum, it has been found to be elevated in the blood serum of individuals suffering from hepatocellular carcinoma. The neoplasm forms upon mutatation of healthy liver tissue that causes the cells to rapidly grow, similar to growth prior to gestation. This reversion back to the growth stage promotes the synthesis alpha-L-fucosidase and can thus be used confirm the presence of a tumor.

The detection of alpha-L-fucosidase can be achieved through a variety of methods. Many approaches have been investigated based on the enzyme kinetics of alpha-L-fucosidase, but the detection is limited to relatively high concentrations. It is possible that elevated levels of alpha-L-fucosidase are missed by enzyme-based assays. Immunoassays can enhance the detection of alpha-L-fucosidase by using an immunoglobulin antibody that binds exclusively to an epitope on the enzyme. The development of immunoassays typically involves a solid support to fix the antibody into the proper orientation and lower

the amount of antibody needed through packing. Two different supports were used for the detection of alpha-L-fucosidase through an immunoassay. The first approach uses a quartz slide and commonly implemented conjugation techniques. The second approach explores a more recent field of biosensing using nanoparticles. Antibodies immobilized to a gold-nanoparticle were used to develop an optical assay that exploits the energy transfer from a carbon dot probe emission to the surface plamson of the gold nanoparticle.

Finally, some unknown analytes are believed to possess medicinal properties. The medicinal properties of molecules are often discovered prior to discovering the source or mechanism of the observed therapeutic benefits. One such analyte is singlet oxygen produced from photoactivation of a sensitizer. The cytotoxic effect exhibited by some porphyrin or dye molecules on cells was recognized long before the source of apoptosis was discovered. The cytotoxicity of certain dye molecules was developed as a new form of disease treatment which is called photodynamic therapy.

Photodynamic therapy is most often used in the treatment of cancer due to the site-specific manner treatment can be administered. Photosensitizer molecules are biologically inert until activated by irradiation, allowing the location of the cytotoxicity to be controlled by an external light source. One limitation of this approach is that light must be able to reach to photosensitizer. This limits the use of photodynamic therapy, as not every wavelength of light is capable of penetrating tissue deep enough to reach the disease location. Bacterial keratitis does not suffer from this limitation, as the cornea is exposed and can be irradiated by most wavelengths of light. Photodynamic therapy has been used to treat bacterial keratitis and promising results have been obtained. However, the concentration of sensitizer, the irradiation time, the number of treatments necessary, and

the ideal sensitizer drug all remain under investigation. Furthermore, the exact mechanism of cytotoxicity is still under debate. Singlet oxygen and superoxide radicals formed from reactions of the excited photosensitizer with ground state triplet oxygen, are believed to be the source of apoptosis. To confirm the cytotoxic source, the quantum yield of singlet oxygen generation, radical superoxide anions, and the effect they have on bacterial keratitis must be determined.

ACKNOWLEDGEMENTS

Above all else, I would like to thank Dr. Leblanc for mentoring me during my time at the University of Miami. He was always available to discuss research or anything else that may have been on my mind. I learned many great leadership qualities from observing Dr. Leblanc as a mentor, the foremost being the importance of maintaining collaboration. I am most grateful to have had the opportunity to learn from Dr. Leblanc that while it is important to work hard for the things you are passionate about, you can always make time for a martini at the end of a long day.

I would also like to thank my committee members Dr. James Wilson and Dr. Orlando Acevedo. They challenged me and advised me throughout my graduate studies and gave me invaluable suggestions that will help me in my career. I sincerely thank my external committee member, Dr. Jean Marie-Parel. The collaboration I had with Dr. Parel was a remarkable learning experience. I cannot thank him enough for allowing me to participate in the amazing research he is doing at Bascom Palmer.

Thank you to the staff and faculty of the Department of Chemistry. Thank you Noel Urbina, Nyisha Alexander, Juanita and Raul Hernandez for all your help and support during my time at the University of Miami. I would like to give special thanks to Ana Parr for all the help she provided. The graduation process can be a complicating headache but Ana was so on top of everything that it was a breeze.

Thank you to my present group members Shiv Sharma, Xu Han, Yiwen Ji, Yiqun Zhou, Sajini Hettiarachchi, Piumi Liyanage and Zhili Peng for all the support and collaboration. I wish you all the best in your continued studies. I would also like to extend thanks to previous group members Shanghao Li, Sheba Johnson, and Nicolas

Crawford who were with me at the start of my research studies and helped me establish good lab techniques.

Last, thank you to my friends and family for all your support. To my chemistry golfing buddies, Anthony Cauley and Brian Doherty, thank for your friendship during our time here. I wish you both the best of luck in your last year of research and in your future careers. To Anthony Player, Anthony Heath and Rocky Hinkle, thank you for helping me enjoy time away from the lab but always reminding me to keep the train rolling. Saving the most important for last, thank you to my amazing parents. You taught me the importance of working hard and without that, none of this would be possible. Thank you for always being in my corner and supporting me all the way to the end.

TABLE OF CONTENTS

LIST OF FIGURES

Chapter 5

Chapter 6

LIST OF TABLES

LIST OF SCHEMES

Chapter 4

LIST OF ABBREVIATIONS

AcPy	Acetylated aryl pyrogallol[4]arene
AFP	Alpha-fetoprotein
AFU	Alpha-L-fucosidase
ATR-FTIR	Attenuated total reflection-Fourier transform infrared spectroscopy
AuNp	Gold nanoparticle
BSA	Bovine serum albumin
CPS	Counts per second
CT	Computerized tomography
CT(PEG)12	1-mercapto-3,6,9,12,15,18,21,24,27,30,33,36-dodecaoxanoatrriacontan-39-oic acid
DPBF	1,3-diphenylisobenzofuran
EDC	1-ethyl-3-(3-dimethylaminopropyl) carbodiimide
ELISA	Enzyme-linked immunosorbent assay
FA	Furfuryl alcohol
FITC	Fluorescein isothiocyanate
GGT	γ-Glutamyltranspeptidase
HCC	Hepatocellular carcinoma
IgG	Immunoglobulin
IRRAS	Infrared reflective-absorption spectroscopy
Isc	Intersystem crossing
LED	Light Emitting Diode
MES	2-(N-morpholino) ethane sulfonic acid

MRI	Magnetic resonance imaging
NHS	N-hydroxysuccinimide
PBS	Phosphate buffer saline
PDT	Photodynamic therapy
RB	Rose Bengal
RPM	Revolutions per minute
$^1O_2$	Singlet oxygen
Φ_Δ	Singlet oxygen quantum yield
SM(PEG)12	Succinimidyl-([N-maleimidopropionamido]-dodecaethylene glycol) ester
SPR	Surface plasmon resonance
τ_T	Triplet state lifetime
2-D	Two dimensional
UV	Ultraviolet

Chapter 1

Introduction

1.1 Detection of Ions

Heavy metal poisoning has become a growing public health concern. One of the most common routes of exposure is from contaminated water. The sources of contamination can vary greatly, whether it be lead from pipes,[1] mercury released from industrial waste,[2] or cadmium from mining practices.[3] For instance, in the early 20th century a region of Japan began to experience elevated rates of bone softening and kidney failure. They named the effects Itai-Itai disease ("it hurts-it hurts disease"), which was later found to be caused by cadmium poisoning from a nearby mine contaminating local rivers.[4]

As pure water is a basic need for human survival, there is great need to develop materials capable of detecting or filtering impurities from water. One way in which toxic metals can be detected in water is through host-guest interactions[5] with cavitand molecules.[6] Macrocyclic cavitands include molecules such as calixarenes,[7-9] cucurbiturils,[10-12] and cyclodextrins.[13] Calixarenes have been shown to form complexes with small molecules[14,15] and ions[16-19] and have also displayed promising benefits for molecular recognition[20,21] and enzyme-mimics.[22]

The ability of calixarene derivatives to form complexes with metal cations through host-guest interactions has previously been investigated.[23-26] It has been shown that it is possible to alter the binding affinity of the cavitand by manipulating the starting materials.[27-29] One way in which calixarenes can be modified is to change the number of hydroxyl head groups the cavitand possesses. The classical synthesis of calixarenes comes from a condensation reaction between a para-substituted phenol and

formaldehyde. Alternative phenols, such as benzene-1,3-diol (resorcinol) and 1,2,3-trihydroxybenzene (pyrogallol), can be used to produce the calixarene derivatives resorcinarene and pyrogallolarene, respectively.[30] Furthermore, the tail group of the calixarene derivative can also be modified by changing the aldehyde used to react.

Given the ability to modify the head and tail groups, calixarenes can be catered to exhibit amphiphilic properties.[31] The amphiphilic nature of most calixarene derivatives make them interesting candidates to observe at the air-water interface.[32] Markowitz et al.[33] exemplified that calixarenes are capable of self-assembly at the air-water interface.

Langmuir monolayers can be produced by spreading amphiphilic molecules onto a hydrophobic-hydrophilic barrier, typically the air-water interface, to produce a one-molecule-thick layer.[34,35] The classical experiments used to characterize Langmuir monolayers are to produce surface pressure-area (π-A) and surface potential-area (ΔV-A) isotherms.[36,37] π-A isotherms are produced by depositing a known number of molecules on top of a subphase containing a pressure-sensitive Wilhelmy plate, at which point the molecules expand to lower repulsion effects.[38] After allowing the molecules to equilibrate into the most favorable orientation, the one-molecule-thick layer is compressed by barriers. Prior to compression, the molecules are oriented apart and the surface tension is null, but once the barriers are compressed, the molecules are forced into closer proximity which results in an increase in surface tension until the point at which the tension becomes too great and the monolayer collapses into multiple layers.[39] ΔV-A isotherms are produced in the same manner as π-A, but the voltage is measured using an electrode rather than the pressure-sensitive Wilhelmy plate. Surface potential measurements analyze the dipole moments produced when a monolayer is forming, the

reorganization or water and the dipole moments of the water subphase.[38] This allows for more sensitive measurement of molecular interactions at greater distances than surface pressure alone, which is only capable of recognizing the van der Waals interactions when molecules come close together.

Langmuir monolayers have been found to be sensitive to changes in the environment that lead to alterations in the packing of the monolayer.[40] An example of a change in the environment could be the concentration of ions present in the subphase. By adding ions into the subphase, the host-guest interactions calixarene Langmuir monolayers can be probed.[41] Through the incorporation of infrared reflective-absorption spectroscopy (IRRAS), the effects of host-guest interactions on calixarene Langmuir monolayers can be observed to detect different ions in various concentrations.[42]

1.2 Detection of Alpha-L-Fucosidase

Hepatocellular carcinoma (HCC) is one of the most recurrent types of cancer and is the 2nd leading cause of cancer mortality worldwide as of 2015.[43] The incidence rate for HCC is almost identical to the mortality rate, as the tumor is fatal for a majority of people within a year of diagnosis.[44] For neoplasms of the liver, HCC is the most prevalent, encompassing approximately 90-95% of all liver cancers.[45] The rate of HCC onset is directly influenced by the presecnce of liver diseases. Cirrhosis and hepatitis B and C are the leading causes of HCC.[46] Many countries experience above average cases of cirrhosis and hepatitis B and C.[47,48] Regions where liver diseases are more common can be considered high risk areas for HCC pevalence. In these places, HCC is not only one th leading cause of cancer related deaths in the U.S.A. but is the 5th leading cause of cancer death in Asia and the Middle East. The Center for Disease Control (CDC) reported that

from 2001-2006, the incidence of HCC in the United States increased from 2.7 per 100,000 persons in 2001 to 3.2 per 100,000 persons in 2006. The incidence rate for males was 5 per 100,000, which is ~5 times higher than the incidence rate for females. In Saudi Arabia, the overall incidence rate for HCC onset is 4.8, with an incident rate of 7.2 and 2.9 for males and females, respectively.[49] The highest rate of incidence globally is found amoung Asians/Pacific Islanders, where the rate of incidence climbs up to an average of 7.8 per 100,000 persons and has steadily been increasing.

Presently, hepatocellular carcinoma (HCC) is an issue that bears global impact. Preexisting complications of the liver have an immense impact on the etiology of HCC. In regions where complications of the liver are common, the amount of HCC occurence is significantly elevated. Cirrhosis of the liver is one of the most prominent sources of HCC formation, and thus, the risk factors for cirrhosis correspondingly beget vulnerability of tumorigenesis. Hepatitis B and C are two of the largest contributers to cirrhosis, and have been shown to increase the probability of carcinogensis.[50-52] For example, Japan has one of the highest densities of individuals with chronic hepatitis C virus (HCV). A study on trends of HCC incidence in Japan found that a generation of post World War II Japanese men experienced a well-above average influx of HCV, and there was a corresponding spike from 29.2 to 41.9 cases per 100,000 people of HCC observed from 1981-1987.[53] Other minor risk factors include alcohol/tobacco abuse,[54,55] nonalcoholic fatty liver disease (NAFLD)[56] and environmental toxins.[51,57] Alcohol has been a well-known cause for cirrhosis, but it's effects on the liver can be evaded through abstanence. Environmental toxins, however, are a worldwide problem. Aflatoxin is one of the most prevalent environmental toxins and is well known for being carcinogenic.[58]

Aflatoxins arise predominantly from the fungus *Aspergillus flavus* and are commonly found in commodities, such as cereal seeds, cotton, beans/legumes, and a wide range of nuts.[59] A study on food contamination in the Jeddah Region of Saudi Arabia found that roughly 26% of all the food products tested contained high levels of aflatoxin, with seeds being the most drastically contaminated.[60] It has been previously documented that high intake of aflatoxins through diet can be associated with higher occurrences of HCC.[61] Due to the high rate of mortality of HCC, it is necessary to regularly screen individuals whom experience frequent exposure to all of the above aforementioned risk factors.

While the occurrence rate of hepatocellular carcinoma is amongst the highest for all types of cancer worldwide, it is the mortality rate that causes the greatest level of concern. One of the prominent causes of the high mortality rate of this particular neoplasm is the late stages at which a diagnosis is confirmed. Currently, HCC is detected through magnetic resonance imaging (MRI), ultrasonography, and/or computerized tomography (CT).[62] While these detection techniques are proficient in tumor diagnosis, they are typically only successful when tumors reach sizes >1cm in diameter. Treatment of HCC usually occus through surgical resection of the cancerous tissue. HCC treatement is rarely successful, mostly due to the late stages at which the cancer is detected. It is therefore desirable to develop more sensitive detection approaches, to screen at-risk individuals to provide earlier diagnosis, which will improve the chances for survival.

Biosensing is an alternative branch of cancer diagnostics that could provide early detection. Biosensors are developed by coupling a physiochemical detector to a biological component. Many different physiochemical detectors have been developed,

which are most commonly based upon enzyme-linked immunosorbent assay (ELISA),[63,64] radioimmunoassays,[65] spectroscopy assays,[66,67] potentiometic assays,[68] and surface plasmon resonance (SPR).[69] While the source of detection in each approach can vary from electrochemical to optical responses, a common theme in most biosensors is the implementation of antibodies. Immunoglobulin (IgG) is an ideal component for an assay because it allows for high specifity to a biological molecule, such as a specific protein or enzyme.

The use of biosensing has shown promising improvements in early cancer detection and in some cases, it can even help determine the prognosis of disease.[70-72] Biosensors for cancer are developed to detect cancer specific biomarkers. These biomarkers are any measurable substance found within an organism whose presence can be indicative of neoplasm formation. Biomarkers provide a marked improvement in cancer detection, as the level of cancer specific antigens will elevate above normal levels typically long before the tumor has grown large enough to be detected by visible approaches. HCC biomarkers can be divided into four categories: embryonic and glycoprotein antigens; enzymes and isozymes; genes; and cytokines.[45] Recent data suggests that genes and cytokines could potentially be the most sensitive for detection, however, further research needs to be performed to defend these claims.[73]

Serum alpha-fetoprotein (AFP) is the most universally used antigen for diagnosing HCC. AFP is an embryonic protein that is typically only produced by the fetal liver.[74] Typically, healthy individuals express levels of alphafetoprotein that are < 20 ng/mL, as the liver ceases synthesis AFP after gestation.[75] It has been found, however, that HCC onset causes an influx of AFP, allowing its presence in serum samples to be used as an

indicator of tumorigenesis.[76-78] However, AFP is not a perfect diagnostic test as 40% of individuals with early HCC development express normal or acceptable AFP levels.[79,80]

Several other biomarkers for HCC have been proposed, but many (such as squamous cell carcinoma antigen[81]) are not exlcusive to HCC and can be present from other types of cancer. γ-Glutamyltranspeptidase (GGT) represents an HCC biomarker that could greatly improve diagnostics.[82] GGT is a membrane-bound enzyme and is one of the least investigated markers for HCC.[83] GGT is a glycoprotein, with several known isoforms.[84,85] While GGT as a whole has been found to be elevated in complications of the liver, it is the GGT-II isoform that shows the most promising benefits tumor diagnosis.[86] The GGT-II isoform is almost exclusively present with hepatoma, and has been shown to increase the specificity of HCC detection to 97.1%.[87] Furthermore, combination of GGT and AFP screening achieves the highest sensitivity of HCC detection to date, however, further investigation in combining markers must be done as the initial tests were obtained from small sample groups.[82,88]

Alpha-L-fucosidase (AFU) is another enzyme that has been associated with HCC. Alpha-L-fucosidase is a lysosomal enzyme that catalyzes the hydrolytic cleavage of fucose-containing molecules.[89] Mammalian α-L-fucosidases are glycoproteins, possessing several isoforms of varying molecular weight (~20-225 kDa) with optimal activity between pH 4 and 6.5.[90] AFU is present in low concentrations in all animal tissues but has been found to be overexpressed in cancerous tissue, particularly with HCC.[91] It has been found that AFU can diagnose 85% of HCC patients up to 6 months before it is detectable by ultrasonography.[92]

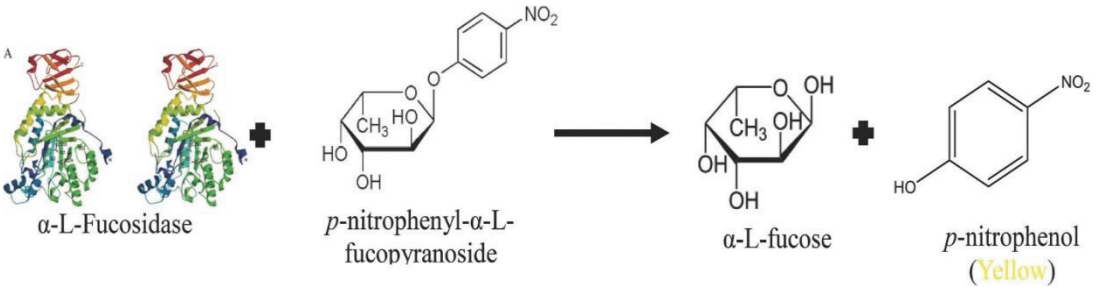

Figure 1.1 Schematic of the assay developed through the hydrolysis of *p*-nitrophenyl-α-L-fucopyranoside by AFU to produce α-L-fucose and the colored product *p*-nitrophenol.

AFU serum values are typically given in regards to the enzymes catalytic activity using the SI unit katal or the more commonly utilized enzymatic unit (U). The reason AFU serum values were not previously expressed in mol/L was a result of the heterogeneity of AFU and its various isoforms. Avila and Convit[93] developed the first assay on AFU in 1974 by means of measuring the enzymatic activity with the colorimetric substrate *p*-nitrophenyl-α-L-fucopyranoside (PNFP) as depicted in **Figure 1.1**.[94] In brief, the enzymatic activity is measured at a pH of 5.5 in an acetate buffer and the absorbance of the cleaved *p*-nitrophenol is observed at 400 nm. The connection between AFU serum levels and HCC onset was not made until ten years later when Deugnier et al.[95] used a previously described AFU assay[96] to establish a correlation between high AFU levels and carcinoma.

To date, the most prevalent detection technique is the above-mentioned assay using the colorimetric substrate PNFP. Many research groups have used this approach to determine the onset of HCC with sensitivities ranging from 60-90% and specificities ranging from 55-98%.[48,97-100] An alternative method was proposed by Wang et al.[101] by chlorinating the 2 position of the standard substrate *p*-nitrophenyl-α-L-fucopyranoside to produce 2-chloro-4-nitrophenyl-α-L-fucoside. The addition of a chlorine group to the

substrate leads to an increased cleavage rate and produces a faster assay with sensitivity for HCC detection reported at 81.8% and specificity of 85.4%. While the standard approach for AFU detection appears to show promise in HCC detection, it is still affected by incubation times, indirect measurements via catalytic rates and interference caused by the overlap in yellow color of the substrate collected and that of the inherently yellow color of serum samples from high levels of bilirubin.[68]

1.3 Detection of Singlet Oxygen

Although the concept of photodynamic therapy (PDT) was postulated in 1904,[102,103] it wasn't until the 1960s that the toxic effect of some photosensitive dyes was discovered to be from the creation of a reactive oxygen species.[104] This observed cytotoxic effect drew many to develop treatments using photosensitive molecules, called photosensitizers. The most prevalent use for PDT to date is in the treatment of neoplasms.[105] PDT treatment of tumors began utilizing the site-specific control that PDT offers.[106,107] The sensitizers can be administered topically or intravenously, and then the drug can be activated in the desired region by irradiating the specific area with the appropriate wavelength of light.[108,109]

Upon irradiation of a photosensitizer, there are two pathways in which a cytotoxic oxygen species is produced, Type I and Type II.[110] When a photon is absorbed by the sensitizer, the sensitizer transitions from its ground state to the excited state. In the excited state, it is possible for a radical species to be produced by either electron transfer to create a superoxide radical anion or by hydrogen atom abstraction from a substrate.[111] If a radical species is produced upon irradiation, the sensitizer is said to have undergone a Type I mechanism. Alternatively, it is also possible upon

excitation for the sensitizer to react with ambient oxygen via triplet-triplet interactions to generate singlet oxygen. If singlet oxygen is produced upon excitation, the sensitizer is said to have undergone a Type II mechanism.

Although the sensitizer can produce a cytotoxic agent through a Type I or Type II mechanism, these are not the only possible pathways upon irradiation. Once a photon is absorbed by the sensitizer, it can relax back down to the ground state by emitting a photon from fluorescence or the photon can transition to an excited triplet state through intersystem crossing (ISC). From the triplet state, the sensitizer can then emit a photon in the form of phosphorescence and relax back down to the ground state or singlet oxygen can be produced via energy transfer to oxygen in its ground state.

PDT has been used to treat bladder, colorectal, breast, brain, head, neck, oral, and skin cancers.[112-114] The main appeal of using PDT to treat cancer is it allows the tumor to be destroyed, while limiting the cytotoxicity towards healthy cells that traditional chemotherapies exhibit. In developing PDT for cancer treatment, a few main parameters must be met. The sensitizer chosen must remain biologically inert until irradiation occurs, it must accumulate at the tumor site and photoactivation must be possible at the tumor site. Because photoactivation occurs at the tumor site, the photosensitizers that can be used are limited by the wavelength of light that can reach the tumor. **Figure 1.2**[115] portrays the penetration depth for a few corresponding wavelengths of irradiation.

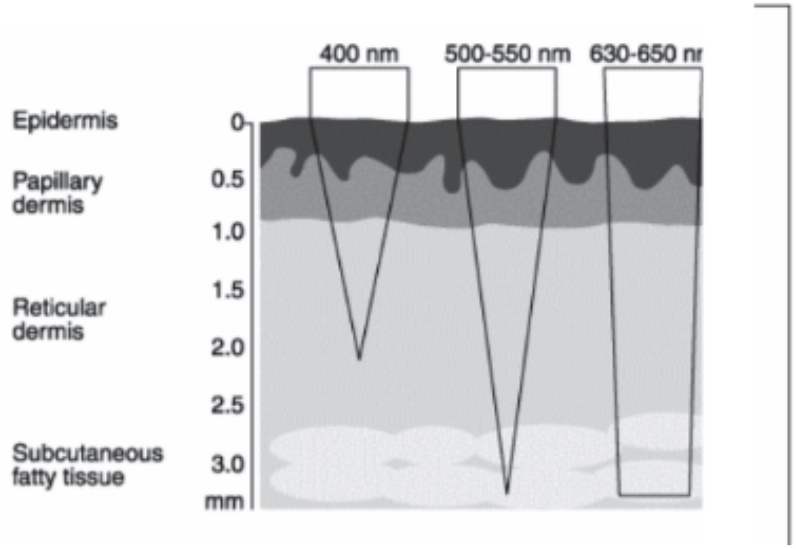

Figure 1.2 Tissue penetration of light with respect to wavelength.

Due to the lack of penetration from wavelengths smaller than those in the near infrared region, many photosensitizers have had minimal research done on their photodynamic therapy capabilities. While photosensitizers that are activated by UV or visible light are ineffective for PDT in deep tissue, they can be effective on exposed organs. The potential uses for PDT at treating infections of the cornea are currently being invesitgated.[116-118] Sensitizers can easily be applied directly to the infection site through drops and the cornea can be irradiated with UV and visible light, opening a wider range of potential photosensitizers to be utilized in PDT.

Chapter 2

Host-Guest Complexation of a Pyrogallol[4]arene Derivative at the Air-Water Interface

2.1 Background

Cavitand molecules have been well investigated for the favorable host-guest interactions. The most investigated type of cavitand is the calixarene.[17,119] Calixarenes can be modified by altering the nature of the starting phenol.[120] Synthesized from the acid-catalyzed condensation of pyrogallol (1,2,3-trihydroxybenzene) with an aldehyde, pyrogallol[4]arenes are calix[4]arene derivatives that possess three hydroxyl head groups instead of the typical one. After the first reported synthesis in 1999,[121] some work has been done studying pyrogallol[4]arenes using aliphatic aldehydes, however little has been done researching the effect of using aryl aldehydes. Unlike calixarenes, pyrogallol[4]arenes possess 12 hydroxyl head groups. These hydroxyl groups are oriented in close proximity upon macrocycle formation, leading to the formation of a network of hydrogen bonds between neighboring hydroxyl groups. These intermolecular interactions cause complications with solubility, as only dimethyl sulfoxide, dimethylformamide and high pH solutions capable of disrupting the hydrogen bond network, solubilize these cavitands. By acetylating the hydroxyl head groups of pyrogallol[4]arenes, the network of hydrogen bonds can be disrupted and the macromolecule gains solubility in polar solvents such as acetone and acetonitrile, as well as, solubility in non-polar solvents such as hexanes and chloroform. Although small esters have low hydrophilicity, the solubility gained upon acetylation in both polar and non-polar solvents suggests that the macromolecular effects of producing esters results in the expression of amphiphilic properties. These amphiphilic properties made it possible

to observed a Langmuir monolayer of an acetylated aryl pyrogallol[4]arene (AcPy). By combining surface chemistry techniques with spectroscopy, the orientation and conformational changes that occur upon host-guest interaction with an AcPy Langmuir monolayer can be measured.[122]

Calixarene derivatives have been shown to have host-guest interacations with metal cations.[23-26] Using AcPy, the metal binding can be enhanced from traditional calixarenes, through the incorporation of a network of carbonyls to the head group of the cavitand. Carbonyls possess more favorable electrostatic interactions with large metal cations than hydroxyl groups alone. One ion found to have binding affinity towards AcPy is cadmium. Cadmium is a toxic metal and consumption can lead to cadmium poisoning. Symptoms of this poisoning include osteomalcia, brought on by the cadmium displacing calcium, causing the softening of bones. The ability of cadmium to displace calcium occurs because of the similar properties expressed by both atoms within biological systems. It is therefore important to be able to selectively distinguish between biologically relevant materials such as calcium and toxic cadmium.

Acetylated aryl pyrogallol[4]arene was found to form a stable Langmuir monolayer at the air-water interface. In addition to self-assembly, this molecule has also shown consistent host-guest interactions with divalent metal cations, while no interaction was observed for monovalent ions. Through infrared spectroscopy, it was possible to distinguish between calcium and cadmium complexation. The host-guest interactions of acetylated aryl pyrogallol[4]arene were studied at the air-water interface using surface pressure-area and surface potential-area isotherms, compression-decompression, stability and infrared reflective-absorption spectroscopy (IRRAS).

2.2 Experimental

2.2.1 Materials and methods

In accordance to a prior published synthesis,[123] pyrogallol was mixed with benzaldehyde in an acid-catalyzed condensation. The purified product was then acetylated with acetic anhydride under alkaline conditions to produce acetylated aryl pyrogallol[4]arene (AcPy).

Chloroform was obtained from Alfa Aesar (Ward Hill, MA, USA) with purity greater than 99.5%. Cadmium chloride was also acquired from Alfa Aesar (Ward Hill, MA, USA) with purity greater than 99.0%. Calcium chloride, potassium chloride and sodium chloride were received from Sigma Aldrich (St. Louis, MO, USA) with purity greater than 98.5%. Cadmium chloride and calcium chloride were both used after further purification by extraction with chloroform to remove surfactants. The pure water used in the experiments was obtained from a Modulab 2020 Water purification system (Continental Water System Corp., San Antonio, TX, USA) with a resistivity of 18MΩ·cm, surface tension of 72.6 mN m^{-1}, and pH 5.6 at 20.0 ± 0.5°C.

All isotherm measurements and IRRAS spectroscopy were obtained in a clean room (Class 1000) with a constant temperature of 20.0 ± 0.5°C and a humidity of 50 ± 1%. A Kibron μ-trough S (Kibron Inc., Helsinki, Finland) with an area of 5.9 x 21.1 cm^2 was used for the studies of surface pressure- and surface potential-area isotherms, compression-decompression cycles, stability and IRRAS. Surface pressure was monitored by the Wilhelmy method,[124] using an alloy wire probe with a sensitivity of ±0.01 mN m^{-1}. Surface potential was measured with a Kelvin probe to an accuracy of 10 mV.

The IRRAS measurements of the AcPy Langmuir monolayer were recorded with an EQUINOX 55 Fourier transform infrared spectrometer (Bruker Optics, Billerica, MA, USA), connected to an XA-511 external reflection accessory with a mercury-cadmium-telluride detector cooled by liquid nitrogen. The measurements were performed using p-polarized light on a Kibron μ-trough S. Each spectrum was acquired by the co-addition of 1200 scans with a resolution of 8 cm^{-1}. The IRRAS spectra were used without any processing or baseline correction.

2.2.2 Langmuir monolayer preparation

AcPy was provided as an amorphous powder that was then dissolved using chloroform. The concentration of AcPy in chloroform used for each experiment was between 0.20 and 0.22 μmol/L. Different concentrations of cadmium, calcium potassium and sodium chloride solutions (0.1, 0.3 and 0.5 M) were used as the subphase, as well as, purified water. The spreading volume for AcPy was between 30 and 40 μL, depending on the subphase used and the concentration of AcPy stock solution. The sample was spread at the air-water interface using a 50 μL syringe (Hamilton Co., Reno, NV, USA) by uniform droplet deposition over the subphase surface. A waiting period of 20 min was taken for the AcPy Langmuir monolayer to reach equilibrium after spreading. The Langmuir monolayer was compressed at a rate of 10 cm^2/min. Triplicate experiments confirmed the reproducibility of the data.

2.2.3 Infrared reflection-absorption measurements

To determine the optimal angle for IRRAS measurements, the Langmuir monolayer was first compressed to a surface pressure of 10 mN m^{-1} and measurements

were taken in 5° increments from 35° to 70°. An angle of 40° was chosen to do further IRRAS measurements due to the favorable signal to noise shown at this angle.

2.3 Surface chemistry of a pyrogallol[4]arene Langmuir monolayer

2.3.1 Surface pressure-area and surface potential-area isotherms

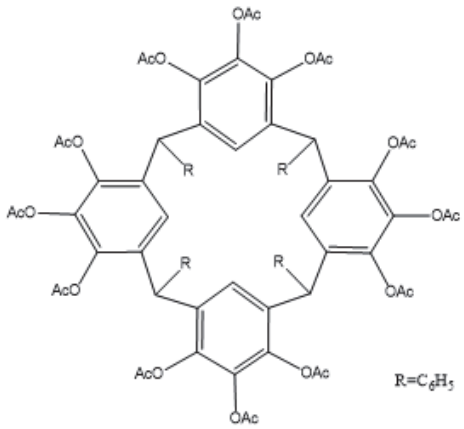

Figure 2.1 Molecular structure of acetylated aryl pyrogallol[4]arene (AcPy)

Pure water was used as the subphase first to obtain the AcPy (**Figure 2.1**) Langmuir monolayer. A concentration of 0.20 μmol/L of AcPy in chloroform was spread onto the pure water subphase. As shown in **Figure 2.2**, the surface pressure had a lifting point of around 250 $Å^2$ per molecule. By extrapolating the linear portion of the plot to zero, the limiting molecular area was shown to be, on average, 192 $Å^2$ per molecule. According to crystallographic data,[123] the area of AcPy is 213 $Å^2$. Pyrogallol[4]arenes generally take one of two conformations; all cis (rccc) or cis-trans-trans (rctt). The crystal structure shows AcPy taking rctt conformation, but it is likely that this is not the case at the air-water interface. At the air-water interface, it is more likely that the conformation shifts to all cis, as this would lead to more favorable hydrophilic/hydrophobic interactions of the head and tail groups. The all cis

conformation is prone to take up less area than the cis-trans-trans conformation, as the molecule would be forced into a cone. It is also likely the acetyl groups are overlapping neighboring molecules at the air-water interface, leading to a lower molecular area than that observed in the crystal structure. These slight differences can account for the reduction in molecular area observed at the air-water interface in comparison to the crystallographic data.

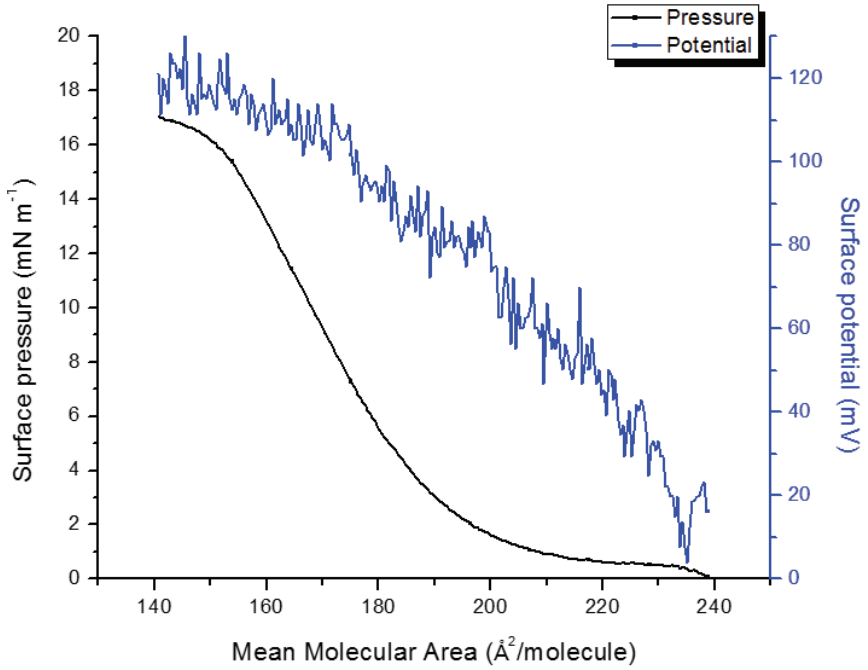

Figure 2.2 Surface pressure-area isotherm (black) and surface potential-area isotherm (blue) of AcPy Langmuir monolayer.

The surface potential-area isotherm (**Figure 2.2**) is correlated with the surface pressure-area isotherm. Surface potential measurements are able to encompass the dipole moments found as molecules are forming a monolayer, as well as, the reorganization of water and its own dipole moments.[38] This allows for interactions between molecules to be measured at much larger distances than surface pressure alone, which mainly measures the van der Waals interactions between molecules in close contact.[125] As

expected, the surface potential begins to increase upon compression of the Langmuir monolayer. The potential continues to increase relatively smoothly in a linear fashion until around 160 Å^2. The collapse of the potential corresponds to the same molecular area where the collapse can be seen for the surface pressure-area isotherm.

2.3.2 Compression-decompression and stability measurements

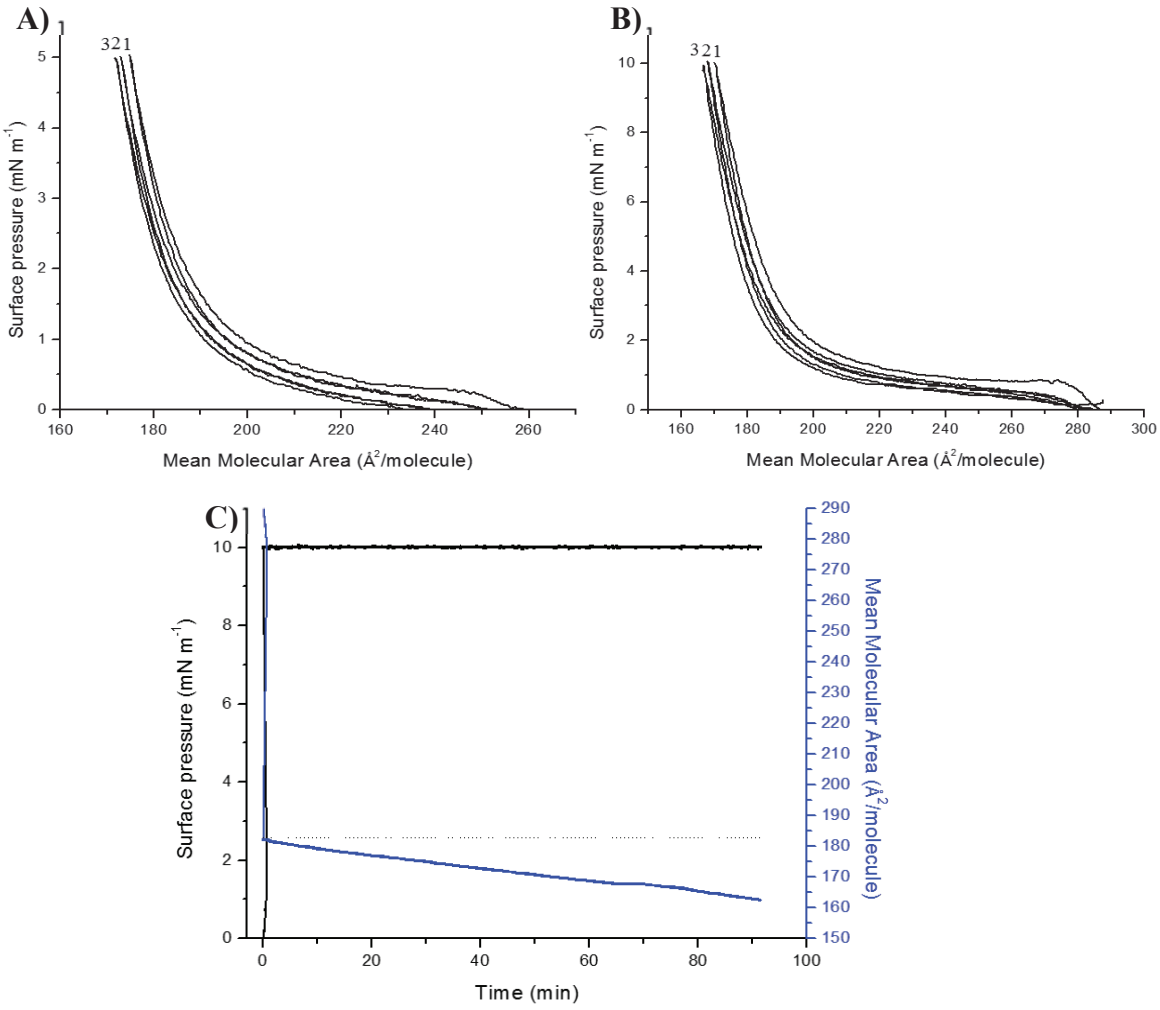

Figure 2.3 Compression-decompression cycles of the AcPy Langmuir monolayer on a pure water subphase at surface pressure (A) 5 and (B) 10 mN m^{-1}. (C) Stability measurement at 10 mN m^{-1}.

The stability of the AcPy Langmuir monolayer was then tested by performing three compression-decompression cycles at both 5 and 10 mN m^{-1}, followed by a stability

study at a constant pressure of 10 mN m^{-1} (**Figure 2.3**). From **Figures 2.3A-B**, a hysteresis is observed at both surface pressures. However, there is very little difference between the first compression and the final compression (1.7 and 2% difference in area, respectively). Furthermore, as the barriers approached the maximum area start position, the surface pressure returned to 0 mN m^{-1}. This suggests that no aggregation of the AcPy Langmuir monolayer occurs, as aggregate formation would cause an increase in surface tension. Next, a stability study was carried out by compressing the monolayer to a constant surface pressure of 10 mN m^{-1} (**Figure 2.3C**). After 90 minutes had elapsed, there was a change in the mean molecular area of approximately 10%. A time of 90 minutes was chosen for stability measurements because this is approximately the amount of time needed for IRRAS measurements. The observed 10% change can be attributed to conformational changes within the Langmuir monolayer. As compression begins, the Langmuir monolayer may not completely reach equilibrium. As time proceeds, the individual molecules reorganize and adopt the most favorable conformation, resulting in a slight change in the observed mean molecular area after 90 minutes.

2.3.3. Ion effect

Upon changing the subphase to increasing concentrations of cadmium chloride dissolved in water, an increase in the mean molecular area was observed, while the collapse pressure remains relatively unchanged (**Figure 2.4**). The overall shape of the isotherm does not appear to be impacted by increasing concentrations of metal ions in the subphase. The limiting molecular area shows an increase from 192 $Å^2$/molecule in pure water to 211, 222 and 236 $Å^2$ for 0.1, 0.3 and 0.5 M cadmium chloride, respectively. From the data, it was observed that there was a complexation between the cadmium

cation and the cavity of the AcPy. Due to the amphiphilic nature of the AcPy, the molecule will orient itself at the air-water interface in a way that leads to favorable hydrophilic/hydrophobic interactions. This causes the ester head groups to orient towards the aqueous subphase, while the hydrophobic aryl tail groups will face in the opposite direction towards the air. Because of this orientation, an interaction between the ester head groups and the Cd^{2+} ions in the subphase is possible. As the ions interact with AcPy, it would be expected that the mean molecular area would show an increase, as fitting an ion within the pocket of the cavitand would cause the cavity to expand slightly to minimize electron repulsion. As more ions are added to the subphase, the area would continue to increase as the number of individual cavitands forming complexes would increase. Mean molecular area measures the average area per molecule found in the Langmuir monolayer. As the concentration of ions in the subphase increases, the number of individual cavitands forming complexes with the ions in the subphase will increase proportionally. This proportional increase should lead to a linear trend in mean molecular area growth as a function of ion concentration, until saturation is reached and every molecule in the Langmuir monolayer has formed a complex. This corresponds to the data shown in **Figure 2.4B**, as a linear trend is observed in the increase in mean molecular area in relation to an increase in cadmium chloride concentration up to 0.5 M.

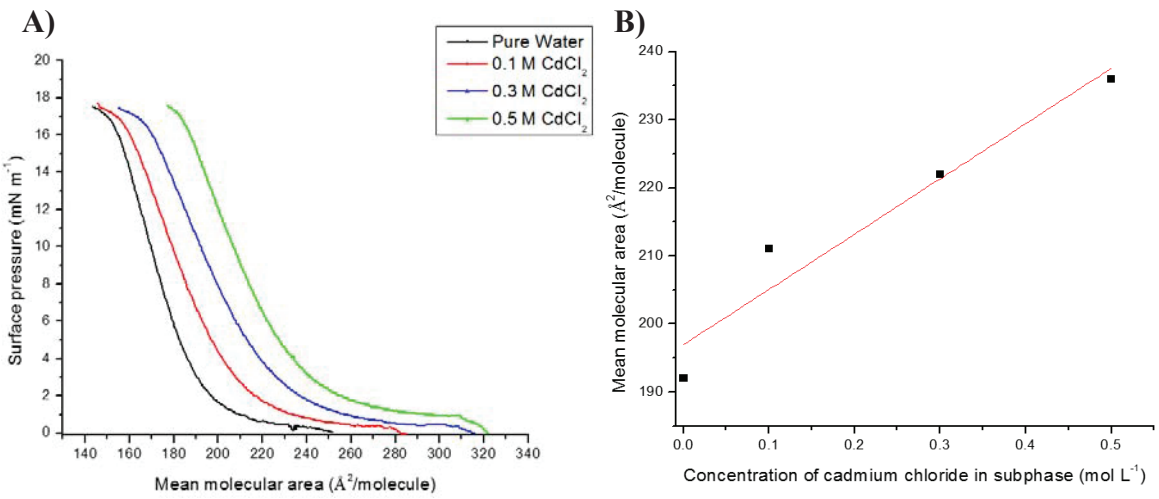

Figure 2.4 (A) Surface pressure-area isotherms of AcPy Langmuir monolayer on pure water subphase and subphase solution containing 0.1, 0.3, and 0.5 M $CdCl_2$. (B) Linear trend of the increase in mean molecular area in relation to the increase of $CdCl_2$ concentration in the subphase.

Likewise, changing the subphase to increasing concentrations of calcium chloride also appears to complex with AcPy, as an increase of mean molecular area is observed (**Figure 2.5**). The shape and collapse pressure were analogous to that of the cadmium subphase measurement. The overall change in mean molecular area is slightly different than that of the cadmium complexation, showing increases to 200, 213, and 235 $Å^2$ for 0.1, 0.3 and 0.5 M calcium chloride, respectively. While the increase in the limiting molecular area for calcium is comparable to that of cadmium, the slightly lower increase at 0.1 and 0.3 concentrations resulted in a better linear trend for calcium. Due to the similar charge and size of calcium and cadmium, it would be expected that there is similar coordination for each molecule.

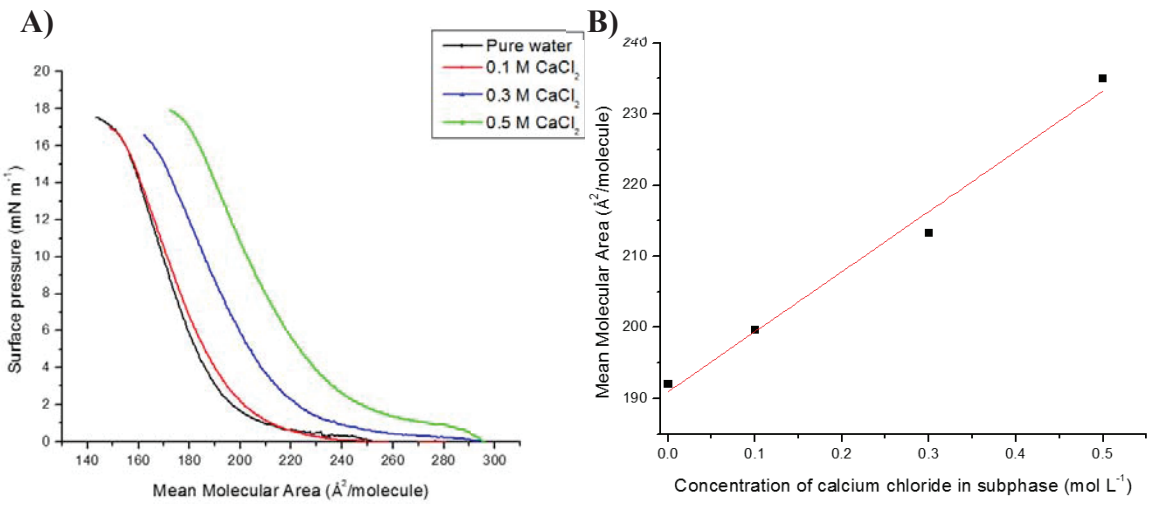

Figure 2.5 (A) Surface pressure-area isotherms of AcPy Langmuir monolayer on pure water and subphase solution containing 0.1, 0.3, and 0.5 M $CaCl_2$. (B) Linear trend of the increase in mean molecular area in relation to the increase of $CaCl_2$ concentration in the subphase.

Furthermore, measurements for sodium chloride and potassium chloride subphases were also attempted. To begin, a concentration of 0.5 M sodium chloride was chosen to perform surface pressure-area measurements. However, upon testing the 0.5 M sodium chloride subphase in triplicate, no observable change was obtained from that of the pure water subphase. This result suggests that there is no complexation occurring between the AcPy and monovalent cations. To be sure that no complexation occurs with monovalent cations, measurements were attempted using a potassium chloride subphase. Again, a concentration of 0.5 M potassium chloride subphase was chosen to perform surface pressure-area measurements. After testing the 0.5 M potassium chloride subphase in triplicate, there was still no change observed from that of a pure water subphase. It is likely that the monovalent cations do not possess a strong enough electrostatic interaction with AcPy for any complexation to be observed.

2.4 Spectroscopy of a pyrogallol[4]arene Langmuir monolayer

2.4.1 Infrared reflection-absorption spectroscopy on pure water subphase

Infrared reflective-absorption spectroscopy (IRRAS) is a useful technique for determining conformational and orientational information of a Langmuir monolayer. When performing IRRAS measurements, the polarization of light is important. The component perpendicular to the plane of incidence, S-polarized light, produces a stronger signal on our instrument; however the p-polarized parallel component gave better resolution for the observed stretching peaks.[126] Accordingly, all measurements were obtained using p-polarization.

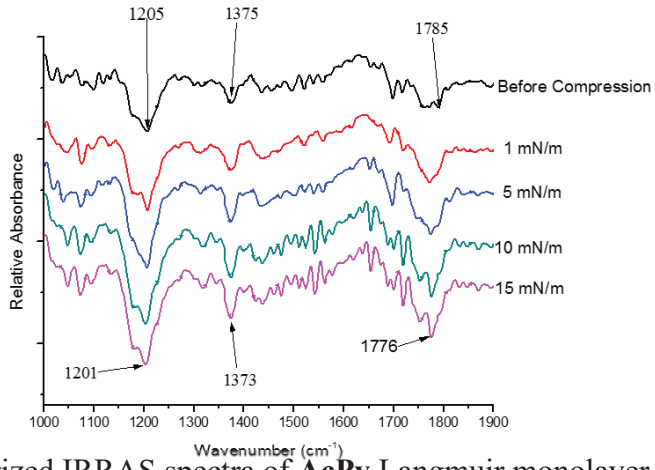

Figure 2.6 P-polarized IRRAS spectra of **AcPy** Langmuir monolayer at 40 degrees for increasing surface pressures.

From **Figure 2.6**, the IRRAS spectra of AcPy Langmuir monolayer are shown on a pure water subphase. Before compression begins, the spectrum appears relatively weak and undefined when compared to the peaks after compression. This is expected because before compression the individual molecules are further apart, causing fewer molecules to be in contact with the incident beam. As compression occurs, more and more molecules will be moved into range of the laser, subsequently increasing the intensity and

resolution of the peaks observed. This corresponds with the data, as the spectrum before the collapse of the isotherm at 15 mN m^{-1} produces the most defined peaks. While C-H stretching peaks are observed in the range of 2800-3000 cm^{-1} for this molecule, the signal for these peaks are very weak and therefore difficult to properly assign. This is likely due to the rigid nature of the molecule or its particular orientation at the air-water interface. C=C stretching can be observed in the range of 1400-1600 cm^{-1} as would be expected with the high number of aromatic carbons. Although these peaks are visible, the close proximity of these peaks makes it difficult to observe any changes that may occur upon compression or through changing the nature of the subphase. As such, the stretching frequencies of the ester moiety were the primary focus for these measurements. Molecules containing ester groups typically show C=O stretching around 1700 cm^{-1} and two C-O stretch peaks between 1000-1300 cm^{-1}. The C-O peaks can be observed at around 1200 and 1370 cm^{-1}, while the C=O stretch appeared at 1776 cm^{-1}. As seen in Figure 4, the C-O and C=O stretch for AcPy show a shift from the start of compression to the last measurement at 15 mN m^{-1}. Before compression begins, the molecules are further apart and have slightly more freedom than they do when compressed. As a result, the stretch before compression should be higher in energy than the stretch observed upon compression. This correlates with the data, as before compression the C-O stretches shift from 1205 and 1375 to 1201 and 1373 cm^{-1}, respectively. The C=O stretch also experiences a shift from 1785 before compression to 1776 cm^{-1} after compression.

2.4.2 Infrared reflection-absorption spectroscopy on ion subphases

While it is difficult to differentiate between the complexation of cadmium and calcium ions from surface chemistry alone, it is possible to discriminate the two ions

using spectroscopic methods. It is well known that pyrogallol[4]arenes are excellent host molecules. For this acetylated molecule, it would be expected that the carbonyl moiety would be the source of complexation of a guest molecule. Due to the difference in electronegativity between oxygen and carbon, each carbonyl would have partially negatively charged oxygen atoms. This would allow a positively charged guest molecule to coordinate itself near these partial negative charges due to favorable electrostatic interactions. When this complexation occurs, the stretching of the C=O bond will be restricted. By restricting the movement of this stretch, the energy correlated with it would decrease and, as a result, the wavenumber of this stretch would be lower. From **Figure 2.7A**, it is observed that C-O stretches appear at 1204 and 1372 cm^{-1}, while the C=O stretch is at 1739 cm^{-1} for spectra with cadmium ions present. However, with calcium ions present (**Figure 2.7B**), the C=O stretch is much lower, at 1700 cm^{-1}, while C-O stretches are no longer observed. **Figure 2.7C** confirms that a decrease in stretching energy is observed upon ion complexation, as addition of cadmium and calcium causes the C=O stretch to shift from 1776 to 1739 and 1700 cm^{-1}, respectively at 15 mN m^{-1}. The C-O stretch also allows for differentiation between the ions as the C-O stretches disappear with calcium present, while they remain relatively unaffected by addition of cadmium. From the data, it is clear that there is not only a significant difference between the wavenumber of these peaks, but the overall shape and intensity of the peaks is different. When interpreting the differences observed between the effect of calcium and cadmium, it is important to note that the difference in radius of these two ions is relatively negligible. With little difference in size, the large shift in wavenumber must be attributed to an interaction other than size. It is likely that the interaction between the

carbonyls and the calcium ion is more favorable than that of cadmium due to a smaller difference in energy levels. Both cadmium and calcium will have an empty s-orbital, but cadmium's valence s-orbital will be the 5s while calcium's would be the 4s. Since the ion will be interacting with oxygen, which is in the second energy level, it would be expected that the smaller difference in shell energy will lead to the most favorable interaction. The more favorable the interaction is between the ion and the carbonyl, the closer it will be oriented towards the carbonyl, leading to a lower wavenumber. This corresponds to what is observed in the data.

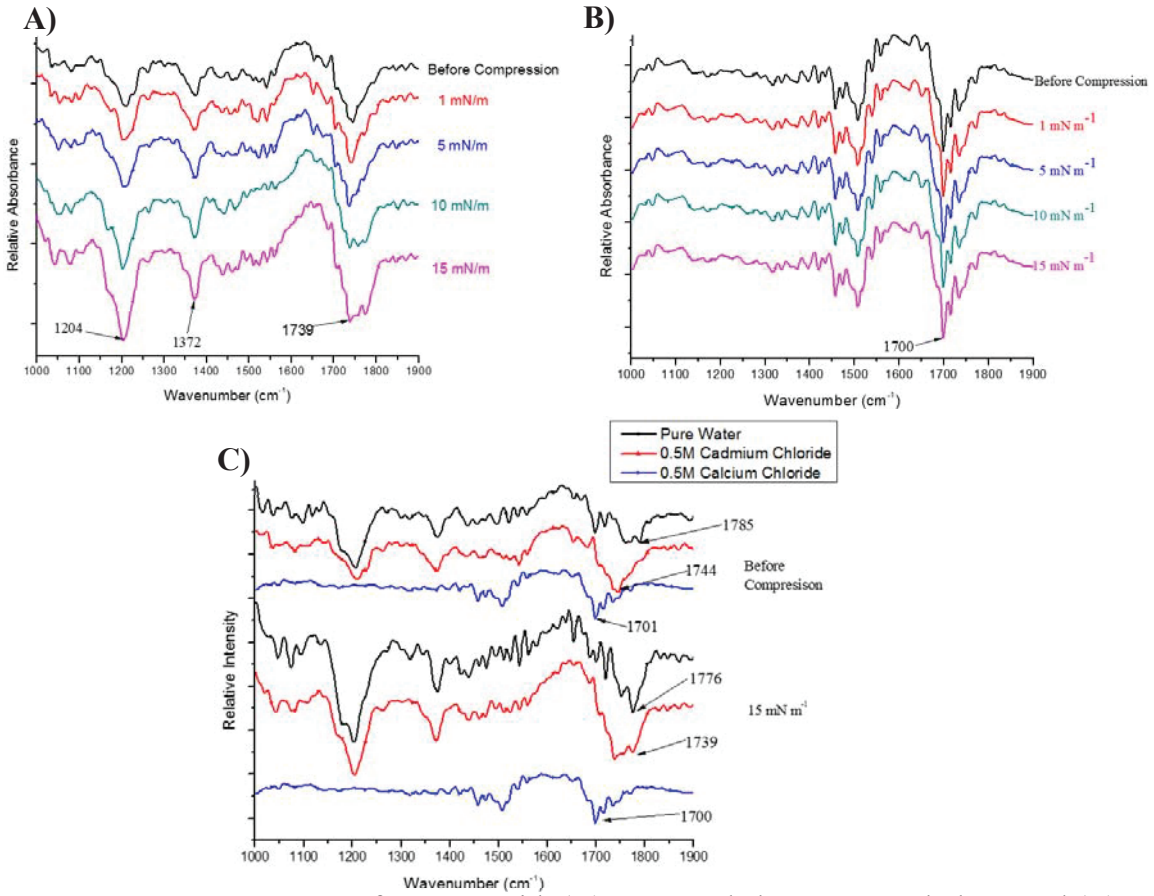

Figure 2.7 IRRAS spectra for AcPy with (A) 0.5 M $CdCl_2$ aqueous subphase and (B) 0.5 M $CaCl_2$ aqueous subphase. (C) Comparison of IRRAS spectra on pure water subphase and 0.5 M $CdCl_2$ and 0.5 M $CaCl_2$ aqueous subphase before compression and after being compressed to 15 mN m^{-1}.

2.5 Summary

In conclusion, the host-guest chemistry of AcPy was studied using surface chemistry and spectroscopy at the air-water interface. It is shown that AcPy is capable of self-assembly, forming a stable Langmuir monolayer at the air-water interface. This Langmuir monolayer is capable of interacting with different divalent metal cations, while no interaction is observed for monovalent metal cations. Spectroscopic analysis gave further characteristics of the AcPy Langmuir monolayer at the air-water interface. From the spectroscopy point of view, it was possible to not only confirm the complexation occurring between this host and the metal guests, but it was also possible to distinguish between the two metals being complexed.

Chapter 3

Alpha-L-Fucosidase: Physical Properties and Relevance as a Biomarker

3.1 Background

A growing method for cancer detection is to search for the presence of cancer specific biomarkers, rather than the tumors themselves.[63,71] One such biomarker that has shown promise in cancer diagnostics is alpha-L-fucosidase (AFU). AFU is a glycoprotein with several known isoforms and optimal activity at pH 4-6.5.[94] AFU synthesis ceases after gestation, leaving only trace levels in the tissues of healthy individuals.[91] The presence of AFU has been associated to the onset of several different types of carcinoma, with recurrent use in diagnosing hepatocellular carcinoma (HCC).[127] The majority of human alpha-L-fucosidase exists as a soluble enzyme, primarily found in serum or lysozymes.[128] However, a small amount of AFU can be found membrane-bound in the brain,[129] as well as, in cells of colon adrenocarcinoma.[90]

Developing sensitive detection methods for AFU is a growing area of interest. Current detection techniques rely primarily on the enzymatic properties of AFU, using the rate of cleavage of a specific substrate (*p*-nitrophenyl-α-L-fucopyranoside).[68,97] Antibodies are a common platform for enhancing the detection of biological molecules, as they can be catered to bind the desired antigen specifically. Finding an ideal antibody for an assay requires maximizing molecular recognition.[130]

While many groups have observed the properties of AFU in solution,[66,80,88,101] little is known of the interactions at the air-water interface. A better understanding of the membrane-bound properties of AFU could lead to improved treatment of colon

adenocarcinoma. New cancer therapy is being developed that implements the use of antibodies that have been linked to a drug, called antibody-drug-conjugates (ADC).[131-133] These ADC's target surface-bound proteins that are known to exist primarily on tumor cells.[134,135] AFU represents a potential target for use in colon adenocarcinoma, however, more must be known of the 2-D properties of AFU.

The air-water interface is a well-known model system for investigating the 2-D properties of membrane-bound proteins through the use of Langmuir monolayers.[136] Proteins and peptides are inherently amphiphilic, due to the large size and charge these molecules typically possess. It is this phenomenon that allows proteins to be deposited at the air-water interface to form one-molecule thick layers of protein.[137]

AFU was found to form a stable Langmuir monolayer at the air-water interface. Langmuir monolayer formation was confirmed by surface pressure- and surface potential-area isotherms, as well as compression-decompression cycles and stability measurements. The AFU monolayer was further investigated through infrared reflective-absorption spectroscopy (IRRAS). Furthermore, the 2-D interaction between AFU and an anti-alpha-L-fucosidase IgG (FUCA2) was confirmed at the air-water interface.

3.2 Experimental

3.2.1 Materials and methods

Alpha-L-fucosidase and anhydrous citric acid were purchased from Sigma Aldrich (St. Louis, MO, USA). FUCA2 antibody was obtained from Abgent (San Diego, CA, USA). Sodium chloride, sodium phosphate, sodium azide and magnesium chloride were purchased from Alfa Aesar (Ward Hill, MA, USA) with purity greater than

99.5%. Potassium chloride and potassium phosphate were received from MP Biomedicals (Santa Ana, CA, USA). Magnesium chloride was used after purification through extraction with ethyl acetate to remove surfactants. The pure water utilized was from an Elga Ultrapure water purifier with a resistivity of 18 MΩ·cm, surface tension of 72.4 mN m^{-1}, and pH 5.6 at 20.0 ± 0.5°C.

Isotherm and IRRAS measurements transpired in a clean room (Class 1000) with a constant temperature of 20.0 ± 0.5°C and humidity of 50 ± 1%. All isotherms were obtained on a Kibron μ-trough S (Kirbon Inc., Helsinki, Finland) with an area of 5.9 x 21.1 cm^2. The surface pressure was recorded through use of the Wilhelmy method with an alloy wire probe possessing a sensitivity of ± 0.01 mN m^{-1}. Surface potential was monitored through used of a Kelvin probe with an accuracy within 10 mV.

IRRAS measurements of the AFU monolayer were obtained on an EQUINOX 55 Fourier transform infrared spectrometer (Bruker Optics, Billerica, MA, USA), connected to an XA-511 external reflection accessory containing a mercury-cadmium-telluride detector cooled with liquid nitrogen. Each measurement contains a spectrum that reflects the aggregate of 1200 scans and 8 cm^{-1} resolution. The spectrometer used p-polarized light and the spectra are represented without any baseline correction.

3.2.2 Langmuir monolayer preparation

AFU concentration was determined using the certificate of analysis provided from Sigma for the specific lot of AFU (SLBL8171V) which had a protein concentration of 0.77 mg of protein/mL. Using the molecular weight of AFU (which Sigma indicates is between 210-220 kDa) a solution of 0.08 mg/mL AFU was produced in citrate/phosphate leading to ~ 0.01nmol of AFU in a 20 μL injection. Subphases used were pure deionized

water, phosphate buffer saline (137 mM NaCl, 2.7 mM KCl, 10 mM Na_2HPO_4, 1.8 mM KH_2PO_4), citrate/phosphate buffer (0.1 M Citric Acid, 0.2 M Na_2HPO_4, 30 mM NaCl, 8 mM $MgCl_2$, 1 μM NaN_3), 0.5 M NaCl and 0.5 M KCl. Upon deposition, the AFU Langmuir monolayer was given 20 minutes to reach equilibrium. The surface pressure- and potential-area isotherms were produced by compressing the AFU Langmuir monolayer at a rate of 10 cm^2/minute. Each experiment was reproduced in triplicate.

3.2.3 Infrared reflection-absorption spectroscopy measurements

To begin infrared reflection-absorption spectroscopy, the optimal angle of reflection must be determined. The AFU Langmuir monolayer is prepared as described as above, then the barriers were compressed until a surface pressure of 20 mN m^{-1}. Upon reaching 20 mN m^{-1}, scans were taken in 5° increments from 35° to 70°. The optimal angle was determined to be 40°, due to the favorable signal and low noise observed in the amide I region.

3.2.4 Antibody injection measurements at the air-water interface

AFU monolayers were prepared by spreading 0.01 nmol of AFU onto a citrate/phosphate buffer (pH 5.5) subphase and allowing 20 minutes for the Langmuir monolayer to form. The AFU monolayer was then compressed to a pressure of 10 mN m^{-1} and the barriers were halted. 20 μL of FUCA2 was then injected into the subphase outside of the barriers in a 1:1 or 1:2 ratio [AFU:FUCA2 (mol/mol)]. The pressure was monitored over a period of ~4-5 hours, until saturation occurred and the pressure remained constant. Control results were obtained using human IgG (MP Biomedicals) prepared as a 1% (w/v) solution in PBS. 20 μL of human IgG was

injected in the same manner as FUCA2. After 4 hours, there was no observed increase in surface pressure.

3.3 Surface chemistry of an Alpha-L-Fucosidse Langmuir monolayer

3.3.1 Buffer optimization

To further understand the benefits of alpha-L-fucosidase as a biomarker for hepatocellular carcinoma, its physical properties and interaction with an anti-alpha-L-fucosidase (FUCA2) IgG were observed at the air-water interface. AFU monolayers were prepared by depositing 0.01 nmol evenly onto a citrate/phosphate buffer subphase. A citrate/phosphate buffer at pH 5.5 was chosen for the ideal subphase after completing a salt and pH effect of the AFU isotherm. Surface pressure-area measurements were first carried out by depositing AFU onto pure water, phosphate buffer saline (PBS), citrate/phosphate buffer, 0.5 M KCl, and 0.5 M NaCl. The only subphase that could produce an isotherm was the citrate/phosphate buffer, as all the other subphases yielded no change in surface pressure, indicating no monolayer was formed. The subphase was further probed by measuring the effect of pH by adjusting the pH of the citrate/phosphate buffer to 2, 5.5, 7 and 10. As shown in **Figure 3.1**, there is a correlation between the collapse pressure and the pH. The AFU monolayer experiences its highest collapse at roughly 43 mN m^{-1} at a pH of 2, with the collapse occurring at roughly the same area as pH 5.5. Using neutral and basic subphases produces less stable monolayers, as collapsing occurred at lower area and pressures than in an acidic subphase. The lack of stability in the neutral and basic subphases is likely a result to the charge state of protein. While a pI value for AFU has not been calculated, most proteins experience acidic pI and AFU is likely

not an exception. Therefore, the strong contrast in the monolayer formed at pH 7 and 10 compared to pH 2 and 5.5 is likely attributed to a conformational change in AFU that occurs when the protein becomes less protonated. AFU expresses optimal activity at pH 5.5 so these conditions were chosen for further measurements.

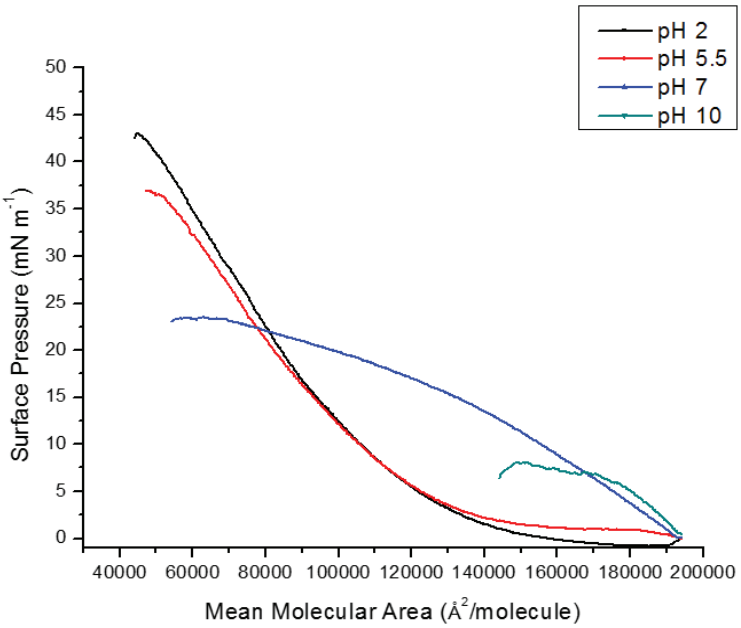

Figure 3.1 Surface pressure-area isotherm of AFU monolayer on a citrate/phosphate buffer of pH 2 (black), 5.5 (red), 7 (blue) and 10 (green).

3.3.2 Surface pressure-area and surface potential-area isotherms

Figure 3.2 displays the surface pressure- and surface potential-area isotherms. Upon barrier compression, an immediate increase is observed as the AFU monolayer compresses from a gaseous state into the liquid expanded state (**Figure 3.2**). At 185,000 Å^2/molecule, the isotherm steadies out, indicating a coexistence between the liquid expanded and liquid condensed state until approximately 150000 Å^2/molecule, when a transition to the liquid condensed state occurs. By extrapolating the isotherm from the linear portion of the liquid condensed state, the limiting molecular area is found to be

118000 Å^2/molecule. The isotherm's collapse is not prominent but can be estimated by the change of curvature at a surface pressure of ~38 mN m^{-1}.

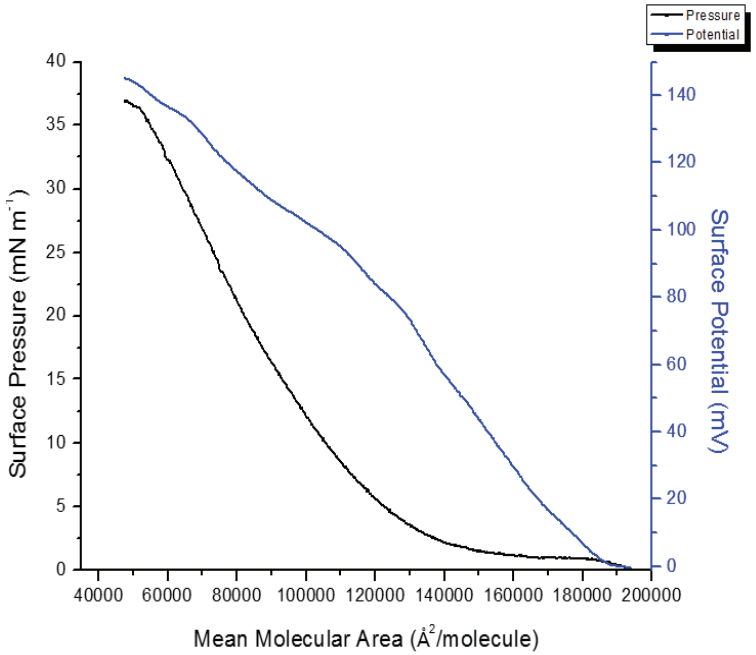

Figure 3.2 Surface pressure-area isotherm (black) and surface potential-area isotherm (blue) of AFU Langmuir monolayer on citrate/phosphate buffer subphase.

A correlation between the surface pressure- and surface potential-area isotherms is observed. While the surface pressure is limited to primarily van der Waals interactions of molecules in close contact, the surface potential measures dipole-dipole interactions, which can be detected over greater distances.[138] Upon compression, an increase in surface potential is observed. This is expected, as the monolayer is of an enzyme possessing charge from the amino acid side changes. Before compression, the electrode is nil with the monolayer expanded to its maximum distance. Compression immediately brings these molecules closer to the electrode, resulting in a jump in potential. The surface potential isotherm presents a liquid expanded film from 155,000 to 118,000 Å^2/molecule, followed by a phase transition kink at 118,000, which is followed by a

liquid condensed film up to the collapse surface pressure at about 60,000 $Å^2$/molecule. The slope of the surface pressure isotherm correlates with the surface potential during the liquid expanded phase, until around 20 mN/m when the phase transition occurs. The more sensitive surface potential measurements are able to identify the transition from liquid expanded to liquid condensed while the surface pressure fails to distinctly identify this transition.

3.3.3 Compression-decompression and stability measurements

The AFU monolayer was further tested by performing compression-decompression cycles, as well as, a constant pressure stability measurement (**Figure 3.3**). Compression-decompression cycles were carried out at surface pressures of 10, 20 and 30 mN m^{-1}. All three pressures expressed hysteresis, which one would expect as molecules can orient into more favorable orientations upon compression, leading to a decrease in the initial mean molecular area and a lagging on the decompression. Minimal differences were found in the mean molecular area at the maximum compression pressure for each cycle as there was a 4.8, 1.9, and 9.4 % change for 10, 20, and 30 mN m^{-1}, respectively. One would expect to see an increase in the differences in mean molecular area as the surface pressure is increased. However, this trend was broken at 20 mN m^{-1} for AFU. This small deviation is within the error of the experiment, but a more likely cause for the anomaly is that this surface pressure happens to be the point at which the AFU monolayer transitions from liquid expanded to liquid condensed, which is likely causing the deviation from the typical trend. Another prominent observation from the compression-decompression cycles is contributed to the surface pressure dropping to

0 mN m^{-1} as the barriers approach the initial maximum area, which is indicative that no aggregates were formed.

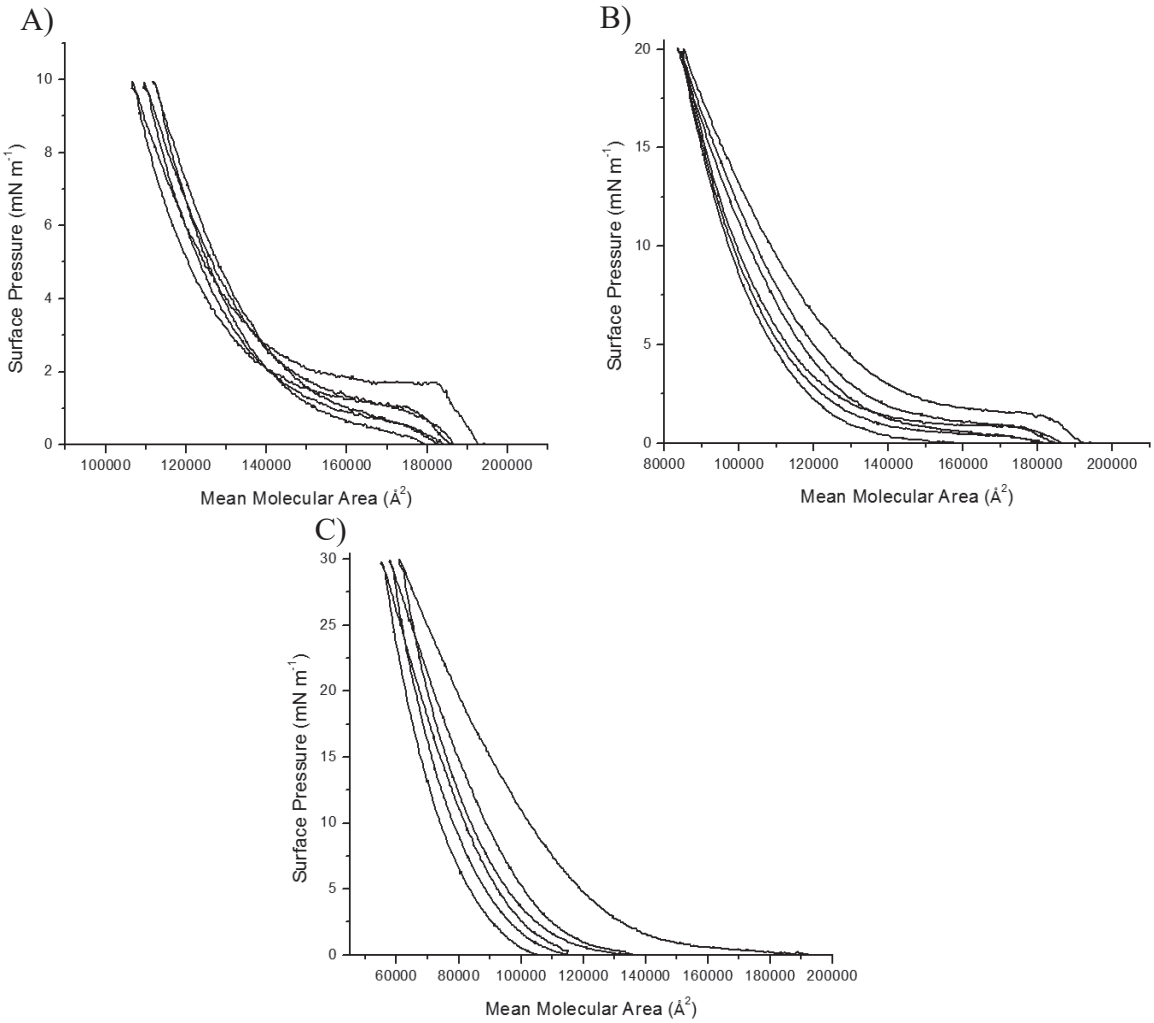

Figure 3.3 Compression-decompression cycles of AFU monolayer on citrate/phosphate buffer subphase (pH 5.5) as surface pressures of (A) 10 mN m^{-1} (B) 20 mN m^{-1} and (C) 30 mN m^{-1}.

As 20 mN m^{-1} is roughly the halfway point to the monolayers collapse pressure, this pressure was used to perform stability measurements. The monolayer was compressed to 20 mN m^{-1} and over the course of 90 minutes a 17.8% change in mean molecular area was observed. The change in mean molecular area over time is likely attributed to the monolayer adopting a more favorable orientation. Prior to compression,

the monolayer will possess holes or molecules that are not ideally oriented. Over time, the molecules will adjust to the most favorable conformation, leading to a decrease in area as imperfections are etched from the monolayer. The time of 90 minutes was chosen because this is the approximate amount of time required to do spectroscopy measurements of the AFU monolayer. The surface compressibility was calculated from the equation: $\frac{1}{k_T^S} = \frac{1}{(\frac{K_T^S}{A})} = -\frac{1}{\frac{(\frac{\partial A}{\partial \pi})_T}{A}}$, where K_T^S is the surface compressibility at a constant temperature T, A is the area, and π is the surface pressure.[139] **Figure 3.4A** displays the inverted surface compressibility at various surface pressures. A net decrease in inverted compressibility is observed as a function of surface pressure. As the plot is inverted, this translates to an increase in the compressibility of the AFU Langmuir monolayer as a function of increasing surface pressure.

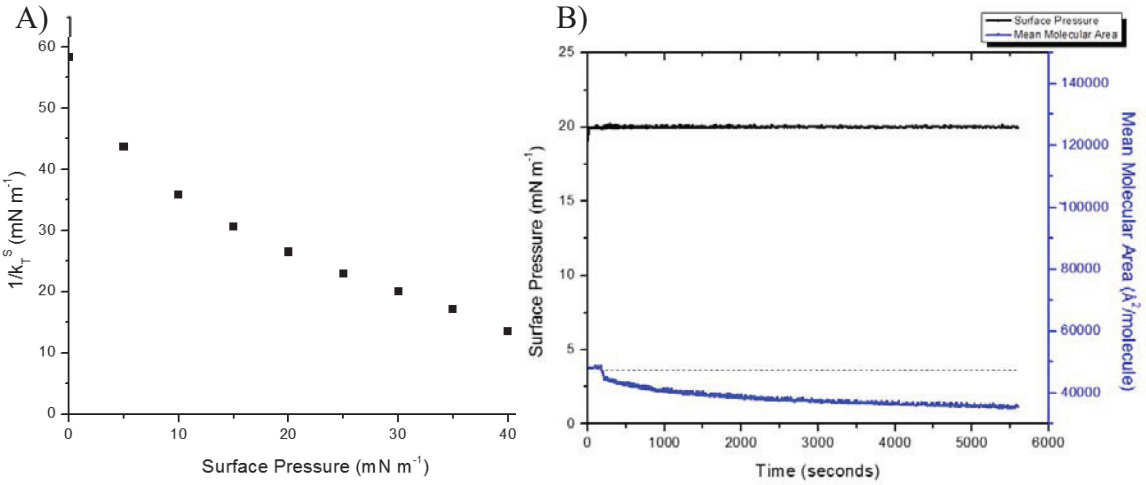

Figure 3.4 (A) Inverse isothermal compressibility. (B) Stability measurement at constant pressure of 20 mN m^{-1}.

3.3.4 Infrared reflection-absorption spectroscopy of alpha-L-fucosidase Langmuir monolayer

The optimal angle for IRRAS measurements was determined by scanning a range of angles on an AFU monolayer compressed to a surface pressure of 20 mN m^{-1}.

Subsequent IRRAS measurements were obtained at an angle of 40° using p-polarized light, as this spectrum displayed the highest resolution in the desired area of analysis (Amide I and Amide II (1500-1700 cm^{-1}). For better peak clarity, the IRRAS spectra of the AFU Langmuir monolayer was split into two main regions of focus: 2700-3200 cm^{-1} where C-H stretching is observed, and 1400-1700 cm^{-1} where peaks relative to the protein's secondary structure and amino acid side chains appear. **Figure 3.5** displays the IRRAS spectra focused on the C-H stretching of the AFU Langmuir monolayer, where three distinct peaks occur. The peaks formed at 2855 and 2925 cm^{-1} can be assigned to the antisymmetric and symmetric stretches of sp^3-hybridized C-H groups. The presence of sp^3-hybridized peaks existing at different wavenumbers is to be expected, as there are a large number of C-H molecules found throughout the amino acid sequences of proteins. The presence of the sp^2-hybridized C-H stretch at 3031 cm^{-1} is also expected, as amino acids, such as tyrosine and tryptophan, would contain aromatic protons. As portrayed in **Figure 3.5a**, there is an overall increase in the band intensity as a function of surface pressure. This trend is expected, as compressing the barriers will force more individual molecules of AFU towards the center of the trough, and therefore, more molecules will be probed by the IRRAS measurement, leading to higher resolution of the

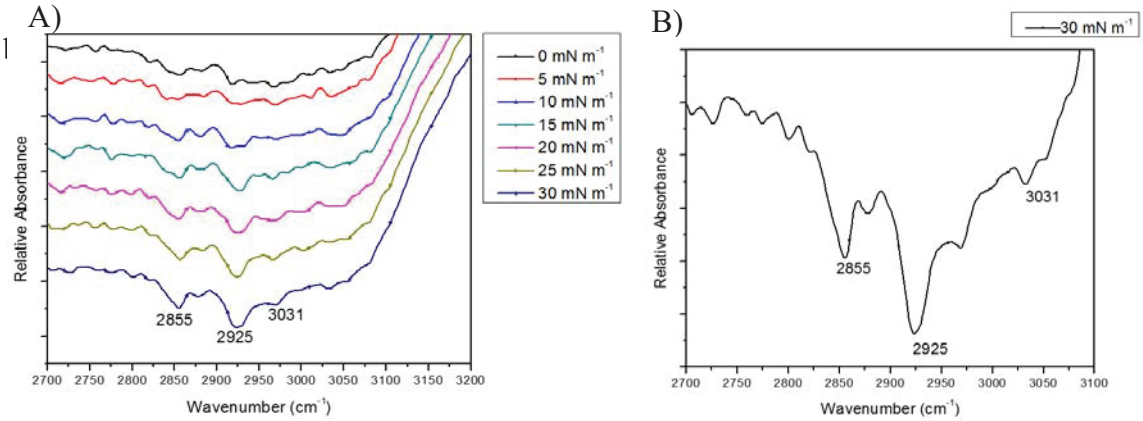

Figure 3.5 IRRAS spectra of the C-H stretching of the AFU Langmuir monolayer at (A) increasing surface pressures and (B) a zoomed profile at 30 mN m^{-1}.

Amide I (1700-1600 cm^{-1})		Amide II (1600-1500 cm^{-1})	
Band Position	**Assignment**	**Band Position**	**Assignment**
A) 1679	β-turn	D) 1567	N-H **b** (60%); C-N ν_s, C-O **b**, C-C ν_s, C-N ν_s (40%)
B) 1655	α-helix	E) 1542	N-H **b** (60%); C-N ν_s (40%) of α-helix
C) 1614	β-sheet	F) 1524	N-H **b** and C-N ν_s from β-sheet

Table 3.1: IRRAS band assignment for the functional group region (1500-1700 cm^{-1}) of the **AFU** Langmuir monolayer.

The next area of analysis for the IRRAS spectra (**Figure 3.6**) is one of the most important regions for analyzing proteins because it contains Amide I (1600-1700 cm^{-1}), where C=O stretching occurs, and Amide II (1500-1600), where predominantly N-H bending occurs. Amide I and II are of particular importance, because the signals observed make up the backbone of the protein and thus give insight into the protein's secondary structure. In observing Amide I, one would expect to see C=O stretching indicative of α-helix, β-sheet, or random coil. However, it is possible that there is overlap in these peaks causing them to be missed in the overall spectrum. **Table 3.1** displays the assignment of the bands formed from the AFU Langmuir monolayer.[140-143] The most prominent peak in this region is found at 1679 cm^{-1} is indicative of β-turn, which is further confirmed by the slight peak at 1614 cm^{-1} for a β-sheet, as well as the band at

1524 cm^{-1} where bending of N-H occurs for the β-sheet. The last observable peak in the Amide I region is at 1655 cm^{-1}, where α-helix C=O stretching occurs.

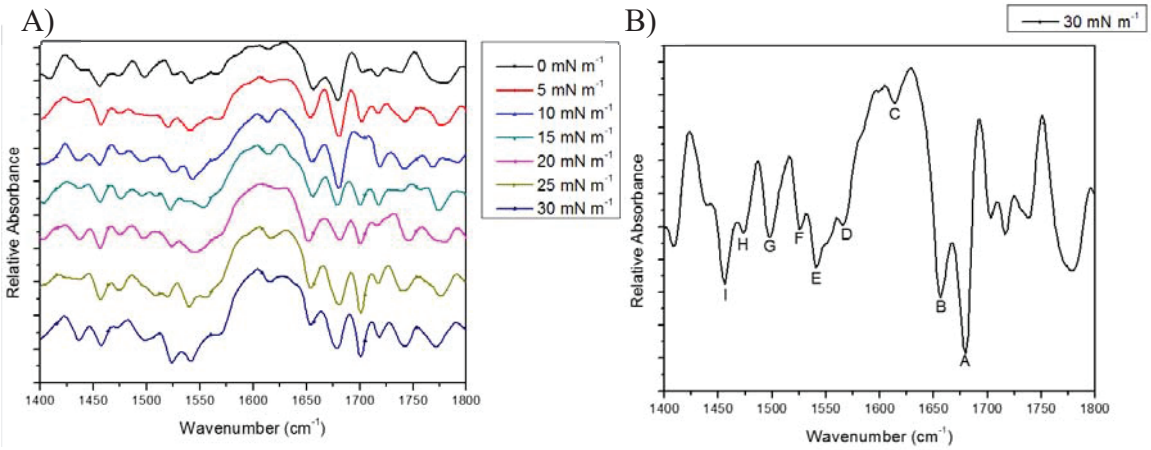

Figure 3.6 IRRAS spectra of the carbonyl region of the AFU Langmuir monolayer at (A) increasing surface pressures and (B) a zoomed profile at 30 mN m^{-1}.

3.4 Interaction of alpha-L-fucosidase Langmuir monolayer with FUCA2 antibody injected into subphase

3.4.1 Surface chemistry of FUCA2 antibody

Prior to monitoring the interaction of the FUCA2 antibody with the AFU Langmuir monolayer, baseline measurements of the FUCA2 Langmuir monolayer were surveyed. The main objective is to observe any changes that may occur to the AFU Langmuir monolayer upon injection of FUCA2 into the subphase. However, the mean molecular area of the FUCA2 Langmuir monolayer must be established to observe if there is any overlap in the formation of a FUCA2 Langmuir monolayer with that of the AFU Langmuir monolayer. As shown in **Figure 3.7**, the FUCA2 Langmuir monolayer forms a stable isotherm upon deposition onto a citrate/phosphate buffer subphase. Upon compression, an initial lift is observed at 28000 $Å^2$/molecule. This is well outside of the range at which the AFU Langmuir monolayer is produced, which is reasonable

considering AFU is significantly larger than the FUCA2 antibody. The FUCA2 Langmuir monolayer experiences a collapse at ~40 mN m^{-1} and a limiting mean molecular area of 28,000 $Å^2$/molecule.

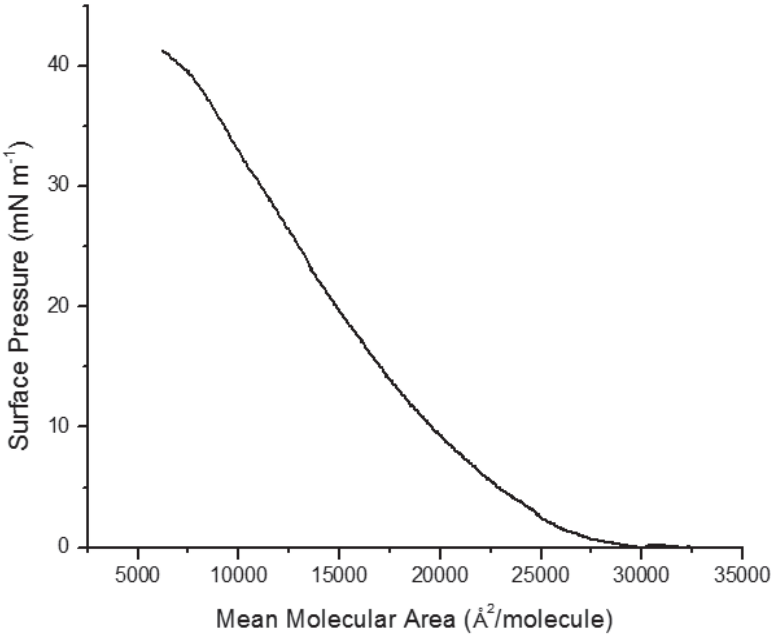

Figure 3.7 Surface pressure-area isotherm of FUCA2 Langmuir monolayer on a citrate/phosphate buffer subphase (pH5.5).

3.4.2 Injection of FUCA2 into alpha-L-fucosidase Langmuir monolayer

The AFU Langmuir monolayer was probed with the injection of the FUCA2 immunoglobulin. Developing a sensitive assay is often enhanced by implementing specific antibodies. The interaction between the antibody and enzyme can be observed at the air-water interface. Upon injecting the antibody into an already compressed subphase, one would expect to see a rise in the surface pressure if the antibodies rise from the subphase to interact with the AFU Langmuir monolayer, while if no interaction is observed a decrease in pressure will be observed over time. **Figure 3.8** contains the results of a 1:1 and 1:2 molar injection of FUCA2. In both cases, the barrier was compressed until the surface pressure reached 10 mN m^{-1} prior to injecting

the antibody. An initial drop in surface pressure is observed as the monolayer reorients into more favorable orientations and some molecules dissolve into the subphase. However, after ~1 hour the surface pressure begins to rise as FUCA2 begins to interact with the AFU Langmuir monolayer. A slight difference can be observed through increasing the concentration of FUCA2, as using a 2-molar excess caused the surface pressure to raise up to 18 mN m^{-1}, while using a 1:1 ratio yields a rise in surface pressure up to 16 mN m^{-1}.

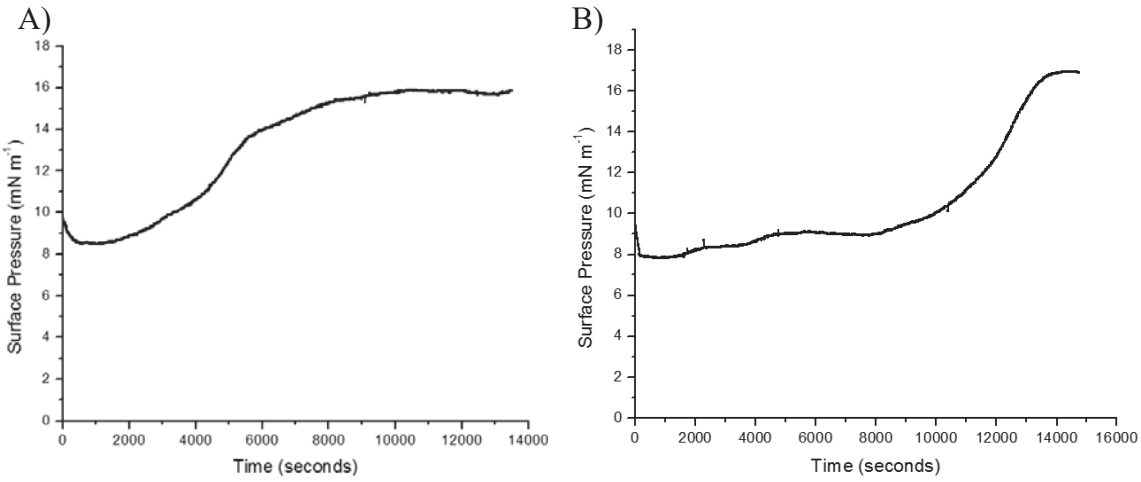

Figure 3.8 Pressure change after injection of FUCA2 with (A) 1:1 ratio and (B) 1:2 ratio.

3.4.3 Infrared reflection-absorption spectroscopy on FUCA2 injection into an alpha-L-fucosidase monolayer

The interaction between FUCA2 and the AFU Langmuir monolayer was also monitored through IRRAS. **Figure 3.8** displays the spectra monitored over the course of 300 minutes. A large change in the spectra is observed at ~90 minutes. A zoomed profiled of the first 90 minutes after injection shows only the spectra corresponding to the AFU Langmuir monolayer. After 90 minutes, the peak intensity experiences a large change. This roughly corresponds to the point in **Figure 3.6** where the surface pressure

begins to increase as FUCA2 is interacting with the AFU Langmuir monolayer. Furthermore, three additional stretches are observed at 1696, 1669 and 1634 cm^{-1}. The peak at 1696 cm^{-1} is in the upper end of a β-turn stretch and this assignment is further confirmed by the presence of a β-sheet peak at 1634 cm^{-1}. The final remaining additional peak at 1669 cm^{-1} is from the α-helix of the FUCA2 antibody.

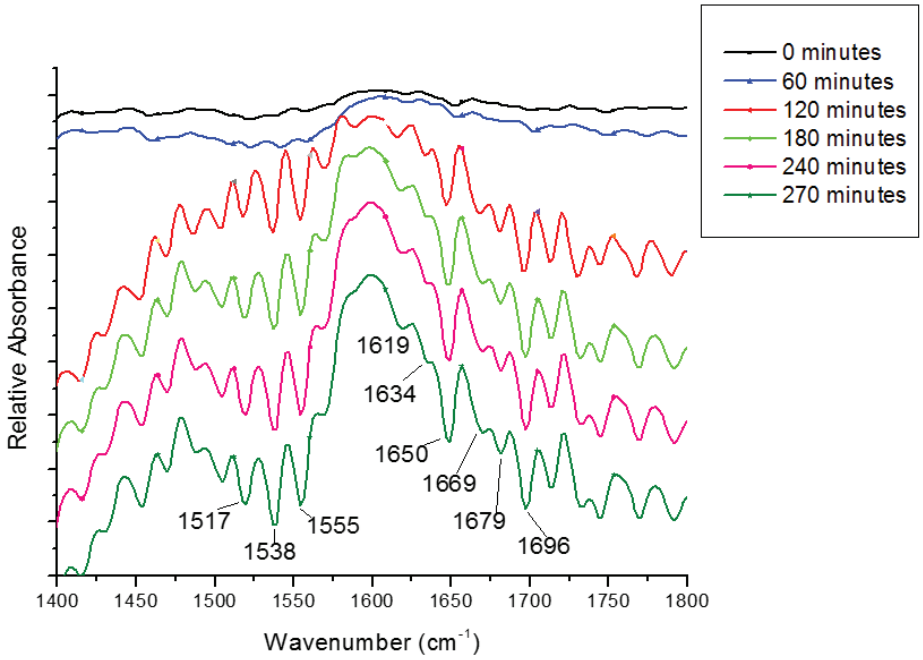

Figure 3.8 IRRAS spectra of AFU Langmuir monolayer after injection of FUCA2 in a 1:1 ratio.

3.5 Summary

In summary, AFU can form a stable Langmuir monolayer at the air-water interface. AFU proved to be sensitive to conditions, as varying salt content and pH of the subphase lead to drastic changes in the Langmuir monolayer. Under the proper conditions, no aggregation is formed and the monolayer is stable over time. An interaction between AFU Langmuir monolayer and an antibody (FUCA2) was confirmed at the air-water interface.

Chapter 4

Quartz Slide Immunoassay for Detection of Alpha-L-Fucosidase

4.1 Background

Developing a biosensor for the detection of AFU has not been a facile task. The most common approaches for assays to detect serum AFU are based upon the enzymatic properties of AFU.[144] Enzyme-based colorimetric assays are capable of detecting a desired antigen, however, the sensitivity of detection is low.[68,145] One way in which antigen detection can be made more sensitive is to incorporate antibodies. The IgG anti-FUCA2 is an antibody that has specificity towards AFU. After observing the interaction of anti-FUCA2 with AFU at the air-water interface in the previous chapter, it was confirmed that the antibody displayed specificity towards AFU binding and could be used in assay development.

Incorporating monoclonal antibodies can improve the detection sensitivity of an assay, however, it can also greatly increase the cost. Monoclonal antibodies are typically produced through a hybridoma method, which is a time consuming and expensive procedure.[146] To reduce the amount of IgG needed to run an assay, the antibody can be immobilized on a solid support, similar to an ELISA.[147] Another common surface modification technique such as encapsulation (sol-gel process)[148,149] can provide a distinct advantages in that it allows for much higher loading than flat surface immobilization.[150,151] However, the encapsulated gel suffers from slow response time that is dependent upon the analytes diffusion into the gel.[152-154]

To avoid long response times, the detection of AFU using the anti-FUCA2 antibody was developed on a quartz slide. Quartz exhibits favorable optical properties

for spectroscopic measurements and the conjugation techniques have been previously investigated.[155-157] A wide range of silane derivatives can be used for surface modification, allowing for a multitude of further functionalization approaches available.[158-160] The ensuing chapter investigates the development of an immunoassay immobilized on a quartz surface. Several different conjugation approaches were investigated to optimize the binding and packing of the anti-FUCA2 antibody on the quartz surface. Upon determining the optimal conjugation conditions, the quartz slide immunoassay was then used to detect AFU in PBS.

4.2 Experimental

4.2.1 Materials and methods

(3-aminopropyl) trimethoxysilane, (3-mercaptopropyl) trimethoxysilane, fluorescein isothiocyanate and anhydrous toluene were obtained from Alfa Aesar (Ward Hill, MA, USA). Glutaraldehyde and bovine IgG were received from MP Biomedicals (Santa Ana, CA, USA). Rhodamine 6G-succinimidyl ester, 1-mercapto-3,6,9,12,15,18,21,24,27,30,33,36-dodecaoxanoatrriacontan-39-oic acid [CT(PEG)12] and succinimidyl-([N-maleimidopropionamido]-dodecaethylene glycol) ester [SM(PEG)12] were acquired from Thermo Fisher Scientific Inc. (Weston, FL, USA). Alpha-L-fucosidase and diethylthiocarbamoyl chloride were purchased from Sigma Aldrich (St. Louis, MO, USA). FUCA2 antibody was obtained from Abgent (San Diego, CA, USA). The pure water utilized was from an Elga Ultrapure water purifier with a resistivity of 18 MΩ·cm, surface tension of 72.4 mN m^{-1}, and pH 5.6 at 20.0 ± 0.5°C.

4.2.2 Quartz slide cleaning procedure

Prior to functionalizing the quartz surface, the slide was cleaned and activated for more favorable binding chemistry. First, the slide was sonicated with ultrapure deionized water for five minutes. The slide was rinsed thoroughly with water to ensure all debris or dust had been removed from the surface of the slide. Next, the slide was rinsed five times with acetone, then put in a vial filled with acetone and placed under sonication. After 20 minutes, the acetone was removed and the slide was rinsed in the vile with acetone five times. The cleaning with acetone was repeated two additional times. Next, the slide was submerged into a 1 M potassium hydroxide solution and sonicated for one hour. The slide was then rinsed thoroughly with ultrapure deionized water. Once dry, the slide was added to a Piranha solution prepared by mixing sulfuric acid and hydrogen peroxide in a 3:1 volumetric ratio [3:1 H_2SO_4:H_2O_2 (v/v)]. The slide incubated in the piranha solution until bubbles no longer formed, then the piranha solution was discarded, and the slide was rinsed with ultrapure deionized water. The cleaning with piranha was repeated one additional time and the slide was then stored under methanol or immediately used for further functionalization.

4.2.3 Quartz slide silanization

The cleaned quartz slide was dried thoroughly under argon, then placed into a fresh vial with a stir bar and sealed with a septum. The vial was flushed of air and placed under an argon atmosphere. Next, a silanization solution was prepared by adding 20 mL of anhydrous toluene and 0.5 mL of either (3-aminopropyl) trimethoxysilane or 0.5 mL of (3-mercaptopropyl) trimethoxysilane. Acetic acid (2 mL) was added to catalyze the hydrolysis and the hydrolysis was initiated by sonicating the vial for one minute, then

leaving it to incubate overnight (~18 h). The slide was then removed from the silanization solution, rinsed thoroughly with toluene three times, then methanol three times and dried under a gentle stream of argon. Silanized quartz slide could be stored in methanol under inert atmosphere or immediately used for further functionalization.

4.2.4 Quartz slide functionalization with isothiocyanate

A quartz slide prepared with a (3-aminopropyl) trimethoxysilane silanization solution was placed into a 1.5 % (w/v) solution of diethylthiocarbamoyl chloride in acetonitrile and refluxed for 16 hours. The slide was then removed and rinsed in triplicate with acetonitrile, dichloromethane, and methanol. The slide was then dried with a gentle stream of argon and stored in methanol or immediately used for further functionalization.

4.2.5 Quartz slide functionalization with glutaraldehyde

For glutaraldehyde functionalization, a quartz slide prepared with (3-aminopropyl) trimethoxysilane silanization solution was incubated in a solution of 25% (w/v) glutaraldehyde in water for four hours at room temperature. The slide was then removed from the glutaraldehyde solution and washed with ultrapure deionized water three times. Glutaraldehyde functionalized quartz slide was then stored in methanol or immediately used for further functionalization.

4.2.6 Quartz slide functionalization with thiol

Thiol functionalization proceeded using a quartz slide prepared with (3-mercaptopropyl) trimethoxysilane as the silanization solution. The slide immersed in a solution prepared by dissolving 20 mg of the bifunctional linker, N-succinimidyl 3-maleimidopropionate, in a minimal amount of dimethyl sulfoxide with 20 mL of absolute

ethanol. The vial was sealed and argon was bubbled into the solution for approximately five minutes. The slide was left under an argon atmosphere and stirred at room temperature for two days. Upon completion, the slide was removed and rinsed with methanol thoroughly, then dried under a gentle stream of argon. The slide was then stored in methanol or immediately used for further functionalization.

4.2.7 Quartz slide functionalization with carboxy-PEG12-thiol

Functionalization with carboxy-PEG12-thiol proceeded with a quartz slide prepared with (3-aminopropyl) trimethoxysilane for the silanization solution. The slide was deposited into a round bottom flask containing N-hydroxysuccinimide (NHS) and 1-ethyl-3-(3-dimethylaminopropyl) carbodiimide (EDC), dissolved in 2-(N-morpholino) ethane sulfonic acid (MES) buffer (pH 4-5). The slide was left stirring at room temperature for one and a half hours. Carboxy-PEG12-thiol [$CT(PEG)_{12}$] was dissolved in a minimal amount of dimethyl sulfoxide (~1 mL). 100 µL of $CT(PEG)_{12}$ was added to the flask and it was left to stir at room temperature for two days. Next, the slide was removed and rinsed with methanol three times and dried under a gentle stream of argon. The slide was then placed into a 5 mM solution of N-succinimidyl-3-maleimidopropionate in absolute ethanol. After 2 days, the slide was removed and rinsed thoroughly with methanol, then dried under a gentle stream of argon. The CT(PEG)12 quartz slide was stored in methanol or immediately used for further functionalization.

4.2.8 Quartz slide functionalization with succinimide-PEG12-maleimide

To proceed with NHS-PEG12-maleimide [$SM(PEG)_{12}$] functionalization, a quartz slide prepared with (3-mercaptopropyl) trimethoxysilane for the silanization solution was added into a solution containing 100 µL of $SM(PEG)_{12}$ in 20 mL of absolute ethanol.

The slide was left stirring in this solution for two days at room temperature, then removed and rinsed thoroughly with methanol before being dried under a gentle stream of argon. SM(PEG)12 functionalized quartz slide was stored in methanol or immediately used for further functionalization.

4.2.9 Quartz slide conjugation with antibody

After functionalization from any method between ***4.2.4*** and ***4.2.7***, the dried quartz slide was placed into a solution containing 0.1 mg/mL of antibody (either bovine IgG or anti-FUCA2) in PBS and stirred for one hour at room temperature, followed by 2 days at 4° C.

4.2.10 Quartz slide conjugation with optical probe

Upon completing antibody binding (***4.2.9***), the quartz slide was rinsed thoroughly with ultrapure deionized water, then sonicated in PBS for 15 minutes. The PBS was removed and the slide was rinsed five times with ultrapure deionized water. The slide was placed back under sonication in PBS two additional times, for a total of three rinse cycles with PBS. Next, the slide was added to a solution containing 100 µL of the probe [fluorescein isothiocyanate (FITC) or rhodamine 6G-succinimidyl ester (rhodamine 6G)] dissolved in 15 mL of PBS. The slide was stirred at room temperature for 90 minutes, then the slide was moved to 4° C and incubated for two additional days.

4.2.11 Quartz slide assay for detection of alpha-L-fucosidase

Upon conjugation of the probe (***4.2.10***), the quartz slide was ready for the assay. The assay was run by first obtaining a baseline fluorescent measurement of the probe conjugated to the slide in PBS. The slide was then incubated in 5, 10, 25, 50, 75, 100, 125, and 150 µM AFU for 30 minutes at 37° C. After the first incubation at 5 µM, the

slide was scanned at the probe emission wavelength (ex. 495 nm) and the concentration of AFU was increased to the next concentration. The incubation and scanning was repeated until eight data points were obtained for a linear extrapolation to be plotted.

4.3 Quartz slide assay optimization with bovine IgG

To detect human alpha-L-fucosidase in human blood serum, a quartz slide assay was proposed, utilizing an antibody conjugated to a fluorescent probe for sensitive detection. A quartz plate was chosen for the solid support surface due to its lack of interference with spectroscopy measurements and well-known functionalization chemistry. Prior to functionalizing the slide, it must be properly cleaned and activated. Cleaning was done by sonicating the slide in water and then acetone, to remove any physical materials or dust that could be on the slide surface. The slide was then sonicated in 1M KOH, which causes minor etching into the quartz slide surface. Slight etching was found to improve further functionalization steps by improving the packing. However, too much etching could lead to scratches and interfere with the optical properties of the quartz slide. A time of one hour was found to be ideal for adding slight etching without disrupting the optics of the slide. Finally, the slide was activated by treatment with strong oxidizing acid systems to saturate the surface with hydroxyl groups. The best system for achieving this was found to be piranha solution produced from 3:1 (v/v) H_2SO_4:H_2O_2.

4.3.1 Isothiocyanate functionalization

In developing an immunoassay on a solid support, many potential conjugation pathways can be utilized. Common binding moieties intrinsic to antibodies are typically found from primary amines of the amino acid lysine. Primary amines possess favorable

reactivity with many types of functional groups. A well-established method of conjugation with biomolecules was attempted using isothiocyanate moieties. Isothiocyanate reacts with primary amines to produce a covalently stable thiocarbamide. By functionalizing a solid support with terminal isothiocyanate groups, it is possible to covalently immobilize an antibody to the solid support, via lysine residues from the antibody.

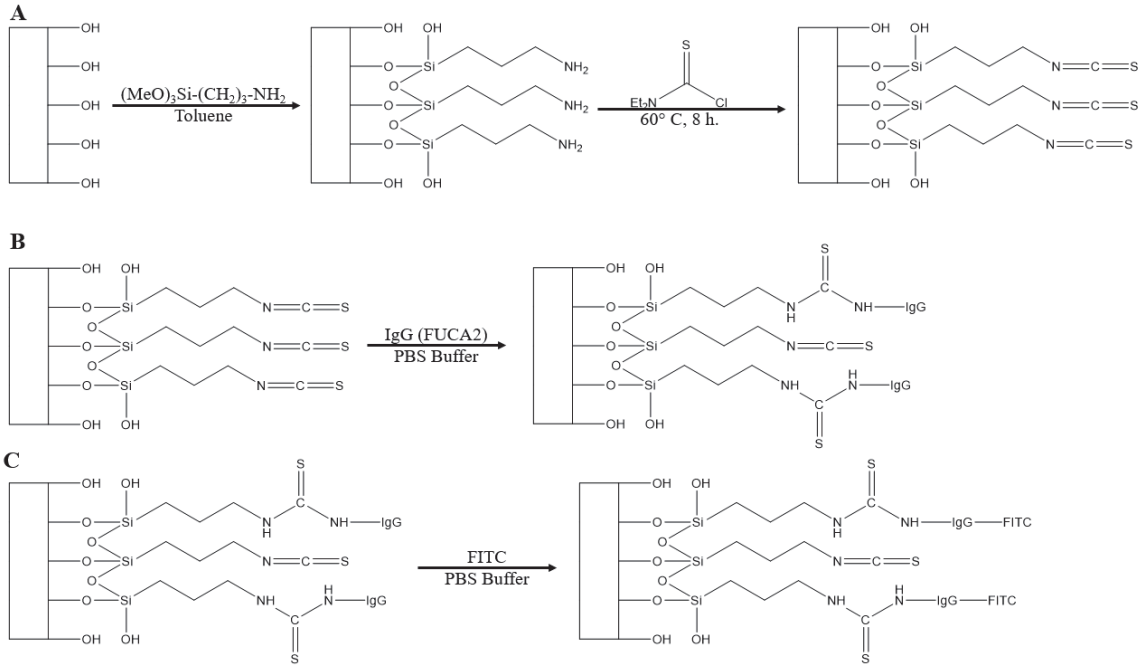

Scheme 4.1 Quartz surface modification: (A) Amino-modified quartz and conversion to isothiocyanate; (B) mutant IgG (FUCA2) immobilization; (C) IgG labeling with FITC.

To prepare an isothiocyanate functionalized quartz slide, the slide must be cleaned and activated as described above. After treatment with piranha solution, the quartz slide surface becomes saturated with hydroxyl groups (**Scheme 4.1A**). These hydroxyl groups have been found to undergo hydrolysis in the presence of alkyloxysilane derivatives, which provides an approach at adding further functionality to the quartz surface. For preparing an isothiocyanate functionalized quartz slide, the alkyloxysilane derivative

implemented was (3-aminopropyl) trimethoxysilane. Upon hydrolysis, the silane forms a covalent bond with hydroxyl groups and the methoxide is displaced and converted to methanol in the acidic solution. A three-carbon spacer was utilized to add some distance from the quartz surface and to improve the packing on the slide surface. Terminating the propyl spacer is a primary amine, which allows for further functionalization.

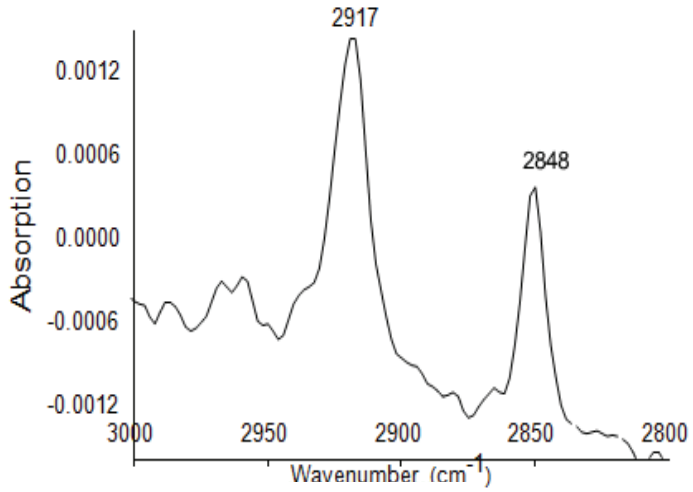

Figure 4.1 ATR-FTIR spectrum of silanized quartz slide.

To gain isothiocyanate functionality, the primary amine exposed from the trimethoxysilane derivative on the quartz slide was treated with diethylthiocarbamoyl chloride. However, before further functionalization can occur, the quartz slide must be checked to determine the silanization process was successful. This was achieved by scanning the slide using attenuated total reflection Fourier transform infrared spectroscopy (ATR-FTIR). Prior to silanization, the quartz slide surface was solely saturated with hydroxyl groups and the ATR-FTIR scan shows only broad stretching ~3600 cm^{-1} from the O-H stretching. Upon treatment with (3-aminopropyl) trimethoxysilane, not only was there a noticeable reduction in the stretching intensity of the O-H groups, there are additional peaks added to the spectrum from the presence of

new C-H stretching frequencies from the alkyl groups added to the slide from the propyl spacer. As portrayed in **Figure 4.1**, sharp absorption peaks are observed at 2917 and 2848 cm^{-1}, which are indicative of the presence of C-H stretching on the quartz surface, thus proving the silanization proceeded as intended.

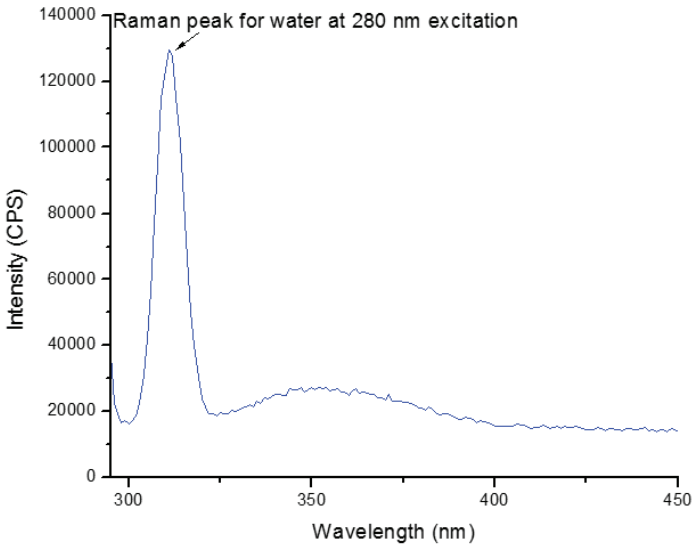

Figure 4.2 Fluorescence spectrum of isothiocyanate functionalized quartz slide with bovine IgG. (excitation 280 nm, slits: 5,5 nm).

After confirming the silanization reaction, the slide was refluxed with diethylthiocarbomyl chloride dissolved in acetonitrile for 16h. Diethylthiocarbamoyl chloride has a thiocarabamide, which is desirable for producing an isothiocyanate bond, along with two good leaving groups which allow the thiocarbamide to be added to the end of the primary amine, yielding an isothiocyanate functional group.

At this point, the slide was ready for antibody conjugation. To validate the proposed methodology, bovine IgG was chosen as a model antibody to observe if immobilization to the quartz slide was successful. To bind the antibody, the slide was placed into a solution of 1 mg/mL bovine IgG in PBS buffer and left to incubate at 4° C for 24 hours. After 24 hours, the slide was thoroughly rinsed with ultrapure deionized

was and then scanned with fluorescence spectroscopy at an excitation wavelength of 280 nm. The excitation wavelength chosen is the primary excitation wavelength used for monitoring the presence of tryptophan in biomolecules. **Figure 4.2** shows the emission spectrum of the isothiocyanate functionalized quartz slide, conjugated with bovine IgG.

Following antibody conjugation, the antibody must be labeled with an optical probe to improve the fluorescence sensitivity for running the assay. The probe employed first was fluorescein isothiocyanate, due to its well-established use as a probe in the labeling of biomolecules. However, it was observed that the binding of FITC did not occur as intended. Following probe binding, the slide was removed from the FITC solution and thoroughly rinsed with ultrapure deionized water. The slide was then transferred to a quartz cuvette containing fresh PBS. Prior to submerging the slide in the PBS cuvette, a background scan was taken to ensure no signal was attributed to the buffer solution and that the cuvette was properly cleaned. After obtaining a clean background displaying zero emission in the range of the probe, an initial measurement of the emission intensity of the FITC bound to the quartz slide was obtained. The slide was then left in the cuvette, submerged in the PBS and stored at 4° C for 30 minutes. As **Figure 4.3** portrays, a scan of the PBS the slide was stored in with the slide removed showed a significant signal for FITC. This indicated a source of error, as FITC releasing into the buffer would hinder the use of this as an immunoassay.

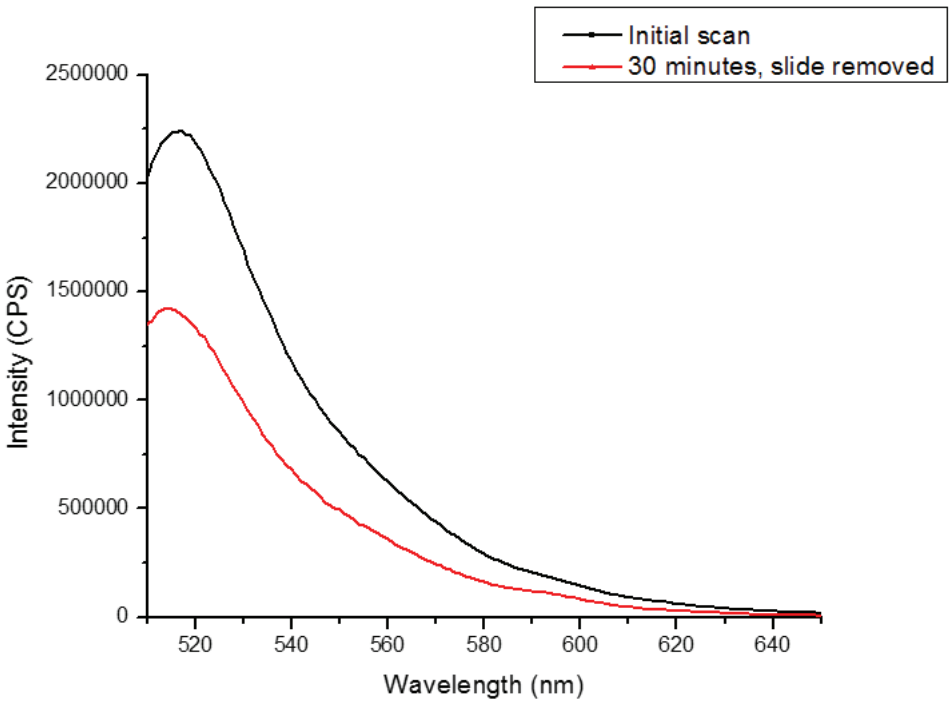

Figure 4.3 Fluorescence emission spectrum of isothiocyanate functionalized quartz slide with bovine IgG labeled with FITC (ex. 494 nm). (Black) Initial scan after probe binding and (Red) scan of PBS the slide was stored in 30 minutes after the initial scan.

4.3.2 Conjugation optimization

To resolve issues that arose in attempting isothiocyanate functionalization, a range of reaction conditions were manipulated to correct the sources of error. The first condition manipulated was the incubation time. Originally, the quartz slide was incubated in FITC for 24 h at 4° C. The reaction must be kept cold to make sure the antibody retains its secondary structure, however, cooling the solution slows the kinetics of the FITC binding. To determine if this was causing insufficient binding, four new incubation systems were employed: 1) 90 minutes stirring at room temperature, 2) two days at 4° C, 3) one week at 4° C, and 4) 90 minutes stirring at room temperature, followed by two days at 4° C. While none of the incubation changes lead to a complete resolution in the problem, there was insight provided for improving the current

methodology. First, increasing the time spent reacting at 4° C by one day led to an increase in the initial signal of ~1,000,000 CPS, indicating there is a larger density of FITC bound to the quartz slide over time. However, letting the quartz slide incubate at 4° C for one week only led to an increase in 1,220,000 CPS, when compared to one day. Furthermore, adding room temperature incubation also impacted the FITC conjugation. The slide incubated at 90 minutes at room temperature experienced a significantly low initial signal, however, there was a marked improvement in the amount FITC that remained on the slide and did not dissolve into the PBS. This indicated that incubation at room temperature helped form stable covalent bonds with FITC, although, the weak fluorescence emission intensity signifies that the amount of FITC conjugating to the slide was low. This led to the use of 90 minutes at room temperature, followed by two days at 4° C, which generated the most promising results of all the incubation conditions. However, FITC was still found in much too high amounts in the PBS to move forward.

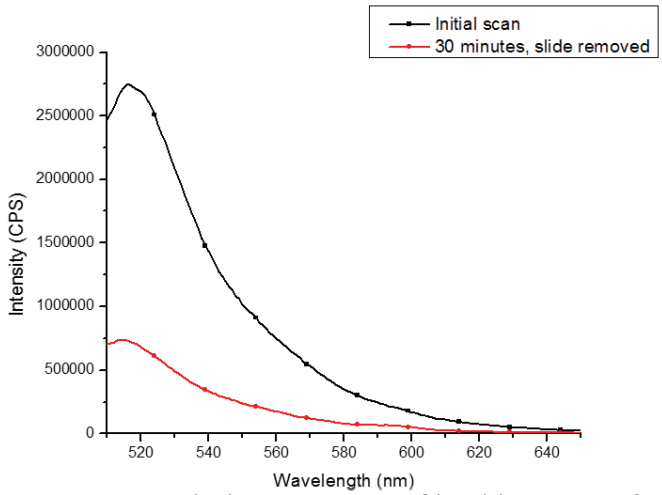

Figure 4.4 Fluorescence emission spectrum of isothiocyanate functionalized quartz slide with goat FITC-labeled IgG (ex. 494 nm). (Black) Initial scan after antibody binding and (Red) scan of PBS the slide was stored in 30 minutes after the initial scan.

Next, a control antibody was used that was prelabeled with FITC to determine if the problem observed was from the FITC binding procedure. A goat monoclonal IgG that was conjugated with FITC was purchased (Abgent) and used in place of bovine IgG for antibody binding, to investigate if FITC was found to release into the PBS overtime. As shown in **Figure 4.4**, there is still a significant amount of FITC observed in the PBS after 30 minutes, indicating the problem was likely occurring earlier in the binding procedure. Indeed, a scan of this same PBS solution at 280 nm displays an emission, indicating that the antibody was insufficiently binding to the quartz slide, rather than the probe (**Figure 4.5**).

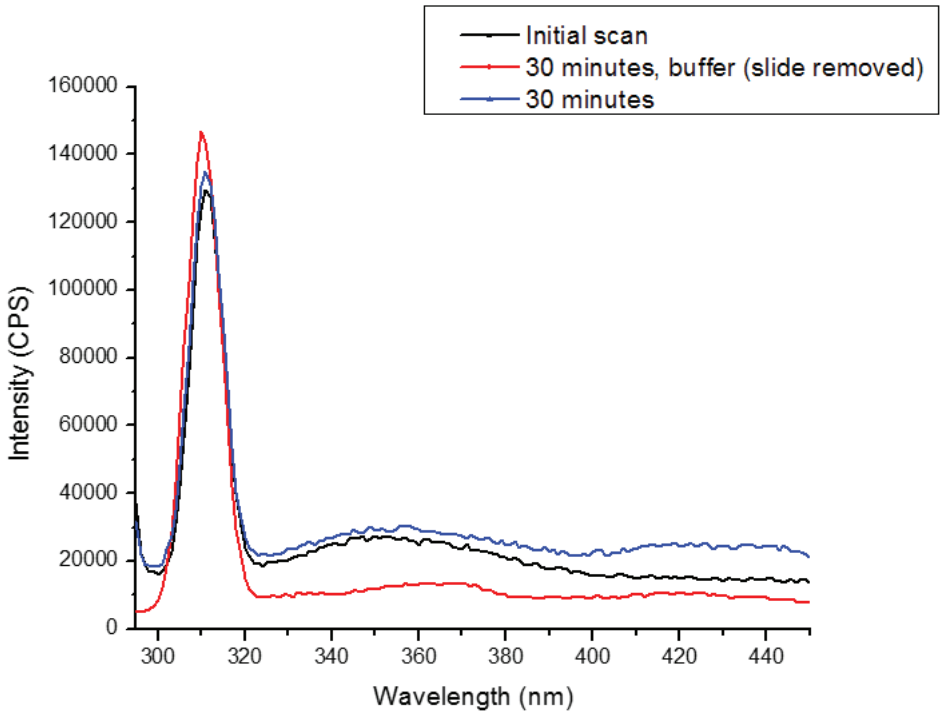

Figure 4.5 Fluorescence emission spectrum of isothiocyanate functionalized quartz slide with goat FITC-labeled IgG (ex. 280 nm).

To improve the antibody binding, the incubation conditions found to improve FITC binding were implemented. A noticeable improvement was made from changing

the incubation conditions to 90 minutes stirring at room temperature, followed by two days at 4° C, however, the improvement was not enough to move forward with the next step of the assay, and instead, new binding approaches had to be explored.

4.3.3 Glutaraldehyde functionalization

Improving upon the work done above, an alternative functionalization approach was attempted to resolve the incomplete binding of the antibody (**Scheme 4.2**). To achieve this goal, a cleaned and activated quartz slide was silanized with (3-aminopropyl) trimethoxysilane, leaving a primary amine functional group, just as was done in the isothiocyanate approach. After the slide was silanized and dried, it was incubated in 25% (w/v) glutaraldehyde in ultrapure deionized water for four hours at room temperature.

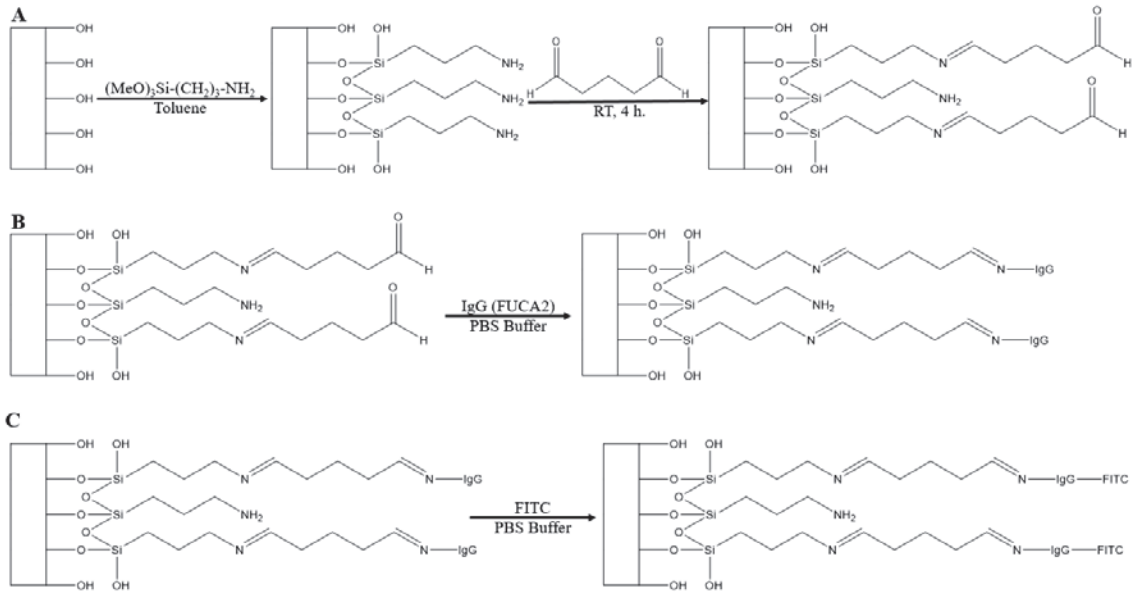

Scheme 4.2 Quartz surface modification: (A) Amino-modified quartz and reaction with glutaraldehyde; (B) mutant IgG (FUCA2) immobilization; (C) IgG labeling with FITC.

Once the slide was functionalized with glutaraldehyde, it was ready for antibody binding. Amines from lysine on the antibody should experience favorable reactivity

towards the exposed aldehyde on the quartz surface. However, upon taking an initial scan after the antibody conjugation procedure, no emission occurred. This indicated that the glutaraldehyde procedure was ineffective at achieving a stable immobilization of the antibody.

4.3.4 Thiol functionalization

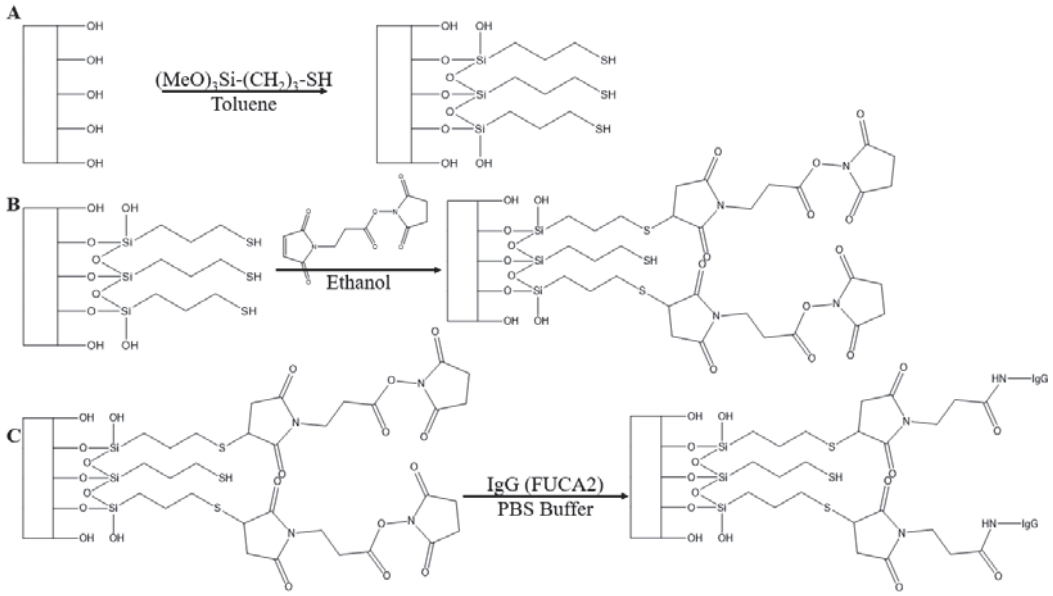

Scheme 4.3 Quartz surface modification: (A Thiol-modified quartz; (B) reaction with maleimide linker (C) mutant IgG (FUCA2) immobilization.

While the previous functionalization approach used a (3-aminopropyl) trimethoxysilane, this approach implemented the silane derivative (3-mercaptopropyl) trimethoxysilane. Silanization with (3-mercaptopropyl) trimethoxysilane results in the quartz slide being left with thiol functional groups, rather than the primary amine from the previous methods. Gaining thiol functionality was desirable, because thiols experience very strong reactivity towards maleimides, allowing the bifunctional linker N-succinimidyl 3-maleimidopropionate to be utilized. The thiol binds to the maleimide side of the bifunctional linker, leaving the quartz surface exposed with a succinimide group

(**Scheme 4.3**). Succinimide is a very common moiety in use of conjugation with biomolecules, because it is a good leaving group and is rapidly displaced in the presence of primary amines, creating a covalent amide bond.

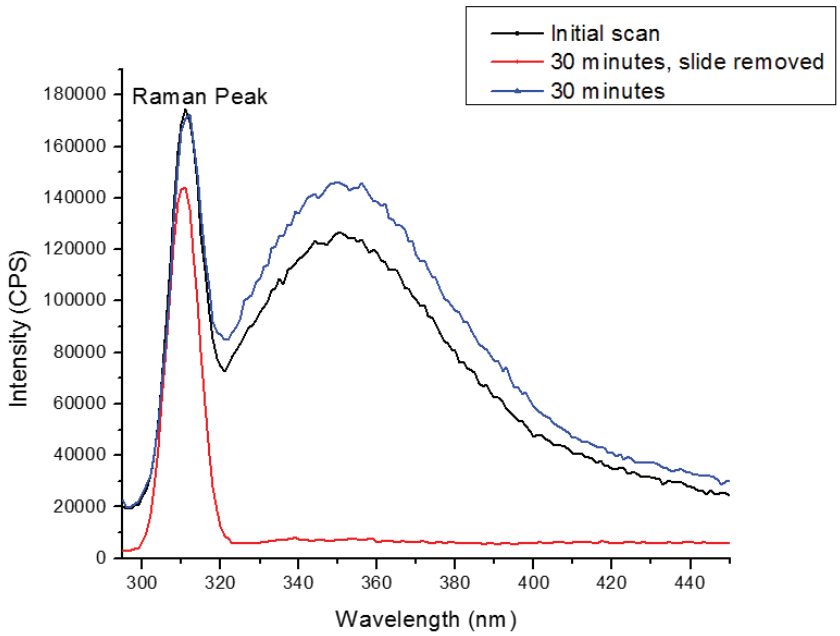

Figure 4.6 Fluorescence emission spectrum of thiol functionalized quartz slide with bovine IgG (ex. 280 nm). (Black) Initial scan after antibody binding, (Red) scan of PBS the slide was stored in 30 minutes after the initial scan and (Blue) scan of slide after 30 minutes placed back into the PBS.

Figure 4.6 displays the emission spectra of the quartz slide assay prepared with thiol functionalization. There was a significant improvement shown in the extent of antibody binding, as a minimal amount was found in the PBS solution after 30 minutes. To determine if the antibody binding was sufficient for developing an assay, rhodamine was conjugated to the antibody. However, after 30 minutes in PBS, a significant amount of the probe was found released from the quartz slide (**Figure 4.7**).

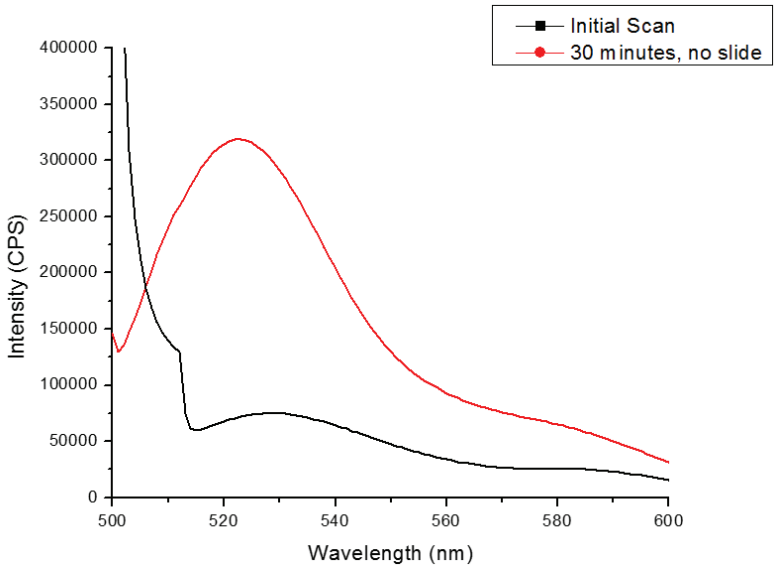

Figure 4.7 Fluorescence emission spectrum of thiol functionalized quartz slide with bovine IgG labeled with Rhodamine 6G (ex. 495 nm). (Black) Initial scan after antibody binding and (Red) scan of PBS the slide was stored in 30 minutes after the initial scan.

4.3.5 Carboxy-PEG12-thiol functionalization

While improvements were made in ***4.3.4***, the antibody binding was still not sufficient for developing an immunoassay. It was likely that while some antibodies are covalently bound to the slide, trace amounts of the antibody were electrostatically binding to the exposed quartz surface. If the packing of the linker is insufficient, it is possible that the antibody can interact with the charged quartz surface, resulting in the observed release into the buffer. One proposed method for improving the packing on the quartz surface was to use (polyethylene)glycol (PEG) spacers. PEG spacers provide controllable length and strong packing interactions. Increasing the length of PEG spacers causes steric hindrance to the quartz surface and improved packing due to intermolecular interactions between the long PEG chains.

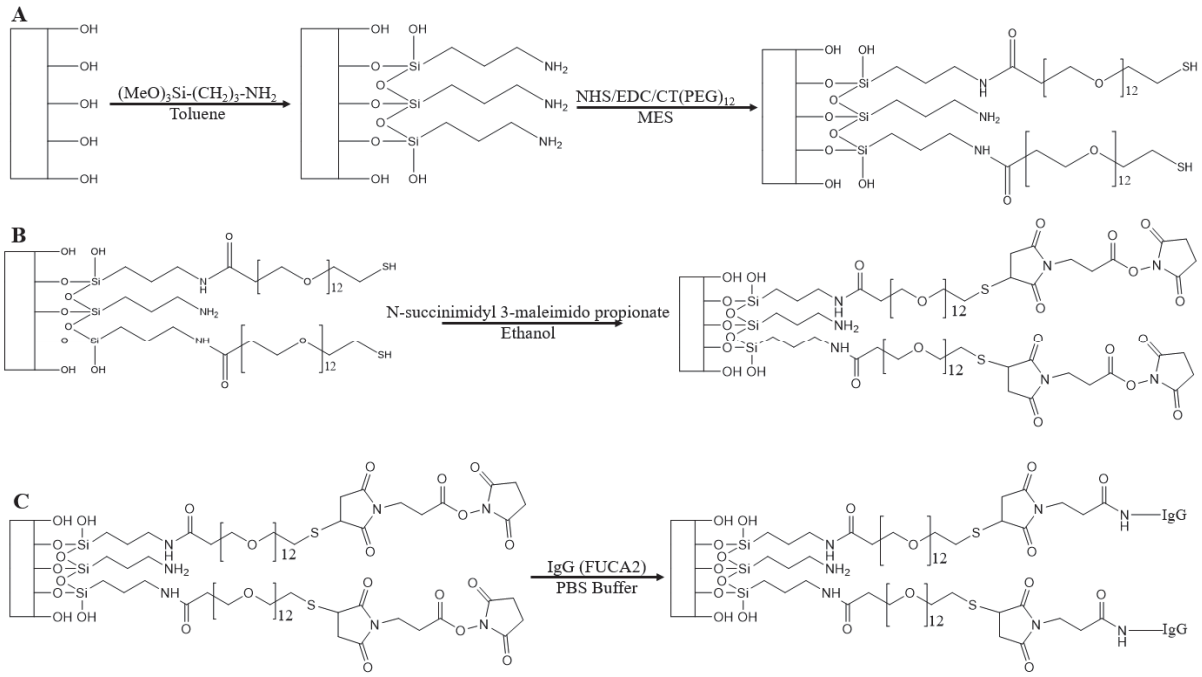

Scheme 4.4 Quartz surface modification: (A) Amino-modified quartz and reaction with NHS activated $CT(PEG)_{12}$; (B) Attachment of bifunctional linker, N-succinimidyl 3-maleimido propionate; (C) mutant IgG (FUCA2) immobilization.

Scheme 4.4 presents a modified method of creating a terminal thiol on the quartz surface, utilizing a branched PEG spacer. The slide was first silanized with (3-aminopropyl) trimethoxysilane. The PEG spacer chosen first was carboxy-PEG12-thiol [$CT(PEG)_{12}$]. The PEG spacer was activated with EDC, then treated with NHS to convert the carboxylic acid into a more reactive succinimide ester. The quartz slide was then deposited into a solution with the PEG linker, and the primary amines left on the quartz slide created an amide bond, leading to covalent attachment of the PEG spacer to the quartz slide. From this point, the slide possesses terminal thiols and the procedure for IgG conjugation is the same as ***4.3.4***. While only trace amounts of IgG were found to have dissolved into the background solution, there was a large hindrance in the extent of

antibody that was covalently bound. The low amount attached proved insufficient to move forward with probe labeling (**Figure 4.8**).

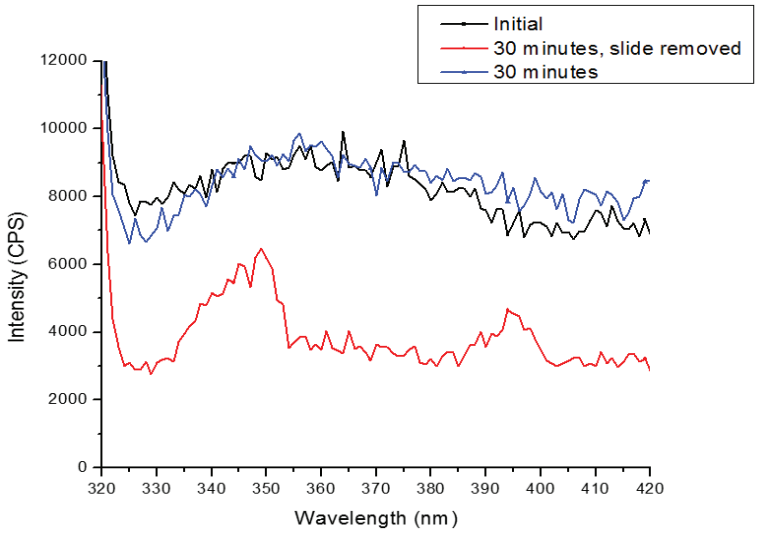

Figure 4.8 Fluorescence emission spectra of CT(PEG)$_{12}$ functionalized quartz slide with bovine IgG (ex. 280 nm). (Black) Initial scan after antibody binding, (Red) scan of PBS the slide was stored in 30 minutes after the initial scan and (Blue) scan of slide after 30 minutes placed back into the PBS.

4.3.6 Succinimide-PEG12-maleimide functionalization

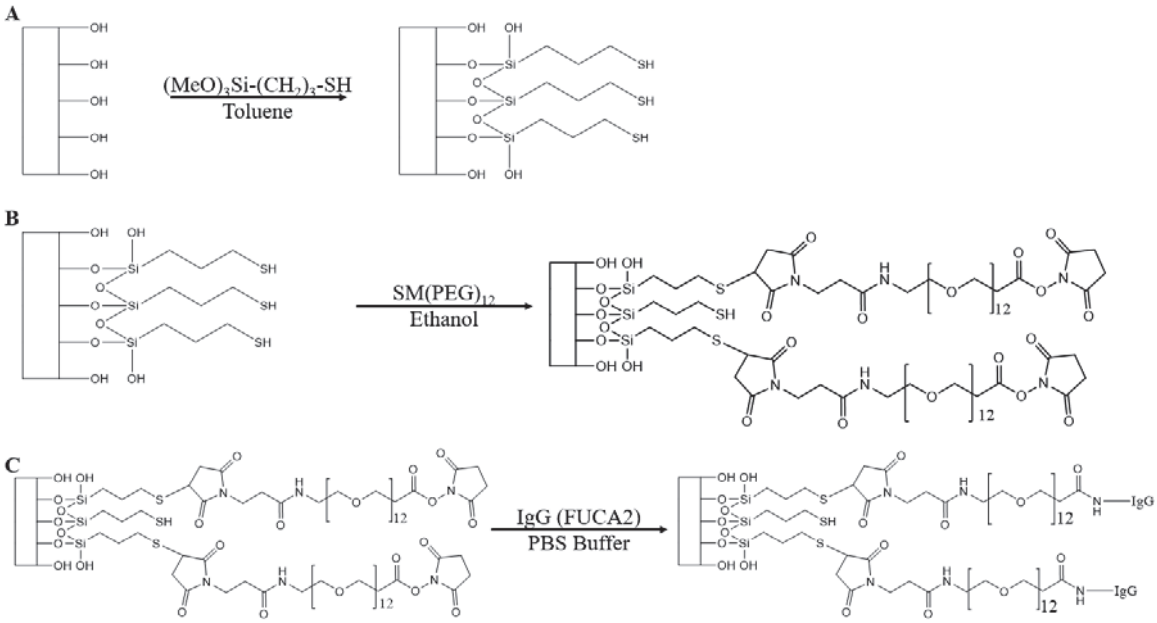

Scheme 4.5 Quartz surface modification: (A) Thiol-modified quartz slide; (B) Attachment of SM(PEG)$_{12}$ linker; (C) mutant IgG (FUCA2) immobilization

An alternative PEG spacer, based upon results from ***4.2.4***, was also attempted (**Scheme 4.5**). Rather than adding an additional spacer, as was the case with CT(PEG)$_{12}$, this approach uses a modified version of the bifunctional linker N-succinimidyl 3-maleimidopropionate. The linker implemented was succinimidyl-PEG12-maleimide [SM(PEG)$_{12}$], which contains the same reactive moieties as N-succinimidyl 3-maleimidopropionate, but with a longer spacer of 12 (polyethylene)glycol rather than a short propionate. For this approach, the slide was treated with (3-mercaptopropyl) trimethoxysilane, creating a quartz surface with exposed thiols for further conjugation. The quartz slide was then stirred in SM(PEG)$_{12}$ dissolved in PBS for two days at room temperature. After two days, the slide was rinsed thoroughly and incubated with bovine IgG and the binding was monitored with fluorescence spectroscopy. Through the use of SM(PEG)$_{12}$, the lowest amount of antibody was found to have released from the slide, as the buffer scan after 30 minutes of exposure was about as flat as the background scan (**Figure 4.9**). However, this approach also produced the lowest signal of antibody bound to the quartz slide, which possibly could hinder the assays efficacy moving forward.

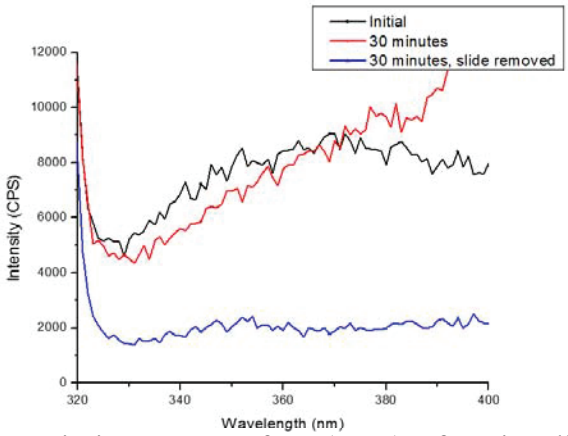

Figure 4.9 Fluorescence emission spectra of SM(PEG)$_{12}$ functionalized quartz slide with bovine IgG (ex. 280 nm). (Black) Initial scan after antibody binding, (Red) scan of PBS the slide was stored in 30 minutes after the initial scan and (Blue) scan of slide after 30 minutes placed back into the PBS.

To explore if the IgG conjugation was sufficient to move forward with the assay, the probe labeling step was attempted with a rhodamine probe. Some of the probe was found in the buffer, however, a majority of the probe remained conjugated to the quartz slide (**Figure 4.10**). The amount of probe found in the buffer was decreased even further by changing the washing procedure of the quartz slide following probe conjugations. Rather than thoroughly rinsing the slide, the quartz slide was instead placed into a fresh vial with PBS buffer and sonicated for 15 minutes. After 15 minutes, the slide was removed, rinsed with ultrapure deionized water, and then this cleaning process was repeated two additional times for a total of three times per wash cycle. At the completion of a wash cycle, an initial measurement of the slide is taken as was done previously, followed by a scan of the solution the slide is kept in 30 minutes later. If a signal appears upon scanning the buffer in the probe's emission range, then the quartz slide is then ran through another wash cycle. It was found that three wash cycles was sufficient for producing background scans with no probe found released into the PBS.

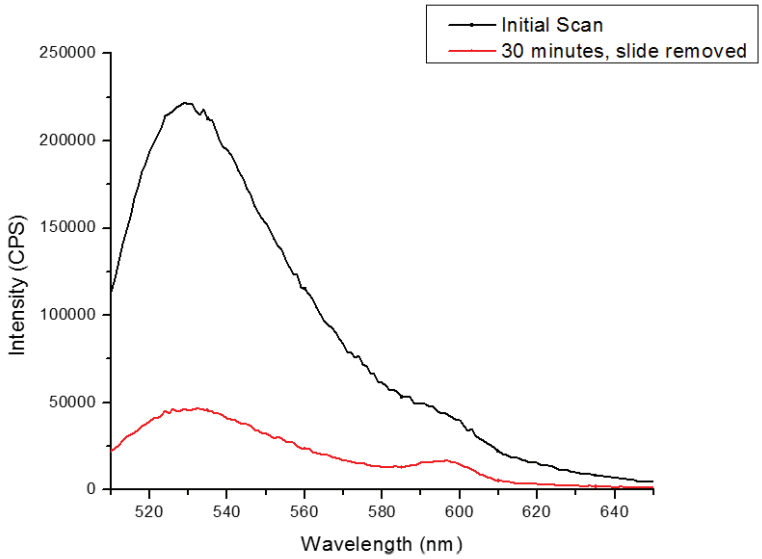

Figure 4.10 Fluorescence emission spectra of SM(PEG)$_{12}$ functionalized quartz slide with rhodamine labeled bovine IgG (ex. 495 nm). (Black) Initial scan after antibody binding and (Red) scan of PBS the slide was stored in 30 minutes after the initial scan.

4.4 Quartz slide assay detection of alpha-L-fucosidase in phosphate buffer saline

Using the results from **4.3**, the ideal conditions were found to be a quartz slide utilizing a thiol terminated trimethoxysilane derivative, followed by an $SM(PEG)_{12}$ bifunctional spacer, then subsequent conjugation with the fucosidase specific antibody and rhodamine probe. These conditions were thus used to produce a calibration curve for quantifying the concentration of AFU in PBS. To produce the calibration curve, the quartz slide was incubated at 37° C in varying known amounts of alpha-L-fucosidase after the probe and antibody had already been confirmed to be thoroughly bound to the slide. **Figure 4.11** shows the emission spectra of the rhodamine probe after incubation with increasing concentrations of AFU. By incubating the slide in increasing increments of AFU, more AFU binds to the FUCA2 antibody, creating a complex between the antibody and AFU. This complex leads to an observed quenching in the emission of the rhodamine probe, which was found to be linearly proportional to the concentration of AFU present. This linear relationship allows for the extrapolation of a Stern-Vølmer plot of the observed quenching, which can serve as a standard for quantifying unknown values of AFU in solution.

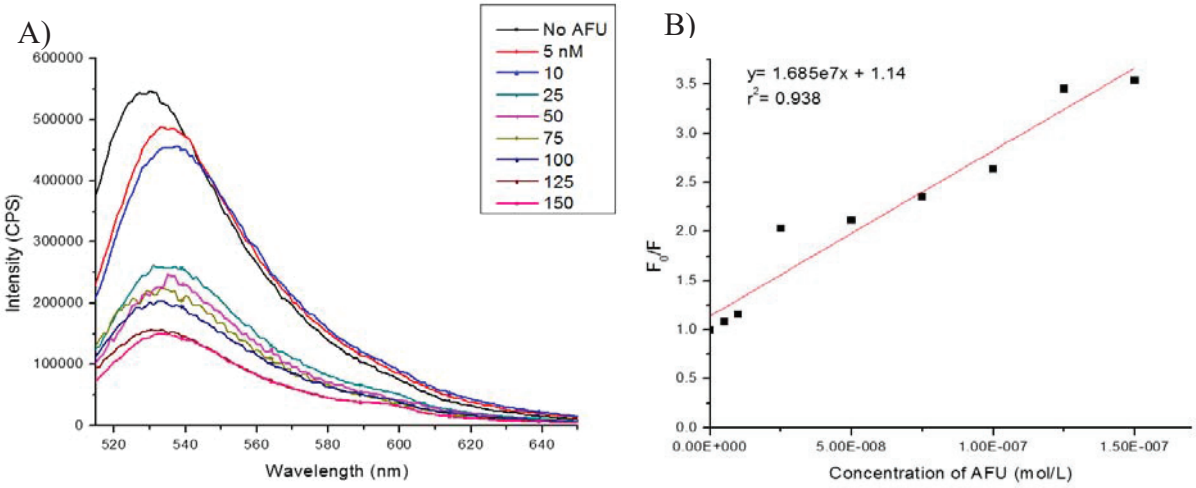

Figure 4.11 (A) Fluorescence emission spectrum of quartz slide assay (ex. 495 nm) at increasing concentrations of **AFU** and (B) Stern-Vølmer linear extrapolation.

4.5 Summary

In conclusion, an immunoassay bound to a solid quartz slide support was produced. To attach immunoglobulin to the quartz surface, a variety of different binding chemistry was examined. After optimizing the conjugation procedure, the quartz slide assay was used to detect BSA by monitoring the change in emission of a rhodamine probe. It was found that the decrease in emission of the rhodamine probe was linearly proportional to the concentration of BSA present. Upon confirming the assay could detect BSA, it was then altered to detect AFU. A calibration curve was then produced for AFU detection based upon the change in fluorescence emission in the presence of increasing concentrations of AFU.

Chapter 5

Nanoparticle Immunoassay for Detection of Alpha-L-Fucosidase

5.1 Background

Many approaches have been utilized in developing an efficient biosensor. Developing an effective assay relies upon a balance between the sensitivity of detection, ease of approach, the speed in which detection can be made, and the cost. Radioimmunoassys represent one of the most sensitive techniques, however, they require highly trained individuals and the use of hazardous isotopes. ELISA has become a universal standard for assay production, due to the great ease in the meaurements, the lack of specific equipment or highly trained indiduals, and the particularly low cost. Nevertheless, they are not a perfect assay, as the ease in measurement leads to a significant blow to the sensitivity.

The development of nanotechnology has shown great promise in furthering the field of analytics. Carbon dots are an interesting nanoparticle because they express similar optical properties to quantum dots but are much easier to prepare and use nontoxic carbon materials rather than toxic heavy metals like cadmium.[161] The primary materials being developed include, but are not limited to, fullerene,[162,163] carbon nanotubes,[164] nanodiamonds[165] and carbon dots.[166] The latter, carbon dots, have been receiving an increasing amount of attention due to the favorable properties these particles possess. Carbon dots offer notable advantages over many similar nanoparticles, such as water solubility,[167,168] tunable emissions,[169] ease in synthetic approaches, and low toxicity.[170]

The facile and extensive basis in which these nanoparticles are formed has been well investigated.[161] In 2006, Sun et al.[171] reported the first synthesis and characterization of carbon dots through acid oxidation of laser ablated graphite powder and cement, followed by passivation with polyethylene glycol. Synthesis techniques now consist of hydrothermal/solvothermal approaches,[172-174] microwave synthesis,[175-177] and electrochemical oxidation. Another appealing quality of carbon dot synthesis is the wide spectrum of starting materials that can be implemented, including inexpensive organic compounds/solvents,[178] food products[179-181] and waste.[182] Carbon dots can be made from virtually any source of carbon, as synthetic approaches using everything from waste to food products have been shown.[183] Coupled with the ease in producing these nanoparticles, carbon dots are saturated in surface carbonyls that have been previously shown to be utilized in coupling to various biological molecules. The most attractive quality of carbon dots, however, is their optical properties. Carbon dots are highly luminescent and experience excitation-dependent emissions. This allows the emission of a carbon dot to be tuned to a desired range through selecting a corresponding excitation. Tunable emissions are a very desirable trait in sensing, as the emission can be catered to best suit the detection method.

Gold nanoparticles are some of the most investigated nanoparticles, and they possess very favorable properties, especially for optics. Gold nanoparticles express a large absorption band around 525 nm, caused by the surface plasmon. By coupling gold nanoparticles and carbon dots in the same assay, the emission of the carbon dots can be tuned, such that, there will be an overlap in the emission of the carbon dots with the surface plasmon band of the gold nanoparticles. Once this is achieved, an assay can be

developed in which gold nanoparticles will come into close proximity with carbon dots in the presence of the biomarker, leading to a quenching of the carbon dot lumisence through energy transfer to the surface plasmon band of the gold nanoparticles. This approach can be used to produce a calibration plot that can be utilized in quantifying unknown concentrations of the respective biomarker from serum samples.

The gold nanoparticle immunoassay will employ polyclonal antibody-capped gold nanoparticles for capture of a desired antigen, with the use of carbon dots conjugated to a monoclonal detection antibdoy. Immobilization of antibodies will rely on the surface modification of proteins, which is most commonly realized through binding to primary amine residues, due to their ability to react with various functional groups in water. At first, gold nanoparticles must be produced. Gold nanoparticles are an ideal support for immobilization due to their unique optical properties (high extinction coefficient),[184] ease of preparation, and ability to be functionalized with antibodies. This approach has flexibility in how the gold nanoparticles are functionalized. The loading of proteins, including antibodies, onto gold surfaces has extensively been studied, and the two prominent strategies involve either electrostatic or covalent coupling. Electrostatic coupling is facile using citrate-capped gold nanoparticle. Upon antigen binding to the polyclonal-capped gold nanoparticle, a sandwich assay can be produced by addition of a monoclonal detection antibody. By using a carbon dot probe, the emission wavelength can be catered to overlap with the surface plasmon of the gold nanoparticle. In this manner, antigen binding will cause a decrease in photoluminescence from the carbon dot due to energy transfer to the surface plasmon.

5.2 Experimental

5.2.1 Materials and methods

Chloroauric acid and bovine IgG were obtained from MP Biomedicals (Santa Ana, CA, USA). Citric acid (anhydrous, ≥99.5%), sodium citrate (95%) and ethylenediamine (99%) were purchased from Sigma Aldrich (St. Louis, MO) and were used without further purification. PD 10 columns were received from GE Healthcare Bio-Sciences (Pittsburg, PA, USA). Dialysis was run through a Cellulose Ester membrane with molecular weight cut-off 500-1000 Daltons purchased from Spectrum Laboratories Inc. (Rancho Dominguez, CA). Purified water was obtained from an Elga PURELAB Ultra water purifier (Woodridge, IL) with a resistivity of 18MΩ·cm, surface tension of 72.6 mN m^{-1}, and pH 5.6 at 20.0 ± 0.5°C.

Ultraviolet-visible spectroscopy measurements were obtained on an Agilent Cary 100 spectrophotometer (Santa Clara, CA, USA). Fluorescence measurements were carried out on a Horiba Jobin Yvon Fluorolog-3 (Kyoto, Japan) with slit widths set to 5 nm for both excitation and emission.

5.2.2 Synthesis of citrate-capped gold nanoparticles

50 mL of a 0.01% (w/v) solution of chloroauric acid dissolved in DI H_2O was brought to a boil. Once boiling, 2 mL of 1% sodium citrate (w/v) was added under constant, vigorous stirring. The mixture was left boiling for 10 minutes, then moved to cool in the dark. The final product collected was diluted up to 50 mL and stored in the dark at 4°C until further use.

5.2.3 Synthesis of immunoglobulin-capped gold nanoparticles

Sodium carbonate was added to the citrate-capped gold nanoparticles to adjust the pH to 9. 1 mL of pH 9 citrate-capped nanoparticles was then incubated with 1 mL of 0.15 mg/mL polyclonal anti-BSA IgG or anti-FUCA2 in PBS for 90 minutes at room temperature. The product was then immediately cooled down to 4°C. Once cooled, the mixture was centrifuged at 10,000 RPM for 30 minutes at a temperature of 4° C. The pellet of IgG-capped gold nanoparticles obtained after centrifugation is then re-suspended in PBS and stored in the dark at 4°C.

5.2.4 Synthesis of carbon dot probe

To synthesize a carbon dot probe, citric acid and ethylenediamine were condensed into polymeric carbon dots possessing excitation-dependent emission and particle sizes around ~4 nm. The synthesis began by heating 20 mL of ethylenediamine to a boil (>120°C). Once the ethylenediamine began to boil, approximately 4 grams of citric acid was added to give a molar ratio of 14:1 ethylenediamine to citric acid. The mixture was then refluxed for ~10min. After this time period, the residual ethylenediamine was then evaporated off using a rotovap. Upon evaporation, a viscous yellow crude product was left behind. To remove excess starting material or other impurities, the crude product was dissolved in a minimal amount of deionized water and then put under dialysis (molecular weight cut-off 500-1000) with 2L of water for 2 days, changing the water every 4-10 hours.

5.2.5 Antibody functionalization with fluorescein isothiocyanate probe

1 mL of a 2mg/mL solution of the desired antibody (anti-BSA or FUCA2) was incubated with 1.5 equivalents of FITC dissolved in DMSO. The mixture was stirred at

room temperature for one hour, then separated using a PD-10 column (Sephadex G-25) with Tris buffer (pH 8.2) to elute the conjugated product. The final concentration is determined by absorption spectroscopy.

5.2.6 Antibody functionalization with carbon dot probe

A 0.01 mg/mL solution of monoclonal anti-BSA or anti-FUCA2 is dissolved in PBS (pH 7.4). A separate solution is then prepared, with 1 g of carbon dots dissolved in 2 mL of MES buffer with 1-Ethyl-3-(3-dimethylaminopropyl) carbodiimide (EDC). Next, the EDC activated carbon dots are moved to a vial containing 1.5 equivalents of NHS dissolved in PBS buffer. The vial is sealed and argon is bubbled in and the slide is left to stir at room temperature for two hours in the dark. After two hours, the 0.01 mg/mL solution of monoclonal antibody is added. The contents are left stirring at room temperature for one hour, then left to incubate at room temperature for two days.

To separate the labeled antibody, a PD 10 desalting column with Sephadex G25 was used. The column is equilibrated with Tris buffer, then the antibody/carbon dot solution is added to the column. Tris buffer is added to elute the carbon dot labeled antibodies, and the conjugation is confirmed through spectroscopy.

5.2.7 Gold nanoparticle assay for detection of alpha-L-fucosidase

200 µL of the IgG-capped gold nanoparticles were incubated with 100 µL of 0.005 M NaCl in 500 µL of PBS, containing known amounts of alpha-L-fucosidase. The nanoparticles were incubated with AFU at 37° C for 30 minutes. 200 µL of the monoclonal carbon dot labeled detection antibody was then added and the incubation was continued another 30 minutes. The mixture was then placed under centrifugation for 10 minutes at 10,000 RPM. The supernatant was removed and the pellet was re-suspended

in fresh PBS. The solution was then placed under centrifugation two additional times for 10 minutes at 10,000 RPM, removing the supernatant and suspending the pellet in fresh PBS each time. The fluorescence of the carbon dot probe was measured and a plot of F_0/F vs. the concentration of AFU was obtained.

5.3 Gold nanoparticle immunoassay optimization with bovine IgG

5.3.1 Fluorescein isothiocyanate probe

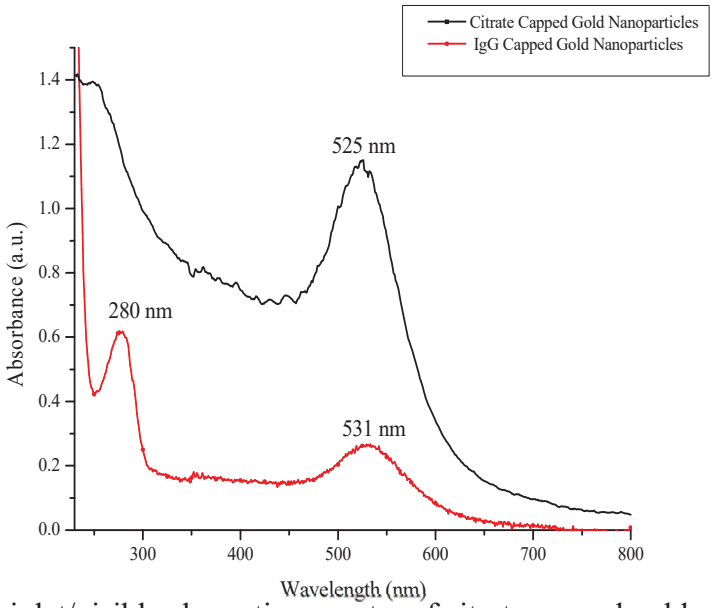

Figure 5.1 Ultraviolet/visible absorption spectra of citrate capped gold nanoparticles (black) and IgG capped gold nanoparticles (red).

To develop an immunoassay based upon a gold nanoparticle support, detetcion of BSA using a fluorescein isothiocyante probe was first attempted for proof of concept. Preparation of gold nanoparticles began with the boiling of tetrachloroauric acid with sodium citrate to yield citrate-capped gold nanoparticles. The citrate-capped gold nanoparticles were then incubated in a solution containing polyclonal anti-BSA at a high pH. Alkaline pH ensures that the primary amines on the polyclonal antibody are not fully protonated, allowing for electrostatic interactions to occur with the gold nanoparticle

surface. Over time, the citrate capping is replaced with antibody capping, which was confirmed through observing the absorption spectrum of the two prepared nanoparticles (**Figure 5.1**). Gold nanoparticles prepared with citrate capping display only one peak which appears at 525 nm from the surface plasmon of the gold nanoparticles. After treatment with the polyclonal IgG, an additional peak is observed at 280 nm, which indicates the presence of the antibody. Additionally, the surface plasmon was found to experience a red shift and weaken in signal upon antibody binding.

In preparing an antibody-capped gold nanoparticle, a polyclonal antibody was chosen for use as the capture antibody. Polyclonal antibodies are cheaper to produce than monoclonal antibodies and possess affinity to multiple epitopes on antigens. While affinity to multiple epitopes can lead to a decrease in specifity, it can greatly enhance the amount of antigen that is captured in solution. Detection of antigen binding can then be enhanced for sensitivity by using a probe labeled monoclonal antibody for the same antigen. The monoclonal antibodies are highly specific and express affinity to a single epitope, allowing the desired antigen to be descriminated from nonspecific binding that may occur with other antigens on the capture antibody.

To produce a detection antibody, monoclonal anti-BSA was labeled with FITC. FITC was chosen as a probe due to its favorable binding chemistry to antibodies and its emission at ~520 nm. The emission of the chosen probe is important for the purposes of detection in the assay. The assay is focused upon the strong absorbance of the surface plasmon of the gold nanoparticles. When the detection antibody binds to the antigen, it is brought into closer proximity with the gold nanoparticle and the overlap with the surface

plasmon and the emission in the probe results in a decrease in fluorescence emission of the probe from the energy transfer.

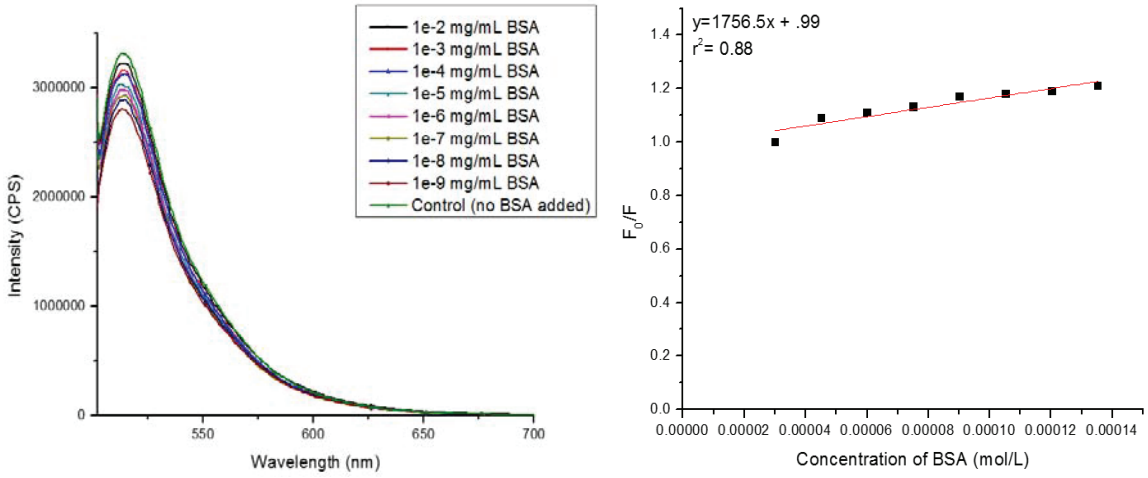

Figure 5.2 (A) Fluorescence emission spectrum of polyclonal anti-BSA capped-gold nanoparticles with FITC labeled monoclonal detection antibody (ex. 494 nm) with increasing incubation concentrations of BSA and (B) Stern-Vølmer linear

To determine if the energy transfer from FITC-labeled detection antibodies could be sufficient in quantifying the concentration of antigen in solution, the polyclonal anti-BSA-capped gold nanoparticles were incubated in increasing concentrations of BSA. After incubation with BSA for 30 minutes at 37° C, the monoclonal FITC-labeled anti-BSA was added and the incubation was continued for an additional 30 minutes at 37° C. **Figure 5.2A** shows the emission spectra of FITC in varying concentrations of BSA, as well as a control in which no BSA was added. The value obtained with no BSA displayed the highest emission intensity as expected, and this value was used as the initial fluorescence to extrapolate a Stern-Vølmer plot. **Figure 5.2B** displays the linear extrapolation at varying concentrations of BSA. The y-intercept of the plot goes approximately through 1 which is expected as with no antigen present F_0/F would be

equal to 1. However, the degree of linearity expressed from the r^2 value is only 0.88, indicating the data points have a degree of improvement necessary.

5.3.2 Carbon dot probe

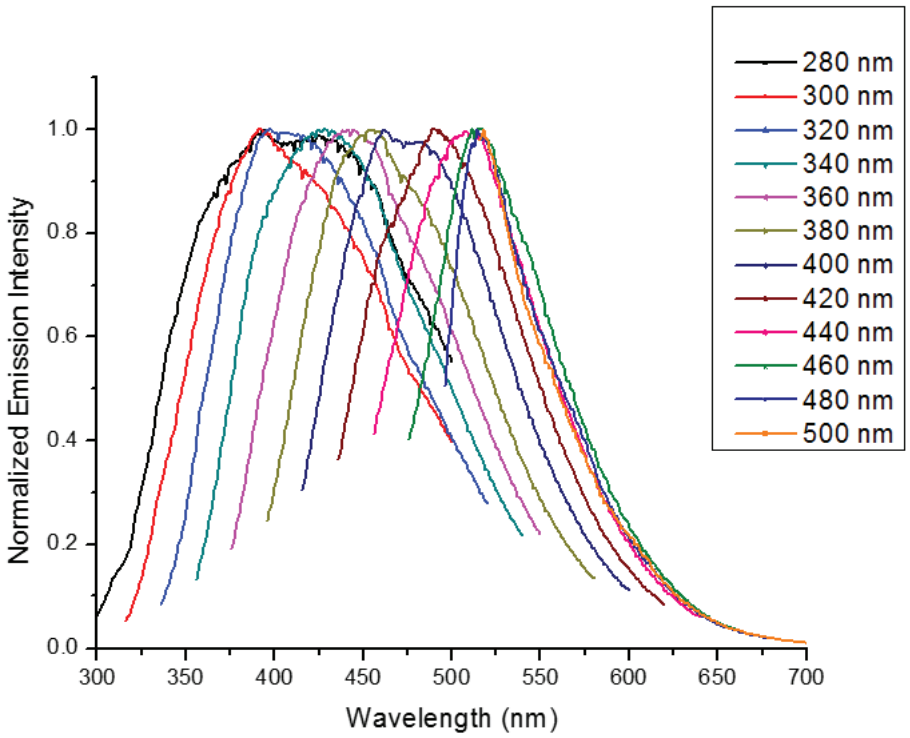

Figure 5.3 Normalized emission spectra of carbon dot at various excitation wavelengths.

Based on evidence from ***5.3.1***, it was clear that improvements needed to be made to the assay. One way found to enhance detection was to utilize an alternative probe. FITC is a standard probe in labeling biomolecules but new classes of probes have since been established. Carbon dots are a relatively new class of probes that have been found to have value in biosensing. One advantage that carbon dots possess over FITC is that the emission of carbon dots is dependent upon the excitation wavelength. This allows the emission of the carbon dot to be tuned to a desired range by selecting the appropriate excitation wavelength (**Figure 5.3**). This allows the carbon dot's emission to be tuned to experience high overlap with the absorbance band of the gold nanoparticle. With a

greater amount of overlap, the absorbance of the emission from the probe will be more efficient and in turn, the assay will be more efficient.

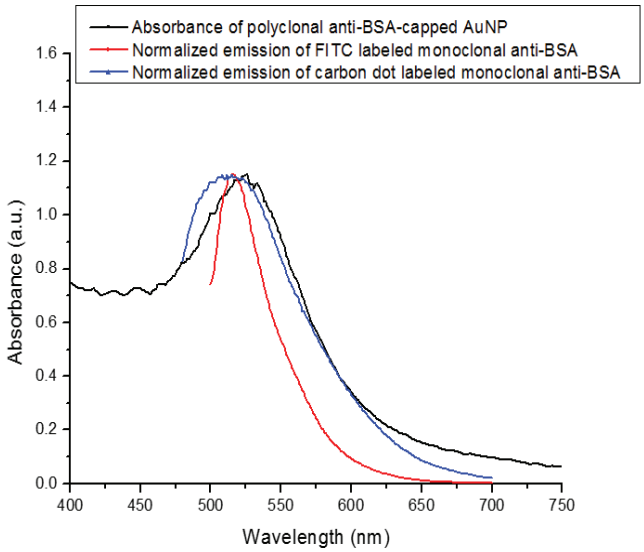

Figure 5.4 Overlap between absorbance of polyclonal-capped gold nanoparticles (black), emission of FITC probe conjugated to monoclonal anti-BSA (red), and emission of carbon dot labeled monoclonal anti-BSA (blue).

As shown in **Figure 5.4**, the broad emission of the carbon dot probe possesses a significant amount of overlap with the surface plasmon of the antibody-capped gold nanoparticle. To determine if this increase in overlap improved detection, a gold nanoparticle assay was set up similar to the FITC approach. To prepare a detection antibody with carbon dot labeling, a solution of carbon dots was activated with EDC and then treated with NHS to produce succinimide esters with surface carboxylic acids from the carbon dot. The carbon dots were then incubated with monoclonal anti-BSA, then separated by size exclusion to yield carbon dot labeled monoclonal anti-BSA. The assay was then run by incubating the polyclonal anti-BSA-capped gold nanoparticles with increasing amounts of BSA, followed by incubation with the carbon dot labeled detection antibody (**Figure 5.5**). A marked improvement was found as the Stern-Vølmer plot

shows the linear extrapolation goes almost perfectly through 1 on the y-intercept as it ideally should, and the r^2 was 0.95. From this plot, it was found that detection of BSA was capable on the nanomolar scale. However, the limit of detection was not determined at this point as this was not the desired antigen for detection and served only to test the methodology.

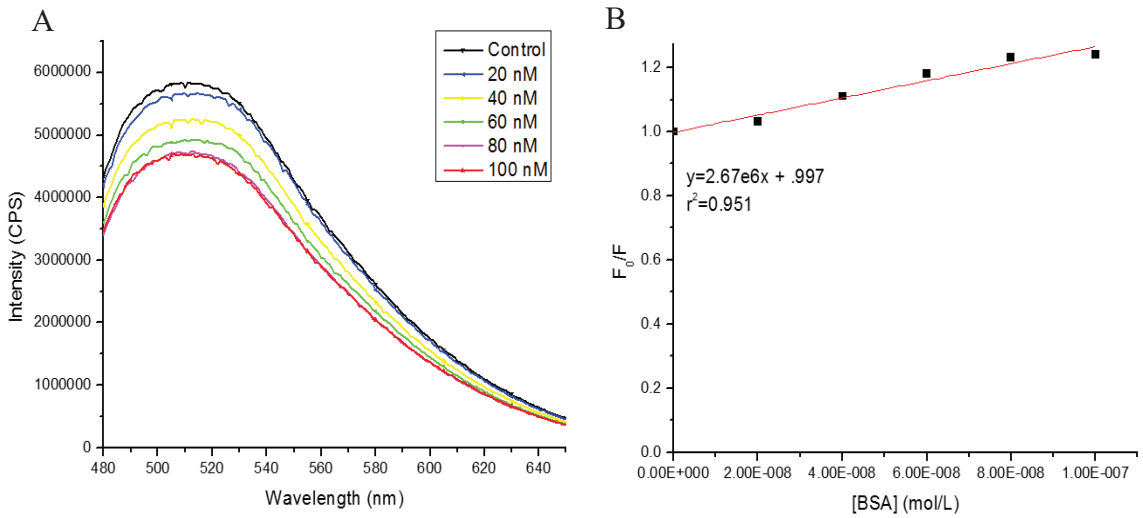

Figure 5.5 (A) Fluorescence emission spectrum of polyclonal anti-BSA capped-gold nanoparticles with carbon dot labeled monoclonal detection antibody (ex. 460 nm) with increasing incubation concentrations of BSA and (B) Stern-Vølmer linear extrapolation.

5.4 Gold nanoparticle immunoassay for detection of alpha-L-fucosidase in phosphate buffer saline

Upon confirming the methodology with BSA, the gold nanoparticle assay was modified for detection of AFU. The only necessary modifications for detecting AFU was to change the polyclonal capping antibody and the monoclonal detection antibody to IgG with specificity towards the FUCA2 epitope on AFU. The AuNP immunoassay for detecting AFU was run by incubating polyclonal anti-FUCA2-capped gold nanoparticles in increasing amounts AFU in PBS at 37° C for 30 minutes. After 30 minutes of

incubation, a carbon dot labeled monoclonal anti-FUCA2 detection antibody was added to the incubation. The incubation was carried out for an additional 30 minutes, then the mixture was centrifuged and the supernatant was removed. The gold nanoparticle pellet was re-suspended in PBS and the emission spectrum of the carbon dot probe was measured for each different concentration of AFU. **Figure 5.6** shows plot of F_0/F vs. the concentration of AFU. An ideal Stern-Vølmer plot would cross the y-intercept at 1 and be perfectly linear. The plot for AFU detection deviates slightly, as the y-intercept was found to be 0.996. The linearity displayed was 0.947, indicating there is indeed a strong correlation with the intensity of fluorescence of the carbon dot probe and the concentration of AFU present.

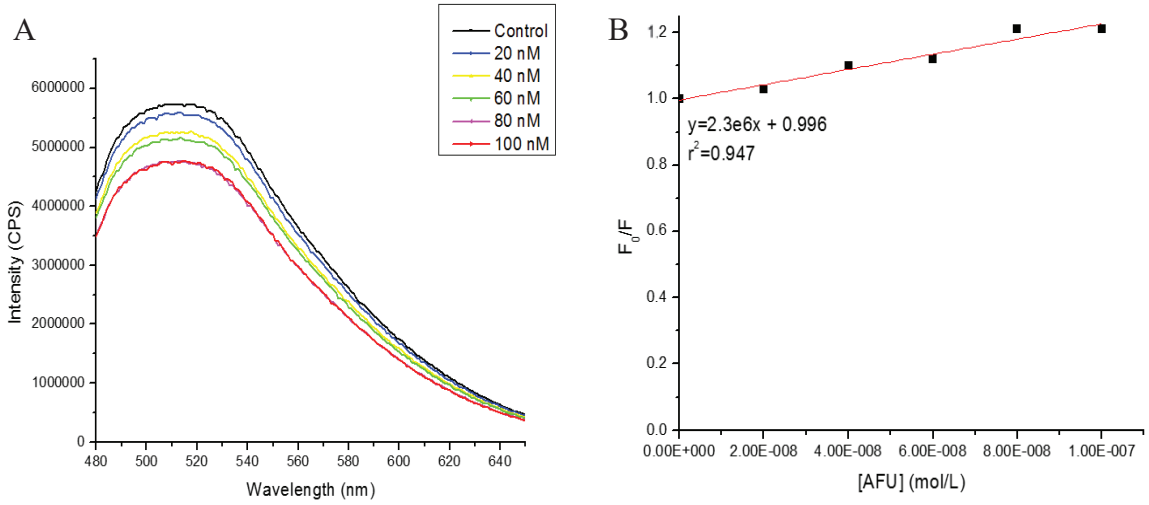

Figure 5.6 (A) Fluorescence emission spectrum of polyclonal anti-FUCA2 capped-gold nanoparticles with carbon dot labeled monoclonal detection antibody (ex. 460 nm) with increasing incubation concentrations of AFU and (B) Stern-Vølmer linear extrapolation.

5.5 Summary

To conclude, an immunoassay based upon a gold nanoparticle support was developed by monitoring the antigen concentration dependency on a carbon dot probe

emission. The assay was centered around energy transfer that occurs when the carbon dot probe emits photons near the surface plasmon of gold nanoparticles. The concept of the assay was optimized with a standard antigen, BSA. After optimizing the assay conditions, the gold nanoparticle immunoassay was modified for detection of AFU. A plot of F_0/F vs. the concentration of AFU produces a calibration curve that can later be used to determine the concentration of AFU in blood samples.

Chapter 6

Photodynamic Therapy Potential of Rose Bengal and Riboflavin-5'-Phosphate for Treating Methicillin-Resistant Staphylococcus Aureus Infections of the Cornea

6.1 Background

Inappropriate use of antibiotics to treat common infections has produced strains that express antibiotic resistance, such as methicillin-resistant *Staphylococcus aureus* (MRSA).[185,186] *Staphylococcus aureus* is one of the leading causes of bacterial keratitis.[187] With the observed increase in resistance, alternative treatment approaches must be developed. A promising way in which bacterial keratitis could be treated is through PDT.[188,189] PDT works by activating a sensitizing agent with a specific wavelength of irradiation, promoting the molecule to the excited state. For a molecule to be active for PDT, the sensitizer must undergo a Type I or Type II reaction with ambient oxygen to produce a cytotoxic agent to promote cell death.[117] The primary agent believed to be responsible for the apoptosis of cells treated by PDT is singlet oxygen.[190]

Measuring the quantum yield of singlet oxygen generation can be achieved via either a direct or indirect approach. Direct measurements of singlet oxygen require special instrumentation that can measure the luminescence of singlet oxygen in the near-infrared region at 1270 nm. Indirect approaches rely on monitoring a chemical trap added to a solution that will interact with singlet oxygen. The method of monitoring the solution is dependent upon which trap is being implemented, as there is a limited number of trap molecules known to interact with singlet oxygen. One of the more commonly used traps in measuring singlet oxygen is 1,3-diphenylisobenzofuran (DPBF).[191] **Figure 6.1** displays the ring opening reaction that occurs open interaction with singlet oxygen. The ring-opening results in the disappearance of an absorbance peak of DPBF at ~410

nm. By monitoring the disappearance of the absorption peak at 410 nm, the amount of DPBF that is reacting with singlet oxygen can be used to indirectly determine how much singlet oxygen is produced per photon of light for the photosensitizer used. However, one drawback in utilizing DPBF as a trap is the lack of water solubility. For measurements of singlet oxygen for treatment of keratitis, the sensitizer must be solubilized in aqueous media to limit damage to the cornea. Furfuryl alcohol (FA) is a water-soluble molecule that has been shown to be a singlet oxygen acceptor.[192] Using these two traps, it is possible to provide the quantum yield production of singlet oxygen in multiple solvent systems.

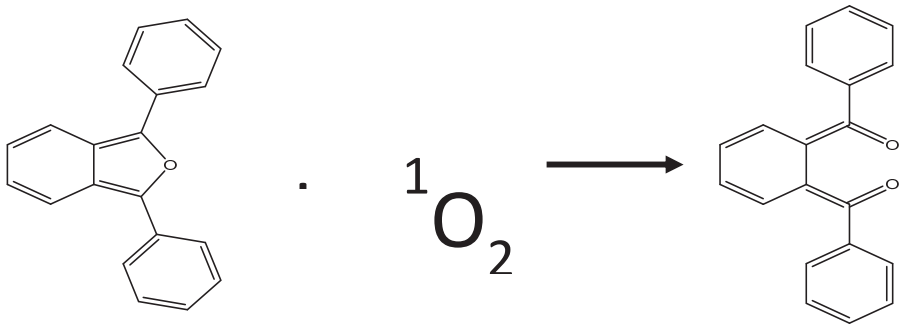

Figure 6.1 Ring opening reaction between DPBF and singlet oxygen

Rose Bengal (RB) is a fluorescein analog that has been shown to produce singlet oxygen.[193] Named for the deep red color this molecule emits, RB is a photosensitizer that has strong absorption in the green range. The efficacy of RB to inhibit bacterial growth through PDT has been investigated.[194] However, determining the proper concentration and irradiation period has been a challenge.[195] The photoreaction of RB has been researched and quantum yields have been reported between 0.68 and 0.86.[196,197] However, most all of the quantum yield values reported for RB are performed in organic

solvent. Accurate quantum yield calculations using the exact equipment utilized in PDT treatment must be established to validate the use of RB in PDT.

An additional sensitizer has been previously used for PDT in treatment of bacterial keratitis.[198] Riboflavin-5'-phosphate, also known as vitamin B_2, is a promising candidate for PDT due to the established corneal collagen cross-linking that occurs upon exposure to UV-A light.[199] Keratitis often results in deep ocular lesions after treatment with standard medication due to a cytokine response administered to rid toxins released from the infection.[200] The crosslinking observed upon PDT treatment offers a large improvement on the treatment of ocular infections due to the lack of ocular lesions left after PDT. However, riboflavin is not without limitations in PDT treatment. Riboflavin has limited solubility in nonaqueous solvents, and the reported quantum yield values for riboflavin are low (0.4-0.54).[201,202]

The following investigates the use of Rose Bengal and riboflavin as possible photosensitizers for treatment of bacterial keratitis. To determine the proper concentrations and irradiation period, the singlet oxygen quantum yield was determined for each photosensitizer using LED for the light source. Furthermore, radical scavengers were added to the photoreactions with each photosensitizer to determine if the cytotoxic agent produced underwent Type I, Type II or a combination of both reactions with ambient oxygen.

6.2 Experimental

6.2.1 Materials and methods

1,3-diphenylisobenzofuran and furfuryl alcohol were purchased from Alfa Aesar (Ward Hill, MA, USA). Rose Bengal and Riboflavin-5'-phosphate were provided by Sigma Aldrich (St. Louis, MO, USA).

6.2.2 Quantum yield measurements with optical trap

Solutions were prepared containing DPBF (90 μM) and Rose Bengal (OD=0.2 at the irradiation wavelength) filled to a volume of 2.8 mL in a quartz cuvette. The cuvette was then placed into a UV-vis spectrometer (Agilent Cary 100) and capped with an LED light fit to the cuvette. The irradiation was carried out by the LED light perpendicular to the direction of measurement. The LED light for Rose Bengal irradiation was a 525 nm LED, with a measured power of 6.11 x 10^{15} photons/s*cm^2 at the fixed distance of 5 mm from the solution. The time of irradiation was controlled by a computer tablet (Winbook TW700). The decay of DPBF was monitored at 410 nm over a minimum of 15 irradiation cycles. This process was repeated 15 times and one experiment contained the average decay measured from each run. The experiments were run in triplicate to ensure accuracy.

The quantum yield Φ_{DPBF} was calculated for each irradiation cycle using the following measured extinction coefficients: $\varepsilon_{methanol}$=24191 M^{-1} cm^{-1} and $\varepsilon_{ethanol}$=18488 M^{-1} cm^{-1} for DPBF at 410 nm. $\varepsilon_{methanol}$=37052 M^{-1} cm^{-1} and $\varepsilon_{ethanol}$=29957 M^{-1} cm^{-1} for Rose Bengal at 525 nm. The quantum yield of DPBF is calculated from the following equation: $\Phi_{DPBF} = -\frac{c_t - c_0}{\frac{I_{abs}}{V_R} \cdot t}$, where c_0 and c_t are the DPBF concentrations prior to and after irradiation, respectively, V_R is the reaction volume, t is the irradiation time per cycle

and I_{abs} is determined by: $I_{abs} = \alpha \cdot \frac{A \cdot P}{N_A}$, where α = 1- 10^{-E}, E is the absorbance of the sensitizer at the irradiation wavelength, *A* is the irradiated area, *P* is the intensity of light and N_A is Avogadro's constant.

The quantum yield of singlet oxygen was then calculated from the quantum yields of the photoreaction Φ_{DPBF} using $\frac{1}{\Phi_{DPBF}} = \frac{1}{\Phi_\Delta} + \frac{1}{\Phi_\Delta} \cdot \frac{k_d}{k_a} \cdot \frac{1}{[DPBF]}$, [203] where Φ_{DPBF} is the quantum yield of DPBF, Φ_Δ is the singlet oxygen quantum yield, k_d is the decay rate constant of singlet oxygen in the respective solvent and k_a is the rate constant of the reaction of DPBF with singlet oxygen. By plotting 1/ Φ_{DPBF} vs. 1/[DPBF], a linear Stern-Vølmer plot is produced and the intercept value obtained will be equal to 1/ Φ_Δ. By taking the inverse of the intercept value obtained, the quantum yield of singlet oxygen generation for Rose Bengal can be determined.

6.2.3 Quantum yield measurements with oxygen sensor

Solutions were prepared immediately before use and stored in the dark. A stock solution of furfuryl alcohol was prepared by adding 1 mL of furfuryl alcohol to a 100-mL volumetric flask and filling to capacity with ultrapure deionized water. A solution of the photosensitizer (Rose Bengal or Riboflavin-5'-phosphate) was made by dissolving approximately 5 mg of the sensitizer in 25 mL of deionized water. The photoreaction was run by preparing a 10 mL mixture in a vial containing 1 mL of the sensitizer and varying amounts of DPBF and water. Prior to running the photoreaction, a control vial was prepared matching the conditions with the highest amount of furfuryl alcohol but replacing the 1 mL of sensitizer with 1 mL of water.

After a sample was prepared, the photoreaction was run immediately by first saturating the solution with oxygen for ~10 minutes. Upon saturation, a 2.8 mL aliquot

was taken from the vial and transferred to cuvette sealed with a septum and the initial oxygen concentration was measured using a NEOFOX Oxygen Sensor (Ocean Optics) that was calibrated each day prior to running experiments. After measuring the initial oxygen concentration, the probe was removed and the cuvette was transferred to a spectrometer and the initial concentration of the sensitizer and furfuryl alcohol was measured. Next, an LED (525 nm for Rose Bengal and 410 nm for Riboflavin) was placed parallel to the detector 1 mm from the center of the cuvette, and the sample was irradiated for exactly180 seconds controlled by a computer tablet. The % transmittance was monitored during irradiation to obtain an average number of photons absorbed by the photosensitizer. After irradiation was terminated, the final concentration of the sensitizer and furfuryl alcohol was monitored and then the final oxygen concentration was obtained. The concentration of furfuryl alcohol and the sensitizers was determined using the following measured extinction coefficients: ε_{water}=8791 M^{-1} cm^{-1} for furfuryl alcohol at 215 nm, ε_{water}=33053 M^{-1} cm^{-1} for Rose Bengal at 525 nm, and ε_{water}=6063 M^{-1} cm^{-1} for riboflavin-5'-phosphate at 400 nm.

The quantum yield of the acceptor (A) furfuryl alcohol was calculated from the following equation:[204] $\Phi_{AO2} = \frac{nO_2}{n_{abs\,\lambda}} = \Phi^1O_2 \times \alpha \times \frac{k_r[A]}{k_d + (k_r + k_q)[A]}$, where Φ_{AO2} is the quantum yield of the photoreaction with the acceptor, nO_2 is the molecules of oxygen consumed, $n_{abs\lambda}$ is the photons absorbed at the irradiation wavelength, k_r is the rate constant of the chemical reaction, k_q is the rate constant of physical quenching and k_d is the rate constant of the natural decay of singlet oxygen to triplet oxygen.

As long as the rate constant of physical quenching, k_q, is insignificant to the rate constant of the chemical reaction, k_r, then the singlet oxygen quantum yield can be determined from the intercept of a plot of $\frac{1}{\Phi_{AO2}}$ vs. $\frac{1}{[A]}$.

6.3 Quantum yield of Rose Bengal and riboflavin-5'-phosphate

6.3.1 Optical quenching approach with 1,3-diphenylisobenzofuran trap

The overall goal is to determine the efficacy of Rose Bengal and riboflavin-5'-phosphate as sensitizers for use in photodynamic therapy. To determine the efficacy of each sensitizer, the quantum yield of singlet oxygen must be calculated. Singlet oxygen values have been measured for both Rose Bengal and Riboflavin, however, there is a large amount of variance in the value obtained based on the irradiation source, the measurement procedure, as well as the solvent system. DPBF is a well-established acceptor for singlet oxygen. Many groups have utilized this trap due to its inherent low oxidation potential and its minimal reactivity towards other oxidants has been observed.[191] Thus, DPBF was chosen for initial measurements to determine if the LED light source was powerful enough to activate a sensitizer and to validate the experimental results obtained from the measurement process with literature values.

Solvent	$^1O_2$ lifetime (μs)
Water	2
Deuterated water	68
Methanol	7
Ethanol	11
Hexane	24
Chloroform	247

Table 6.1 Lifetime of singlet oxygen in various common solvents.

To begin measuring the singlet oxygen quantum yield for Rose Bengal and riboflavin-5'-phosphate, the measurement conditions were first optimized. One of the variables that effects the quantum yield of singlet oxygen is the solvent system used. As **Table 6.1** displays, the lifetime of singlet oxygen can drastically vary depending upon the solvent chosen. Although DPBF is a standard trap used for singlet oxygen, it is not possible to use in measurements with aqueous media, due to a lack of solubility and a tendency for DPBF to dimerize in the presence of water, which mitigates its reactivity towards singlet oxygen.[190,205,206] With this in mind, the initial measurements using DPBF were done in methanol and ethanol. Ethanol provided better results than methanol and was used for the rest of the measurements with DPBF. However, performing the measurements in alcohol proved to be impossible for riboflavin, as it experienced very poor solubility and was thus excluded from measurement in this process.

Another variable that had to be optimized was the concentration of the sensitizer and trap. To provide consistency for the sensitizer utilized, the concentration of the

sensitizer was set so that an optical density of 0.2 was measured at the irradiation wavelength. The concentration of DPBF was initially attempted at 80 µM, however, the measurements obtained expressed poor kinetics. Concentrations lower than 80 µM provided no apparent improvement. At concentrations over 100 µM, the detector on the spectrometer was saturated, so the optimal concentration was found to be 90 µM, which experience a slight improvement upon 80 µM.

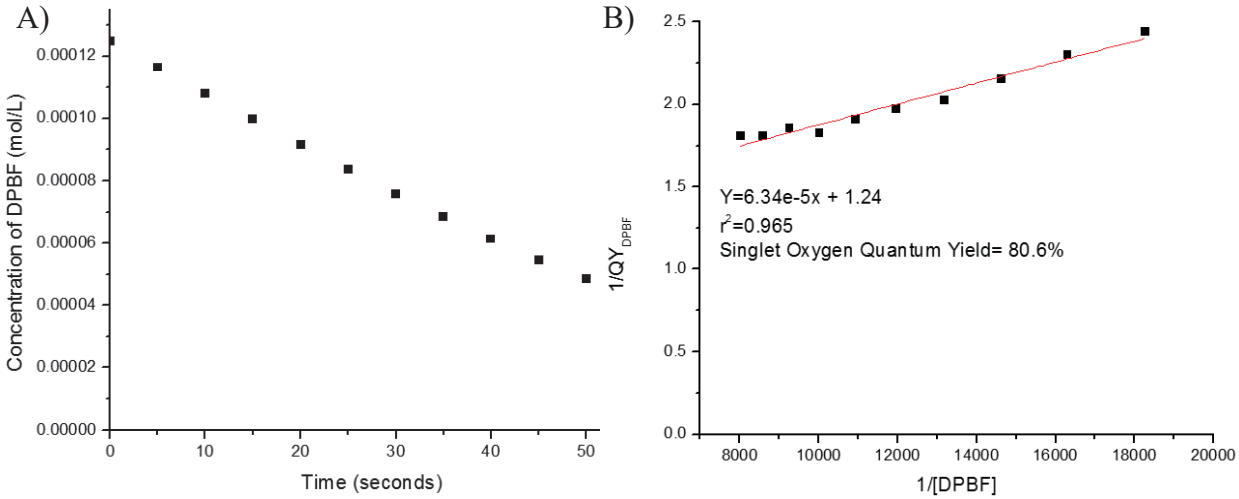

Figure 6.2 (A) Decay of 90 µM DPBF in ethanol from 5 second irradiation cycles with Rose Bengal (O.D.=0.2) and (B) plot of $1/\Phi_{DPBF}$ vs. 1/[DPBF].

The final variable manipulated was the irradiation time. Using two second irradiation cycles was found to be too short. Three second cycles would produce a decay of DPBF, however, five second cycles provided the most similarity to literature results of Rose Bengal's quantum yield for singlet oxygen generation. By measuring the quantum yield of the photooxidation of DPBF ($\Phi_{DPBF} = -\frac{c_t - c_0}{\frac{I_{abs}}{V_R} \cdot t}$), the quantum yield of singlet oxygen can be extrapolated by taking the inverse of the intercept of a plot of $1/\Phi_{DPBF}$ vs. 1/[DPBF] ($\frac{1}{\Phi_{DPBF}} = \frac{1}{\Phi_\Delta} + \frac{1}{\Phi_\Delta} \cdot \frac{k_d}{k_a} \cdot \frac{1}{[DPBF]}$). **Figure 6.2B** shows the plot of $1/\Phi_{DPBF}$ vs. 1/[DPBF] with the sensitizer Rose Bengal (5.5 µM) in ethanol with five second

irradiation cycles. The singlet oxygen quantum yield, Φ_{Δ}, was found to be 80.6%, which is in agreement with other reported results.[191,196,197]

As mentioned in **6.1** above, it is possible that the photosensitizer is going through a Type I process, Type II process or a combination of the two. The Type II process is responsible for generation of singlet oxygen while Type I will create a radical species or superoxide radical anion. If the photosensitizer is creating a radical species, adding a radical scavenger would result in less DPBF being consumed upon irradiation and the calculated singlet oxygen quantum yield would decrease. By adding the radical scavenger NaI (3 mM), there a noticeable decrease in the singlet oxygen quantum yield for Rose Bengal (**Figure 6.3**). This indicates that upon irradiation of Rose Bengal, both Type I and II processes occur. The singlet oxygen quantum yield only reduced by ~20% adding the radical scavenger, which indicates that while the Type I process does occur, the Type II process is the dominant process for Rose Bengal.

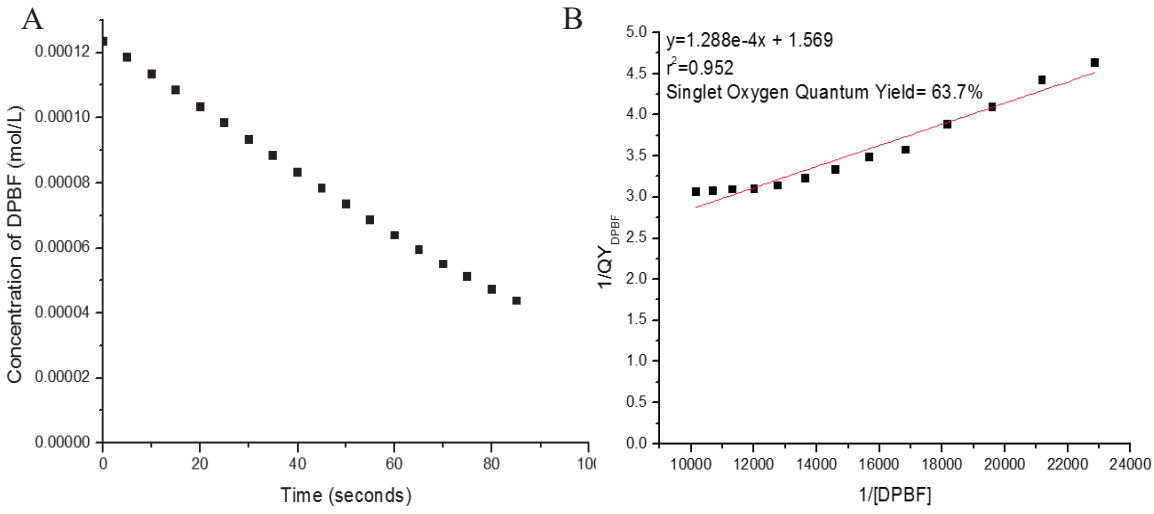

Figure 6.3 (A) Decay of 90 µM DPBF in ethanol with 3 mM NaI from 5 second irradiation cycles with Rose Bengal (O.D.=0.2) and (B) plot of $1/\Phi_{DPBF}$ vs. 1/[DPBF].

6.3.2 Oxygen sensor approach with furfuryl alcohol

To use a sensitizer for photodynamic therapy on the cornea, the photosensitizer must be used in aqueous media. The quantum yield cannot be measured in aqueous solutions using DPBF, so an alternative trap was needed. Furfuryl alcohol is a water soluble singlet oxygen acceptor that has previously been studied.[192,207] To determine Φ_Δ for Rose Bengal in water, the method used in ***6.3.1*** was attempted first by simply replacing DPBF with furfuryl alcohol. However, the experiment did not work because the decay of furfuryl alcohol at 215 nm was found to have too much variance. It has been previously noted that furfuryl alcohol produces a mixture of oxidative products, and it is likely that these products are interfering with detection of furfuryl alcohol by this method.[208,209]

To fix issues in measuring the decay of an absorption peak, an alternative approach was used based upon the consumption of oxygen. The quantum yield of singlet oxygen can be related to the amount of oxygen consumed by the following equation extrapolated from the kinetics of oxygen excitation, $\Phi_{AO2} = \frac{nO_2}{n_{abs\,\lambda}} = \Phi^1O_2 \times \alpha \times \frac{k_r[A]}{k_d + (k_r + k_q)[A]}$. By measuring Φ_{AO2} at different concentrations of furfuryl alcohol, a plot of $\frac{1}{\Phi_{AO2}}$ vs. $\frac{1}{[A]}$ can be produced in which the inverse of the y-intercept of a linear plot will be equal to Φ_Δ ($\frac{1}{\Phi_{AO2}} = \beta \frac{k_r + k_q}{\alpha \times \Phi^1O_2 \times k_r} \times \frac{1}{[A]}$).

Vial	FA Added (mL)	Sensitizer Added (mL)	Water Added (mL)
Control	9	0	1
1	9	1	0
2	7	1	2
3	5	1	4
4	3	1	6
5	2	1	7
6	1	1	8
7	0.5	1	8.5

Table 6.2 Experimental conditions used to measure quantum yield with oxygen sensor.

To calculate Φ_Δ in water, stock solutions prepared as described in ***6.2.3*** were mixed as shown in **Table 6.2**. To begin the experiment, a control was prepared in which no sensitizer was added. The control blank served two purposes: to prove the change in oxygen was due to the presence of the photosensitizer and to establish the baseline number of photons produced by the LED light source during the irradiation cycle. **Figure 6.4** portrays an example plot obtained by measuring the photons absorbed by the sensitizer. A noticeable difference is observed in the presence of the photosensitizer. The difference was used to determine the energy absorbed which was then converted into photons/s*cm^2 using Planck's equation ($E=hc/\lambda$). To determine the number of molecules of oxygen consumed, the concentration of oxygen in each sample was measured before and after irradiation, and the difference in concentration was then converted to molecules of oxygen, allowing a plot of $1/\Phi_{AO2}$ (# of photons absorbed/molecules of oxygen consumed) vs. 1/[FA] to be produced.

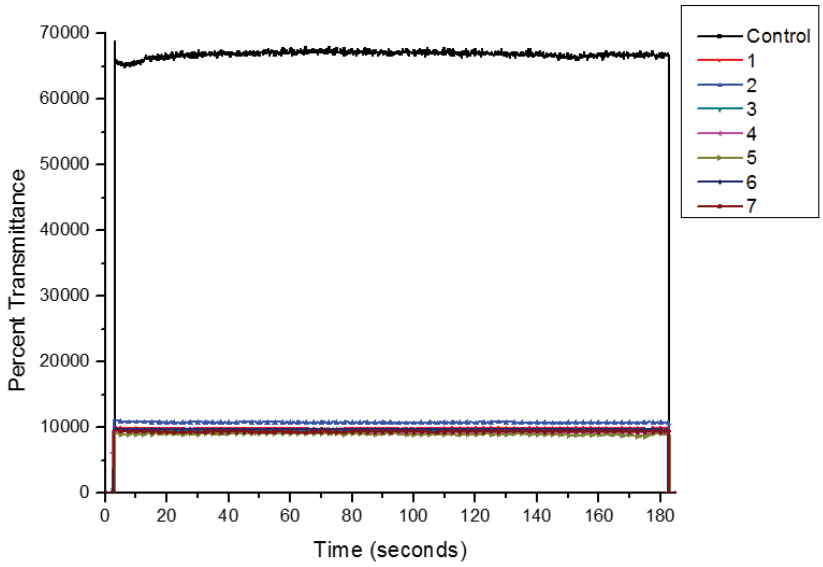

Figure 6.4 Plot of the LED power output over the course of 180 seconds on PDT.

A similar result to the previous method was obtained for the Φ_Δ for RB in water, as shown in **Figure 6.5A**. Additionally, the oxygen sensor approach was attempted with the inclusion of the radical scavenger NaI to determine if the Type I process is occurring. About a 20% decrease in the singlet oxygen quantum yield for RB with the radical scavenger present was noted, which possesses good correlation with the results obtained with DPBF (**Figure 6.5B**).

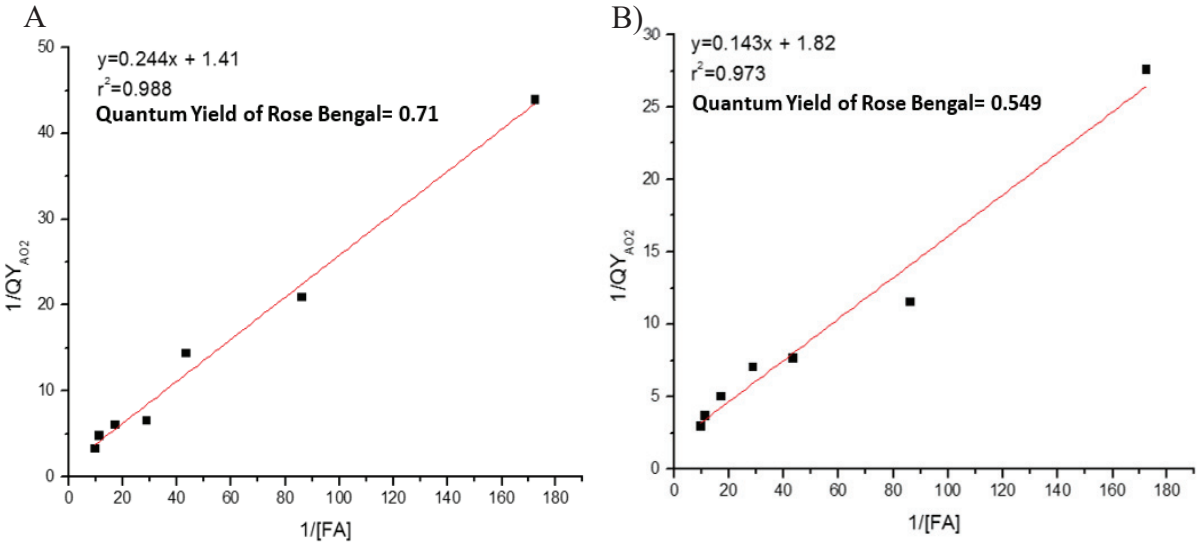

Figure 6.5 (A) Quantum yield of singlet oxygen from RB in water with FA trap and (B) quantum yield of singlet oxygen from RB in water with FA trap and radical scavengers.

While it was not possible to measure the Φ_Δ for riboflavin-5'-phosphate using DPBF, it was possible to use with FA. Experiments were prepared in the exact same manner as done for RB, simply substituting RB with riboflavin-5'-phosphate. As **Figure 6.6A** shows, the quantum yield of singlet oxygen generation is significantly lower for riboflavin-5'-phosphate. However, upon addition of the radical scavenger NaI, there is virtually no change in the quantum yield measured (**Figure 6.6B**). This indicates that while riboflavin-5'-phosphate is a weaker photosensitizer for generating singlet oxygen than RB, the irradiation of riboflavin-5'-phosphate does not appear to include the presence of any species from a Type I process.

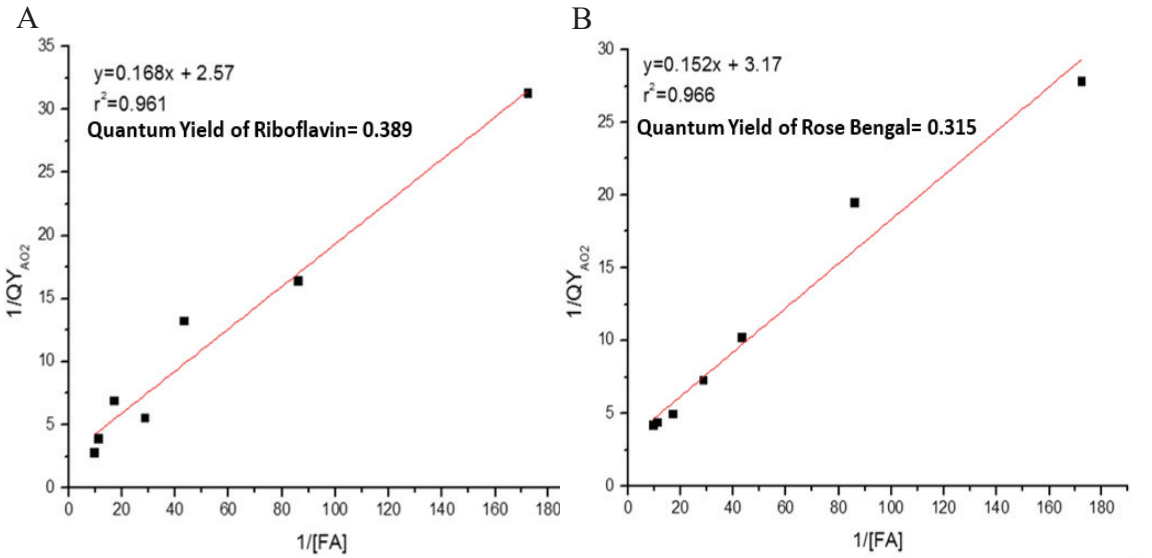

Figure 6.6 (A) Quantum yield of singlet oxygen from riboflavin in water with FA trap and (B) quantum yield of singlet oxygen from riboflavin in water with FA trap and radical scavengers.

6.4 Summary

In summation, the quantum yield of singlet oxygen generation was measured for Rose Bengal and riboflavin-5'-phosphate. The singlet oxygen quantum yield for Rose Bengal was confirmed using two different methods, with the values produced found to be

in good correlation with other reported yields. The irradiation process of Rose Bengal expressed both Type I and Type II processes, with the Type II process being dominant. Riboflavin-5'-phosphate was found to be predominantly Type II, however, the total yield is lower than that of Rose Bengal.

Chapter 7

Future Directions

7.1 Validating alpha-L-fucosidase as a biomarker for detection of hepatocellular carcinoma

7.1.1 Quartz slide assay detection of alpha-L-fucosidase in blood serum

Upon determining the quartz slide assay could detect alpha-L-fucosidase in PBS (**Ch. 4.4**), the assay will next need to be confirmed in human blood serum. To do this, samples of human blood serum will be purchased. Healthy adults do not produce alpha-L-fucosidase, so none should be present in the blood samples. AFU will be added to the blood serum, as was done in PBS, and incubated at 37° C for 30 minutes. After the incubation, the slide will be rinsed thoroughly with deionized water, then placed into a quartz cuvette filled with ultrapure deionized water and the fluorescence of the Rhodamine probe will be measured. A calibration curve for detection of AFU in blood can then be produced by plotting F_0/F vs. the concentration of AFU.

7.1.2 Gold nanoparticle immunoassay detection of alpha-L-fucosidase in human blood serum

A calibration curve for the gold nanoparticle immunoassay was produced in PBS, but one must be produced for human blood serum. To achieve this, the polyclonal anti-FUCA2-capped gold nanoparticles will be incubated in healthy blood serum in increasing amounts of AFU for 30 minutes at 37° C. After 30 minutes, the carbon dot labeled monoclonal anti-FUCA2 detection antibody will be added to the blood serum and incubated for an additional 30 minutes at 37° C. The blood sample will then be centrifuged, the blood serum will be removed and the gold nanoparticle pellet will be re-

suspended in PBS buffer. The fluorescence emission will then be measured at the increasing concentrations of AFU and a plot of F_0/F vs. the concentration of AFU will be produced.

7.1.3 Confirm alpha-L-fucosidase is an effective biomarker for hepatocellular carcinoma using quartz slide and gold nanoparticle immunoassays

After proving the quartz slide and gold nanoparticle immunoassay's can efficiently detect AFU in human blood, they can then be used to detect HCC. To do this, samples must be obtained from healthy individuals, as well as, samples from those who are confirmed to have HCC. A diversity in samples will be necessary, evenly spanning a range of age, genders and nationalities. The assay will be run incubating the quartz slide or gold nanoparticles in each blood sample at 37° C for 1 hour. The slide will then be thoroughly rinsed with ultrapure deionized water, then the fluorescence of the Rhodamine probe will be measured, while the gold nanoparticles will be centrifuged, re-suspended in PBS and the fluorescence of the carbon dot probe will be measured. Calculating F_0/F for each blood sample will allow the concentration of AFU to be determined using the calibration curves from ***7.1.1*** and ***7.1.2***. After compiling the concentration of AFU in each sample, the cut-off level of AFU will be determined by observing the levels of AFU that correlate to positive cases of HCC.

7.2 Determine the effect photodynamic therapy has on Methicillin-resistant Staphylococcus aureus

7.2.1 Background

It has been previously proven that photodynamic therapy can induce cytotoxicity. However, the changes that occur upon PDT at the molecular level have not been

established. Using Rose Bengal to treat infections in the cornea has proven to limit the damage that occurs from treatment with traditional antibiotics. It is believed that toxins produced by the bacteria are responsible for the observed ocular damage. Antibiotics destroy the bacteria, but leave these toxic by-products behind. It has been hypothesized that the lack of residual damage upon PDT treatment may be a result of singlet oxygen reacting with these toxic by-products and rendering them biologically inert.

7.2.2 Preliminary data

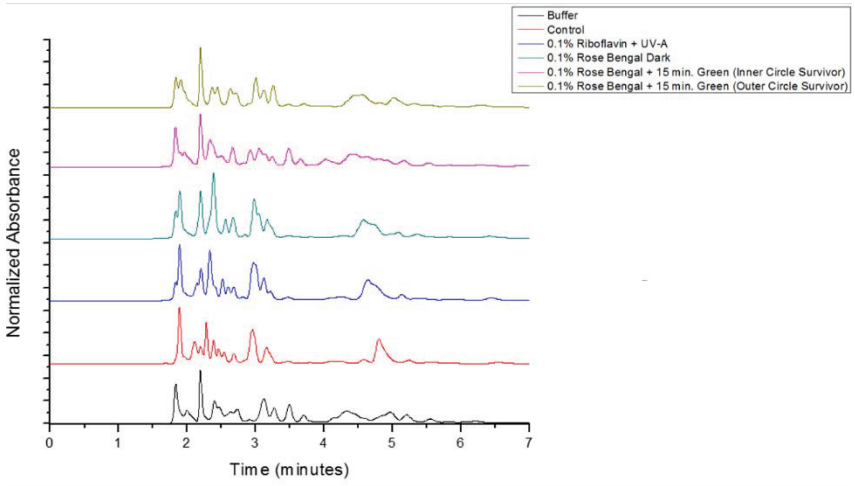

Figure 7.1 HPLC separation of MRSA lysate broth under various PDT conditions (detection at 266 nm).

To determine the effect that PDT has on toxic by-products, the lysates of several different strands of MRSA that had undergone various forms of PDT were monitored via HPLC. The goal of the HPLC experiment was to separate the individual components found in the MRSA lysate broth and to observe any changes that PDT triggered. As shown in **Figure 7.1**, the differences that occur upon PDT treatment are inconclusive. The signal for most of the analytes observed was below the detection limit for the spectrometer and the separation of each analyte was poor. Furthermore, the HPLC detection was limited only to analytes that absorb photons between 200-800 nm. Some

of the toxic by-products and other analytes present in the MRSA lysate are missed by this method of detection.

7.2.3 ESI/MS-HPLC for determining the effect of photodynamic therapy on Methicillin resistant staphylococcus aureus

Determining the effect of PDT of MRSA proved to be insufficient with a diode array detector. To resolve this complication, an electrospray ionization mass spectrometer (ESI/MS) detector can be used instead. ESI/MS detects the analyte based upon mass, allowing all analytes to be observed. Furthermore, ESI/MS is a more sensitive detection approach than absorption spectroscopy and can detect analytes at much lower concentrations.

References

(1) Tiwari, S.; Tripathi, I. P.; Tiwari, H. L. *Res. J. Chem. Sci.* **2013**, *3*, 86.

(2) Martinez-Finley, E. J.; Aschner, M. *Curr. Envir. Health Rpt.* **2014**, *1*, 163.

(3) Di Toro, D. M.; Mahony, J. D.; Hansen, D. J.; Scott, K. J.; Hicks, M. B.; Mayr, S. M.; Redmond, M. S. *Environ. Toxicol. Chem.* **1990**, *9*, 1487.

(4) Bertin, G.; Averbeck, D. *Biochimie* **2006**, *88*, 1549.

(5) Cram, D. J. C., J. M. *Science* **1974**, *183*, 803.

(6) Biros, S. M.; Rebek, J. J. *Chem. Soc. Rev.* **2007**, *36*, 93.

(7) Böhmer, V. *Angewandte Chemie (International ed. in English)* **1995**, *34*, 713.

(8) Gutsche, C. D. In *Calixarenes*; The Royal Society of Chemistry: Cambridge, 1989.

(9) Ikeda, A.; Shinkai, S. *Chem. Rev.* **1997**, *97*, 1713.

(10) Lagona, J.; Mukhopadhyay, P.; Chakrabarti, S.; Isaacs, L. *Angew Chem Int Ed Engl* **2005**, *44*, 4844.

(11) Masson, E.; Ling, X.; Joseph, R.; Kyeremeh-Mensah, L.; Lu, X. *R. Soc. Chem. Adv.* **2012**, *2*, 1213.

(12) Lee, J. W.; Samal, S.; Selvapalam, N.; Kim, H.-J.; Kim, K. *Acc. Chem. Res.* **2003**, *36*, 621.

(13) D'Souza, V. T.; Lipkowitz, K. B. *Chem. Rev.* **1998**, *98*, 1741.

(14) Rullaud, V.; Siragusa, M.; Cumbo, A.; Gygax, D.; Shahgaldian, P. *Chem. Commun.* **2012**, *48*, 12186.

(15) Rullaud, V.; Moridi, N.; Shahgaldian, P. *Langmuir* **2014**, *30*, 8675.

(16) Basílio, N.; Francisco, V.; García-Río, L. *J. Org. Chem.* **2012**, *77*, 10764.

(17) Cafeo, G.; Gattuso, G.; Kohnke, F. H.; Papanikolaou, G.; Profumo, A.; Rosano, C. *Chem. Eur. J.* **2014**, *20*, 1658.

(18) Lonetti, B.; Lo Nostro, P.; Ninham, B. W.; Baglioni, P. *Langmuir* **2005**, *21*, 2242.

(19) Gulino, A.; Lupo, F.; Cristaldi, D. A.; Pappalardo, S.; Capici, C.; Gattuso, G.; Notti, A.; Parisi, M. F. *Eur. J. Inorg. Chem.* **2014**, *2014*, 442.

(20) Shahgaldian, P.; Sciotti, M. A.; Pieles, U. *Langmuir* **2008**, *24*, 8522.

(21) Chinai, J. M.; Taylor, A. B.; Ryno, L. M.; Hargreaves, N. D.; Morris, C. A.; Hart, P. J.; Urbach, A. R. *Journal of the American Chemical Society* **2011**, *133*, 8810.

(22) Tabakci, B.; Yilmaz, M.; Beduk, A. D. *J. Appl. Polym. Sci.* **2012**, *125*, 1012.

(23) González-Delgado, A. M.; Giner-Casares, J. J.; Brezesinski, G.; Regnouf-de-Vains, J.-B.; Camacho, L. *Langmuir* **2012**, *28*, 12114.

(24) Park, S. Y.; Yoon, J. H.; Hong, C. S.; Souane, R.; Kim, J. S.; Matthews, S. E.; Vicens, J. *J. Org. Chem.* **2008**, *73*, 8212.

(25) Supian, F. L.; Richardson, T. H.; Deasy, M.; Kelleher, F.; Ward, J. P.; McKee, V. *Langmuir* **2010**, *26*, 10906.

(26) Zhou, R.; Srinivasan, M. P. *Langmuir* **2013**, *29*, 13042.

(27) Fang, Y.-X.; Zhao, L.; Wang, D.-X.; Wang, M.-X. *J. Org. Chem.* **2012**, *77*, 10073.

(28) Strutt, N. L.; Zhang, H.; Schneebeli, S. T.; Stoddart, J. F. *Acc. Chem. Res.* **2014**.

(29) McCartney, C. M.; Cowlam, N.; Davis, F.; Richardson, T.; Desert, A.; Gibaud, A.; Stirling, C. J. M. *Colloids and Surf. A* **2013**, *436*, 41.

(30) Zhang, Q.; Catti, L.; Kaila, V. R. I.; Tiefenbacher, K. *Chem. Sci.* **2017**, *8*, 1653.

(31) Jebors, S. F., F; Balme, S.; Devoge, F.; Monachino, M.; Cecillon, S.; Coleman, A. W. *Org. Biomol. Chem.* **2008**, *6*, 319.

(32) Ariga, K.; Sakakibara, K.; Richards, G. J.; Hill, J. P. *Supramol. Chem.* **2011**, *23*, 183.

(33) Markowits, M. A.; Bielski, R.; Regen, S. L. *J. Am. Chem. Soc.* **1988**, *110*, 7545.

(34) Li, S.; Mulloor, J. J.; Wang, L.; Ji, Y.; Mulloor, C. J.; Micic, M.; Orbulescu, J.; Leblanc, R. M. *ACS Appl. Mater. Interfaces* **2014**, *6*, 5704.

(35) Cornec, M.; Cho, D.; Narsimhan, G. *Journal of Colloid and Interface Science* **1999**, *214*, 129.

(36) Lednev, I. K.; Petty, M. C. *Adv. Mater.* **1996**, *8*, 615.

(37) Hassan, A. K.; Nabok, A. V.; Ray, A. K.; Davis, F.; Stirling, C. J. M. *Thin Solid Films* **1998**, *327–329*, 686.

(38) George L. Gaines, J. *Interscience Publishers* **1966**.

(39) Liu, G.; Yang, S.; Zhang, G. *J. Phys. Chem. B* **2007**, *111*, 3633.

(40) Thakur, G.; Micic, M.; Leblanc, R. M. *Colloids Surf. B: Biointerfaces* **2009**, *74*, 436.

(41) Zhang, S.; Song, F.; Echegoyen, L. *Eur. J. Org. Chem.* **2004**, *2004*, 2936.

(42) Wrobel, E. C.; Santos, P. M.; Lazzarotto, M.; Oliveira, O. N.; Uehara, T. M.; Miranda, P. B.; Caseli, L.; Garcia, J. R.; de Lazaro, S. R.; Camilo Jr, A.; Wohnrath, K. *Phys. Chem. Chem. Phys.* **2014**, *16*, 26168.

(43) *World Cancer Report 2017*; IARC, 2017.

(44) Dai, L.; Lei, N.; Liu, M.; Zhang, J.-Y. *Exp. Hematol. Oncol.* **2013**, *2*, 15.

(45) Zhao, Y.; Ju, Q.; Li, G. *Mol. Clin. Oncol.* **2013**, *1*, 593.

(46) Shiraha, H.; Yamamoto, K.; Namba, M. *Int. J. Oncol.* **2013**, *42*, 1133.

(47) Lehman, E. M.; Soliman, A. S.; Ismail, K.; Hablas, A. A. S. I.; Ramadan, M.; El-Hamzawy, K. H.; Shoustari, C. S. *Hepatol. Res.* **2008**, *38*, 456.

(48) Tangkijvanich, P.; Tosukhowong, P.; Bunyongyod, P.; Lertmaharit, S.; Hanvjvatvong, O.; Kullavanijaya, P.; Poovorawan, Y. *Southeast Asian J. Trop. Med. Public Health* **1999**, *30*, 110.

(49) Al-Eid, H. S.; Quindo, M. A. *Kingdom of Saudi Arabia Council of Health Services Saudi Cancer Registry* **2014**, 1.

(50) Nguyen, M. H.; Garcia, R. T.; Simpson, P. W.; Wright, T. L.; Keeffe, E. B. *Hepatology* **2002**, *36*, 410.

(51) Nissen, N. N.; Martin, P. *J. Clin. Gastroenterol.* **2002**, *35*, S79.

(52) Seto, W.-K.; Lai, C.-L.; Yuen, M.-F. In *Cancer and Inflammation Mechanisms*; John Wiley & Sons, Inc.: 2014, p 181.

(53) Tanaka, H.; Imai, Y.; Hiramatsu, N.; Ito, Y.; Imanaka, K.; Oshita, M.; Hijioka, T.; Katayama, K.; Yabuuchi, I.; Yoshihara, H.; Inoue, A.; Kato, M.; Takehara, T.; Tamura, S.; Kasahara, A.; Hayashi, N.; Tsukuma, H. *Ann. Intern. Med.* **2008**, *148*, 820.

(54) Trichopoulos, D.; Bamia, C.; Lagiou, P.; Fedirko, V.; Trepo, E.; Jenab, M.; Pischon, T.; Nöthlings, U.; Overved, K.; Tjønneland, A.; Outzen, M.; Clavel-Chapelon, F.; Kaaks, R.; Lukanova, A.; Boeing, H.; Aleksandrova, K.; Benetou, V.; Zylis, D.; Palli, D.; Pala, V.; Panico, S.; Tumino, R.; Sacerdote, C.; Bueno-De-Mesquita, H. B.; Van Kranen, H. J.; Peeters, P. H. M.; Lund, E.; Quirós, J. R.; González, C. A.; Sanchez Perez, M.-J.; Navarro, C.; Dorronsoro, M.; Barricarte, A.; Lindkvist, B.; Regnér, S.; Werner, M.; Hallmans, G.; Khaw, K.-T.; Wareham, N.; Key, T.; Romieu, I.; Chuang, S.-C.; Murphy, N.; Boffetta, P.; Trichopoulou, A.; Riboli, E. *J. Natl. Cancer Inst.* **2011**, *103*, 1686.

(55) Kuper, H.; Tzonou, A.; Kaklamani, E.; Hsieh, C.-C.; Lagiou, P.; Adami, H.-O.; Trichopoulos, D.; Stuver, S. O. *Int. J. Cancer* **2000**, *85*, 498.

(56) Yasui, K.; Hashimoto, E.; Komorizono, Y.; Koike, K.; Arii, S.; Imai, Y.; Shima, T.; Kanbara, Y.; Saibara, T.; Mori, T.; Kawata, S.; Uto, H.; Takami, S.; Sumida, Y.; Takamura, T.; Kawanaka, M.; Okanoue, T. *Clin. Gastroenterol. Hepatol.* **2011**, *9*, 428.

(57) Ozturk, M. *Lancet* **1991**, *338*, 1356.

(58) Chen, C.; Wang, L.; Lu, S.; Wu, M.; You, S.; Zhang, Y.; Wang, L.; Santella, R. M. *Hepatology* **1996**, *24*, 38.

(59) Umesha, S.; Manukumar, H. M. g.; Chandrasekhar, B.; Shivakumara, P.; Shiva Kumar, J.; Raghava, S.; Avinash, P.; Shirin, M.; Bharathi, T. R.; Rajini, S. B.; Nandhini, M.; Vinaya Rani, G. g.; Shobha, M.; Prakash, H. S. *J. Sci. Food Agric.* **2017**, *97*, 1698.

(60) Bokhari, F. M. *Pak. J. Biol. Sci.* **2002**, *5*, 69.

(61) Van Rensburg, S. J.; Cook-Mozaffari, P.; Van Schalkwyk, D. J.; Van der Watt, J. J.; Vincent, T. J.; Purchase, I. F. *Br. J. Cancer* **1985**, *51*, 713.

(62) Tejeda-Maldonado, J.; García-Juárez, I.; Aguirre-Valadez, J.; González-Aguirre, A.; Vilatobá-Chapa, M.; Armengol-Alonso, A.; Escobar-Penagos, F.; Torre, A.; Sánchez-Ávila, J.; Luis Carrillo-Pérez, D. *World J. Hepatol.* **2015**, *7*, 362.

(63) Tjalsma, H. *Expert Rev. Proteomic* **2010**, *7*, 879.

(64) Nilsson, B. *Curr. Opin Immunol.* **1989**, *2*, 898.

(65) Chayvialle, J. A.; Ganguli, P. C. *Lancet* **1973**, *1*, 1355.

(66) Chen, Z.; Ren, X.; Meng, X.; Zhang, Y.; Chen, D.; Tang, F. *Anal. Chem.* **2012**, *84*, 4077.

(67) Tsay, G. C.; Dawson, G. *Anal. Biochem.* **1976**, *78*, 423.

(68) Othman, A. M.; El-Houseini, M. E.; El-Sofy, M. S.; Aboul-Enein, H. Y. *Anal Bioanal Chem* **2011**, *400*, 787.

(69) Hutter, E.; Fendler, J. H. *Adv. Mater.* **2004**, *16*, 1685.

(70) Ijichi, M.; Takayama, T.; Matsumura, M.; Shiratori, Y.; Omata, M.; Makuuchi, M. *Hepatology* **2002**, *35*, 853.

(71) Okuda, H.; Nakanishi, T.; Takatsu, K.; Saito, A.; Hayashi, N.; Yamamoto, M.; Takasaki, K. E. N.; Nakano, M. *J. Gastroenterol. Hepatol.* **2002**, *17*, 772.

(72) Tang, W.; Kokudo, N.; Sugawara, Y.; Guo, Q.; Imamura, H.; Sano, K.; Karako, H.; Qu, X.; Nakata, M.; Makuuchi, M. *Oncol. Rep.* **2005**, *13*, 25.

(73) Zhou, L.; Liu, J.; Luo, F. *World J. Gastroenterol.* **2006**, *12*, 1175.

(74) Mizejewski, G. J. *Exp. Biol. Med.* **2001**, *226*, 377.

(75) Taketa, K.; Okada, S.; Win, N.; Hlaing, N. K. T.; Win, K. M. *Acta Med. Okayama* **2002**, *56*, 317.

(76) Taketa, K. *Hepatology* **1990**, *12*, 1420.

(77) Trevisani, F.; D'Intino, P. E.; Morselli-Labate, A. M.; Mazzella, G.; Accogli, E.; Caraceni, P.; Domenicali, M.; De Notariis, S.; Roda, E.; Bernardi, M. *J. Hepatol.* **2001**, *34*, 570.

(78) Mancal, P.; Srámek, M.; Malbohan, I.; Simek, L. *J. Hyg. Epidemiol. Microbiol. Immunol.* **1988**, *32*, 209.

(79) Choi, J. Y.; Jung, S. W.; Kim, H. Y.; Kim, M.; Kim, Y.; Kim, D. G.; Oh, E.-J. *World J. Gastroenterol.* **2013**, *19*, 339.

(80) Attia, M. S.; Othman, A. M.; Aboaly, M. M.; Abdel-Mottaleb, M. S. A. *Anal. Chem.* **2010**, *82*, 6230.

(81) Liu, J.; Gao, Y.; Yang, B.; Jia, X.; Zhai, D.; Li, S.; Zhang, Q.; Jing, L.; Wang, Y.; Du, Z.; Wang, Y. *Arch. Med. Res.* **2015**, *46*, 133.

(82) Cui, R.; He, J.; Zhang, F.; Wang, B.; Ding, H.; Shen, H.; Li, Y.; Chen, X. *Br. J. Cancer* **2003**, *88*, 1878.

(83) Hanigan, M. H.; Pilot, H. C. *Carcinogenesis* **1985**, *6*, 165.

(84) Curthoys, N. P.; Hughey, R. P. *Enzyme* **1979**, *24*, 383.

(85) Matsuda, Y.; Tsuji, A.; Katunuma, N. *J. Biochem.* **1983**, *93*, 1427.

(86) Kew, M. C.; Wolf, P.; Whittaker, D.; Rowe, P. *Br. J. Cancer* **1984**, *50*, 451.

(87) Xu, K.-C.; Meng, X.-Y.; Shi, Y.-C.; Ge, Z.-J.; Ye, L.; Yu, Z.-J.; Yang, D.-M. *Int. J. Cancer* **1985**, *36*, 667.

(88) Zhu, J.; Jiang, F.; Ni, H.-B.; Xiao, M.-B.; Chen, B.-Y.; Ni, W.-K.; Lu, C.-H.; Ni, R.-Z. *Exp. Ther. Med,* **2013**, *5*, 89.

(89) Sulzenbacher, G.; Bignon, C.; Nishimura, T.; Tarling, C. A.; Withers, S. G.; Henrissat, B.; Bourne, Y. *J. Biol. Chem.* **2004**, *279*, 13119.

(90) Cordero, O. J.; Merino, A.; de la Cadena, M. P.; Bugía, B.; Nogueira, M.; Viñuela, J. E.; Martínez-Zorzano, V. S.; de Carlos, A.; Rodríguez-Berrocal, F. J. *Eur. J. Biochem.* **2001**, *268*, 3321.

(91) Levvy, G. A.; McAllan, A. *Biochem. J.* **1961**, *80*, 435.

(92) El-Houseini, M. E.; Sherbiny, M. E.; El-Din Awad, M. M.; Amer, M. A.; Saad El Din, A. H.; Hussein, T. D. *J. Egypt Natl. Cancer Inst.* **2001**, *13*, 277.

(93) Avila, J.; Convit, J. *Biochim. Biophys. Acta* **1974**, *358*, 308.

(94) Sulzenbacher, G.; Bignon, C.; Nishimura, T.; Tarling, C. A.; Withers, S. G.; Henrissa, B.; Bourne, Y. *The Journal of Biological Chemistry* **2004**, *279*.

(95) Deugnier, Y.; David, V.; Brissot, P.; Mabo, P.; Delamaire, D.; Messner, M.; Bourel, M.; Legall, J.-Y. *Hepatology* **1984**, *4*, 889.

(96) Troost, J.; van der Heijden, M. C. M.; Staal, G. E. J. *Clinica Chimica Acta* **1976**, *73*, 329.

(97) El-Houseini, M. E.; Mohammed, M. S.; Elshemey, W. M.; Hussein, T. D.; Desouky, O. S.; Elsayed, A. A. *Cancer Control* **2005**, *12*, 248.

(98) El-Tayeh, S. F.; Hussein, T. D.; El-Houseini, M. E.; Amer, M. A.; El-Sherbini, M.; Elshemey, W. M. *Disease markers* **2012**, *32*, 255.

(99) Giardina, M. G.; Matarazzo, M.; Morante, R.; Lucariello, A.; Varriale, A.; Guardasole, V.; De Marco, G. *Cancer* **1998**, *83*, 2468.

(100) Montaser, M. F.; Sakr, M. A.; Khalifa, M. O. *Arab Journal of Gastroenterology* **2012**, *13*, 9.

(101) Wang, J.-J.; Cao, E.-H. *Clin. Chim. Acta* **2004**, *347*, 103.

(102) Tappeiner, H. V.; Jodlbauer, A. *Dtsch. Arch. Klin. Med.* **1904**, *80*, 427.

(103) Szeimies, R.-M.; Drager, J.; Abels, C.; Landthaler, M. In *Photodynamic Therapy and Fluorescence Diagnosis in Dermatology*; Calzavara-Pinton, P., Szeimies, R.-M., Ortel, B., Eds.; Elsevier: 2001; Vol. 2, p 3.

(104) Lipson, R. L.; Baldes, E. J. *AMA Arch. Derm.* **1960**, *82*, 508.

(105) Sharman, W. M.; Allen, C. M.; van Lier, J. E. *Drug Discov. Today* **1999**, *4*, 507.

(106) Ochsner, M. *J. Photochem. Photobiol. B: Biology* **1997**, *39*, 1.

(107) Leonard, K. A.; Nelen, M. I.; ANderson, L.; Detty, M. R. *J. Med. Chem.* **1999**, *42*, 3942.

(108) Brown, J. E.; Brown, S. B.; Vernon, D. I. *Adv. Colour Sci. Tech.* **2001**, *4*, 108.

(109) Konan, Y. N.; Gurny, R.; Alleman, E. *J. Photochem. Photobiol. B: Biology* **2002**, *66*, 89.

(110) Zane, C. In *Photodynamic Therapy and Fluorescence Diagnosis in Dermatology*; Calzavara-Pinton, P., Szeimies, R.-M., Ortel, B., Eds.; Elsevier: Amsterdam, The Netherlands, 2001; Vol. 2, p 101.

(111) Bonnett, R. *Chemical Aspects of Photodynamic Therapy*; Gordon and Breach Science: Netherlands, 2000; Vol. 1.

(112) Stilts, C. E.; Nelen, M. I.; Hilmey, D. G.; Davies, S. R. *J. Med. Chem.* **2000**, *43*, 2403.

(113) Hilmey, D. G.; Masako, A.; Nelen, M. I.; Stilts, C.; Detty, M. R. *J. Med. Chem.* **2002**, *45*, 449.

(114) You, Y.; Gibson, S.; Hilf, R.; Davies, S. R.; Detty, M. R. *J. Med. Chem.* **2003**, *46*, 3734.

(115) Gorman, A. A.; Hamblett, I.; Lambert, C.; Prescott, A. L.; Rodgers, M.; Spence, H. M. *J. Am. Chem. Soc.* **1987**, *109*, 3091.

(116) Henderson, B. W.; Dougherty, T. J. *Photochem. Photobiol.* **1992**, *55*, 145.

(117) Hamblin, M. R.; Hasan, T. *Photochem. Photobiol. Sci.* **2004**, *3*, 436.

(118) Halili, F.; Arboleda, A.; Durkee, H.; Taneja, M.; Miller, D.; Alawa, K. A.; Aguilar, M. C.; Amescua, G.; Flynn Jr, H. W.; Parel, J.-M. *Am. J. Ophthalmol.* **2016**, *166*, 194.

(119) Gutsche, C. D. N., K. C. *J. Am. Chem. Soc.* **1988**, *110*, 6153.

(120) He, W.; Liu, F.; Ye, Z.; Zhang, Y.; Guo, Z.; Zhu, L.; Zhai, X.; Li, J. *Langmuir* **2001**, *17*, 1143.

(121) Tanaka, Y. M., M.; Kobuke, Y. *Angew. Chem. Int. Ed. Engl.* **1999**, *38*, 504.

(122) Daschblach, M. M. K., O. V.; Long, E. F.; Gokel, G. W. *Chem. Eur. J.* **2011**, *17*, 8913.

(123) Han, J.; Song, X.; Liu, L.; Yan, C. *J Incl Phenom Macrocycl Chem* **2007**, *59*, 257.

(124) Románszki, L.; Mohos, M.; Telegdi, J.; Keresztes, Z.; Nyikos, L. *Period. Polytech. Chem. Eng.* **2014**, *58*, 53.

(125) Li, S. M., M.; Orbulescu, J; Whyte, J. D.; Leblanc, R. M. *J. R. Soc. Interface* **2012**, *8*, 10.

(126) Dluhy, R. A. *J. Phys. Chem.* **1986**, *90*, 1373.

(127) Block, T. M.; Comunale, M. A.; Lowman, M.; Steel, L. F.; Romano, P. R.; Fimmel, C.; Tennant, B. C.; London, W. T.; Evans, A. A.; Blumberg, B. S.; Dwek, R. A.; Mattu, T. S.; Mehta, A. S. *Proc. Natl. Acad. Sci. USA* **2005**, *102*, 779.

(128) Alhadeff, J. A. *Trends Comp. Biochem. Phys.* **1998**, *4*, 105.

(129) Hopfer, R. L.; Johnson, S. W.; Masserini, M.; Giuliani, A.; Alhadeff, J. A. *Biochem. J.* **1990**, *266*, 491.

(130) Baszkin, A. *Adv. Colloid Interface Sci.* **2006**, *128–130*, 111.

(131) de Claro, R. A.; McGinn, K.; Kwitkowski, V.; Bullock, J.; Khandelwal, A.; Habtemariam, B.; Ouyang, Y.; Saber, H.; Lee, K.; Koti, K.; Rothmann, M.; Shapiro, M.; Borrego, F.; Clouse, K.; Chen, X. H.; Brown, J.; Akinsanya, L.; Kane, R.; Kaminskas, E.; Farrell, A.; Pazdur, R. *Clin. Cancer Res.* **2012**, *18*, 5845.

(132) Amiri-Kordestani, L.; Blumenthal, G. M.; Xu, Q. C.; Zhang, L.; Tang, S. W.; Ha, L.; Weinberg, W. C.; Chi, B.; Candau-Chacon, R.; Hughes, P.; Russell, A. M.; Miksinski, S. P.; Chen, X. H.; McGuinn, W. D.; Palmby, T.; Schrieber, S. J.; Liu, Q.; Wang, J.; Song, P.; Mehrotra, N.; Skarupa, L.; Clouse, K.; Al-Hakim, A.; Sridhara, R.; Ibrahim, A.; Justice, R.; Pazdur, R.; Cortazar, P. *Clin. Cancer Res.* **2014**, *20*, 4436.

(133) Carter, P. J.; Senter, P. D. *Cancer J.* **2008**, *14*, 154.

(134) Hess, C. V., Dario; Neri, Dario *Med. Chem. Commun.* **2014**, *5*, 408.

(135) Shor, B.; Gerber, H.-P.; Sapra, P. *Mol. Immunol.* **2014**.

(136) Adamson, A. W.; Gast, A. P. *Physical Chemistry of Surfaces*; Wiley and Sons, 1997.

(137) Orbulescu, J.; Micic, M.; Ensor, M.; Trajkovic, S.; Daunert, S.; Leblanc, R. M. *Langmuir* **2010**, *26*, 3268.

(138) Oliveira, O. N.; Bonardi, C. *Langmuir* **1997**, *13*, 5920.

(139) Andelman, D.; Brochard, F.; Joanny, J. F. *J. Chem. Phys.* **1987**, *86*, 3673.

(140) Vagharchakian, L.; Desbat, B.; Hénon, S. *Macromolecules* **2004**, *37*, 8715.

(141) Jackson, M.; Mantsch, H. H. *Criti. Rev. Biochem. Mol. Bio.* **1995**, *30*, 95.

(142) Pribic, R.; Vanstokkum, I. H. M.; Chapman, D.; Haris, P. I.; Bloemendal, M. *Anal. Biochem.* **1993**, *214*, 366.

(143) Surewicz, W. K.; Mantsch, H. H.; Chapman, D. *Biochemistry* **1993**, *32*, 389.

(144) Wang, K.; Guo, W.; Li, N.; Shi, J.; Zhang, C.; Lau, W. Y.; Wu, M.; Cheng, S. *Br J Cancer* **2014**, *110*, 1811.

(145) DiCioccio, R. A.; Piskorz, C.; Salamida, G.; Barlow, J. J.; Matta, K. L. *Anal. Biochem.* **1981**, *111*, 176.

(146) Andersen, D. C.; Reilly, D. E. *Curr. Opin. Biotech.* **2004**, *15*, 456.

(147) Engvall, E.; Perlman, P. *Immunochemistry* **1971**, *8*, 871.

(148) Guilbault, G. G.; Montalvo, J. G. *J. Am. Chem. Soc.* **1970**, *92*, 2533.

(149) Guilbault, G. G.; Montalvo, J. G. *J. Am. Chem. Soc.* **1969**, *91*, 2164.

(150) Angenendt, P.; Glokler, J.; Murphy, D.; Lehrach, H.; Cahill, D. J. *Anal. Biochem.* **2002**, *309*, 253.

(151) Brueggemeier, S. B.; Wu, D.; Kron, S. J.; Palecek, S. P. *Biomacromolecules* **2005**, *6*, 2765.

(152) Fidanza, J.; Glazer, M.; Mutnick, D.; McGall, G.; Frank, C. *Nucleosides Nucleoides Nucleic Acids* **2001**, *20*, 533.

(153) Wang, H.; Li, J.; Liu, H.; Lui, Q.; Mei, Q.; Wang, Y.; Zhu, J.; He, N.; Lu, Z. *Nucl. Acids Res.* **2002**, *30*, 61.

(154) Zubtsov, D. A.; Ivanov, S. M.; Rubina, A. Y.; Dementieva, E. I.; Chechetkin, V. R.; Zasedatelev, A. S. *J. Biotechnol.* **2006**, *122*, 16.

(155) Boksanyi, L.; Liardon, O.; Kovats, E. S. *Adv. Colloid. Interface Sci.* **1976**, *6*.

(156) Tripp, C. P.; Hair, M. L. *Langmuir* **1995**, *11*, 149.

(157) Clark, J. H.; Macquarrie, D. J. *Chem. Commun.* **1998**, *8*, 853.

(158) Tripp, C. P.; Hair, M. L. *Langmuir* **1992**, *8*, 1961.

(159) Gobet, J.; Kovats, E. S. *Adsorp. Sci. Technol.* **1984**, *1*, 77.

(160) Navarre, S.; Choplin, F.; Bousbaa, J.; Bennetau, B.; Nony, L.; Aime, J.-P. *Langmuir* **2001**, *17*, 4844.

(161) Yang, Z.; Li, Z.; Xu, M.; Ma, Y.; Zhang, J.; Su, Y.; Gao, F.; Wei, H.; Zhang, L. *Nano-Micro Lett.* **2013**, *5*, 247.

(162) Kroto, H. W.; Heath, J. R.; O'Brien, S. C.; Curl, R. F.; Smalley, R. E. *Nature* **1985**, *318*, 162.

(163) Sweetnam, S.; Vandewal, K.; Cho, E.; Risko, C.; Coropceanu, V.; Salleo, A.; Bredas, J.-L.; McGehee, M. D. *Chem. Mater.* **2016**, *28*, 1446.

(164) Wang, X.; Li, Q.; Xie, J.; Jin, Z.; Wang, J.; Li, Y.; Jiang, K.; Fan, S. *Nano Lett.* **2009**, *9*, 3137.

(165) Miles, B. T.; Greenwood, A. B.; Pattton, B. R.; Gersen, H. *ACS Photonics* **2016**, *3*, 343.

(166) Zuo, P.; Lu, X.; Sun, Z.; Guo, Y.; He, H. *Microchim. Acta* **2015**, *183*, 519.

(167) Shahnawaz Khan, M.; Bhaisare, M. L.; Pandey, S.; Talib, A.; Wu, S.-M.; Kailasa, S. K.; Wu, H.-F. *Int. J. Mass Spectrom.* **2015**, *393*, 25.

(168) Sheng, Y.; Wei, J.; Pan, J.; Huang, P.; Guo, S.; Zhang, J.; Zhang, X.; Feng, B. *Chem. Phys. Lett.* **2015**, *638*, 196.

(169) Pan, D.; Zhang, J.; Li, Z.; Wu, C.; Yan, X.; Wu, M. *Chem. Comm.* **2010**, *46*, 3681.

(170) Li, S.; Wang, L.; Chusuei, C. C.; Suarez, V. M.; Blackwelder, P. L.; Micic, M.; Orbulescu, J.; Leblanc, R. M. *Chem. Mater.* **2015**, *27*, 1764.

(171) Sun, Y.-P.; Zhou, B.; Lin, Y.; Wang, W.; Fernando, K. A. S.; Pathak, P.; Meziani, M. J.; Harruff, B. A.; Wang, X.; Wang, H.; Luo, P. G.; Yang, H.; Kose, M. E.; Chen, B.; Veca, L. M.; Xie, S.-Y. *J. Am. Chem. Soc.* **2006**, *128*, 7756.

(172) Guo, Y.; Wang, Z.; Shao, H.; Jiang, X. *Carbon* **2013**, *52*, 583.

(173) Hsu, P.-C.; Chang, H.-T. *Chem. Comm.* **2012**, *48*, 3984.

(174) Chen, P.-C.; Chen, Y.-N.; Hsu, P.-C.; Shih, C.-C.; Chang, H.-T. *Chem. Comm.* **2013**, *49*, 1639.

(175) Du, F.; Zeng, F.; Ming, Y.; Wu, S. *Microchim. Acta* **2013**, *180*, 453.

(176) Zhai, X.; Zhang, P.; Liu, C.; Bai, T.; Li, W.; Dai, L.; Liu, W. *Chem. Comm.* **2012**, *48*, 7955.

(177) Zhang, P.; Li, W.; Zhai, X.; Liu, C.; Dai, L.; Liu, W. *Chem. Comm.* **2012**, *48*, 10431.

(178) Liu, S.; Wang, L.; Tian, J.; Zhai, J.; Luo, Y.; Lu, W.; Sun, X. *RSC Adv.* **2011**, *1*, 951.

(179) Wang, Q.; Liu, X.; Zhang, L.; Lv, Y. *Analyst* **2012**, *137*, 5392.

(180) Qin, X.; Lu, W.; Asiri, A. M.; Al-Youbi, A. O.; Sun, X. *Sens. Actuators B: Chem.* **2013**, *184*, 156.

(181) Zhu, C.; Zhai, J.; Dong, S. *Chem. Comm.* **2012**, *48*, 9367.

(182) Liu, H.; Ye, T.; Mao, C. *Angew. Chem. Int .Ed.* **2007**, *46*, 6473.

(183) Zhang, B.; Yang, Q.; Li, Z.; Hao, J. *Colloids and Surf. A* **2015**, *485*, 34.

(184) Kreibig, U.; Genzel, L. *Surf. Sci.* **1985**, *156*, 678.

(185) Haas, W.; Pillar, C. M.; Torres, M.; Morris, T. W.; Sahm, D. F. *Am. J. Ophthalmol.* **2011**, *152*, 567.

(186) Miller, D.; Chang, J. S.; Flynn, H. W.; Alfonso, E. C. *J. Ocul. Pharmacol. Ther.* **2013**, *29*, 339.

(187) Mah, F. S.; Davidson, R.; Holland, E. J.; Hovanesian, J.; John, T.; Kanellopoulos, J.; Shamie, N.; Starr, C.; Vroman, D.; Kim, T. *J. Cataract Refract. Surg.* **2014**, *40*, 1894.

(188) Brooks, S. E.; Kaza, V.; Nakamura, T.; Trousdale, M. D. *Cornea* **1994**, *13*, 43.

(189) Nowak-Sliwinska, P.; van den Bergh, H.; Sickenberg, M.; Koh, A. H. C. *Prog. Retin. Eye Res.* **2013**, *37*, 182.

(190) Lindig, B. A.; Rodger, M. A. J.; Schaap, P. *J. Am. Chem. Soc.* **1980**, *102*, 5590.

(191) Spiller, W.; Kliesch, H.; Wöhrle, D.; Hackbarth, S.; Röder, B.; Schnurpfeil, G. *J Porphyrins Phthalocyanines* **1998**, *2*, 145.

(192) Tanielian, C.; Heinrich, G. *Photochem. Photobiol.* **1995**, *61*, 131.

(193) Lambert, C.; Sarna, T.; Truscott, T. G. *J. Chem. Soc. Faraday Trans.* **1990**, *86*, 3879.

(194) Schäfer, M.; Schmitz, C.; Facius, R.; Horneck, G.; Milow, B.; Funken, K. H.; Ortner, J. *Photochem. Photobiol.* **2000**, *71*, 514.

(195) Morton, C. O.; Chau, M.; Stack, C. *BMC Microbiol.* **2014**, *14*, 261.

(196) Gottschalk, P.; Paczkowski, J.; Neckers, D. C. *J. Photochem.* **1986**, *35*, 277.

(197) Gandin, E.; Lion, Y.; Van de Vorst, A. *Photochem. Photobiol.* **1983**, *37*, 271.

(198) Arboleda, A.; Miller, D.; Cabot, F.; Taneja, M.; Aguilar, M. C.; Alawa, K.; Amescua, G.; Yoo, S. H.; Parel, J.-M. *Am. J. Ophthalmol.* **2014**, *158*, 64.

(199) Kashiwabuchi, R. T.; Carvalho, F. R. S.; Khan, Y. A.; Hirai, F.; Campos, M. S.; McDonnell, P. J. *Graefes Arch. Clin. Exp. Ophthalmol.* **2013**, *251*, 521.

(200) Kalkanci, A.; Ozdek, S. *Curr. Eye Res.* **2011**, *36*, 179.

(201) Baier, J.; Maisch, T.; Maier, M.; Engel, E.; Landthaler, M.; Bäumler, W. *Biophys. J.* **2006**, *91*, 1452.

(202) Chancon, J. N.; McLearie, J.; Sinclair, R. S. *Photochem. Photobiol.* **1988**, *47*, 647.

(203) Foote, C. S. In *Singlet Oxygen*; Wasserman, H. H., Murrary, R. W., Eds.; Academic Press: New York, San Francisco, London, 1979, p 139.

(204) Murassecco, P.; Oliveros, E.; Braun, A. M.; Monnier, P. *Photochem. Photobiol.* **1985**, *9*, 193.

(205) Yehye, W. A.; Rahman, N. A.; Ariffin, A.; Abd Hamid, S. B.; Alhadi, A. A.; Kadir, F. A.; Yaeghoobi, M. *Eur. J. Med. Chem.* **2015**, *101*, 295.

(206) Kraljić, I.; Mohsni, S. E. *Photochem. Photobiol.* **1978**, *28*, 577.

(207) Verlhac, J. B.; Gaudemer, A. *Nouv. J. Chim.* **1984**, *8*, 401.

(208) Haag, W. R.; Hoigne, J.; Gassman, E.; Braun, A. M. *Chemosphere* **1984**, *13*, 631.

(209) Braun, A. M.; Dahn, H.; Gassman, E.; Gerothanassis, I.; Jakob, L.; Kateva, N.; Martinez, C.; Oliveros, E. *Photochem. Photobiol.* **1999**, *70*, 868.